Università di Pisa

Department of Physics "E. Fermi"

Master Degree in Physics

Real-time reconstruction of tracks in the Scintillating Fibre Tracker of the LHCb Upgrade

---

Author:
Andrea Di Luca

Supervisor:
Dott. Michael J. Morello

Academic year 2017/2018

Contents

Introduction

The precise measurement of flavour-changing transitions in hadrons is a long-established and powerful tool to precisely study the dynamics of the Standard Model, and simultaneously to seek out manifestations of new physics phenomena. The mass scales that can be probed in loop-level processes are far higher than those that can be accessed in direct searches for on-shell particles. Furthermore, many of the open questions in fundamental physics reside in the flavour sector. The LHCb experiment has demonstrated that the LHC is an ideal laboratory for quark-flavour physics. The current LHCb detector, operating at a luminosity of $4 \times 10^{32} \mathrm{cm}^{-2} \mathrm{s}^{-1}$, will continue data taking until the end of Run 2 of the LHC, in 2018. During Long Shutdown 2 (LS2) it will be replaced by an upgraded experiment, referred as the Phase-I Upgrade (LHC Run 3, 2021-2024 and LHC Run 4, 2027-2029). The Phase-I Upgrade, operating at a luminosity of $L = 2 \times 10^{33} \mathrm{cm}^{-2} \mathrm{s}^{-1}$, will greatly improve the sensitivity of many flavour studies. However, the precision on a host of important, theoretically clean, measurements will still be limited by statistics, and other observables associated with highly suppressed processes will be poorly known. There is therefore a strong motivation for a consolidation of the the Phase-I Upgrade in view of the LHC Run 4[1], and for building a Phase-II Upgrade, which will fully realize the flavour potential of the HL-LHC during the LHC Run 5 ($\geq$ 2031) at luminosity $L > 10^{34} \mathrm{cm}^2 \mathrm{s}^{-1}$ [1, 2].

Although the trigger strategy of both the Phase-I and Phase-II Upgrades is software based, studies are underway to learn what benefits could accrue by adding dedicated processors to help solve specific low-level tasks. One relevant example is to find tracks downstream of the magnet at the earliest trigger level [1, 2]. This capability is not part of the baseline trigger scheme on account of the significant CPU time required to execute the search. Not having access to this information greatly limits efficiency for decay modes with downstream tracks that cannot easily be triggered through another signature, for example channels containing a K^0_s and less than two prompt charged hadrons, for example $B \to K^0_\mathrm{s} K^0_\mathrm{s}$, $B \to K^0_\mathrm{s} K^0_\mathrm{s} K^0_\mathrm{s}$, $B \to \eta K^0_\mathrm{s}$, $B \to \phi K^0_\mathrm{s}$, $B \to \omega K^0_\mathrm{s}$, $D^0 \to K^0_\mathrm{s} K^0_\mathrm{s}$, $D^+_s \to K^0_\mathrm{s} \pi^+$, $D^+ \to K^0_\mathrm{s} K^+$, $K^0_\mathrm{s} \to \mu\mu$, etc. The same is true for decays involving Λ baryons (i.e. $\Lambda^0_b \to 3\Lambda$) and long-lived exotic particles (hidden sector WIMP Dark Matter and Majorana neutrinos).

---

[1]In the current scheme no upgrades of the experiment are planned and funded in the LS3, neither for the sub-detectors nor for the data acquisition and trigger systems.

The LHCb Pisa group has recently proposed [1, 2] an innovative tracking device, the so called Downstream Tracker, capable of reconstructing in real-time long-lived particles in the context of the envisioned Future Upgrades (beyond LHC Run 3) of the LHCb experiment, with the aim of recovering the reconstruction efficiency of the downstream tracks. Such a specialized processor is supposed to obtain a copy of data from the readout system, reconstruct downstream tracks, and insert them back in the readout chain before the event is assembled, in order to be sent to the high level trigger in parallel with the raw detector information. This approach, where tracks can be seen as the output of an additional "embedded track detector" is based on the *artificial retina* algorithm [3], which is a highly-parallel pattern-matching algorithm, whose architectural choices, inspired to the early stages of image processing in mammals, make it particularly suitable for implementing a track-finding system in present-day FPGAs. First small prototypes of track-processing unit, able to reconstruct two-dimensional straight-line tracks in a 6-layers realistic tracking detector, based on the artificial retina algorithm have been designed, simulated, and built [4, 5] using commercial boards, equipped with modern high-end FPGAs. Throughputs in processing realistic LHCb-Upgrade[2] events in the range of tens of MHz[3] and latencies lesser than 1 μs have been achieved running at the nominal clock speed, demonstrating the feasibility of fast track-finding with a FPGA-based system. This open the way for a full realistic application as the Downstream Tracker. In fact, the design can be scaled to larger area detectors and to higher input rates in a cost-effective way.

The aim of this thesis project is to assess the tracking performance, that such an approach could achieve to the Future Upgrades of the LHCb experiment, for the realization of the Downstream Tracker project. This will be evaluated within known budget constraints [6]; an affordable size of such an envisioned device has to be of about 10^5 pattern cells, where each of them corresponds to about 1000 Logic Elements (LEs). A high-level simulation of the envisioned device, written in C++ programming language, has been therefore developed in order to determine the achievable tracking performances, given the above constraints on the size of the system and on the compliance with the future LHCb data acquisition system. The main task of thesis has been the precise determination of the tracking parameters in reconstructing LHCb-Upgrade downstream tracks, such as the reconstruction efficiency and the probability of reconstructing fake tracks ('ghosts') as a function of track parameters, along the resolution in measuring three-dimensional momentum and space trajectory. Lastly, an exhaustive comparison between simulated tracks, reconstructed by the envisioned device, and tracks reconstructed with LHCb-Upgrade offline tracking program, running in the high level trigger sequence, has been carried out in order to assess tracking performance in absolute terms. In particular, the thesis project has faced the challenge of reconstructing the so-called T-tracks, i.e. the tracks reconstructed using hits from the Scintillating Fibre Tracker detector (SciFi detector) [7] located downstream the dipole magnet. This is the first, and the most

---

[2]Running conditions in Run 4 will be the same as in Run 3, the so called LHCb-Upgrade.
[3]The LHC inelastic events rate is 30 MHz.

CPU-time consuming, stage of the reconstruction of downstream tracks.

The thesis presents the first results on the reconstruction of the three-dimensional T-tracks of a generic LHCb-Upgrade event. Using a number of 2×10^5 pattern cells, corresponding to about 1300 pattern cells in a single FPGA chip[4], it has been possibile to solve the pattern recognition both in the axial (10^5 pattern cells for 6-axial layers) and stereo (10^5 pattern cells for 6-stereo layers) views of the SciFi detector. The SciFi detector has the highest hits occupancy amongst the LHCb-Upgrade sub-detectors with an average number of reconstructible tracks per event of about 140 tracks/event, where the long tail of the distribution reaches values up to 400 tracks/event. Both reconstruction efficiency and ghost rate[5] are comparable to those obtained with the official offline tracking program; a generic T-track is reconstructed with an efficiency of about 70% with a ghost rate of about 20%. Requiring a minimal momentum threshold, as three-dimensional momentum larger than 5 GeV, and that the track has to be a downstream track or it has to come from the interaction point, efficiencies in the range of 90% are achieved. Resolution on the measurement of track parameters are also comparable to those obtained with the official offline tracking program.

In conclusion, this thesis presents the first study of the performance of real-time reconstruction of tracks in the SciFi detector achievable with the artificial retina algorithm, using fully simulated events at the LHCb Upgrade (LHC Run 4) conditions. This is a crucial milestone on the path of the realization of the Downstream Tracker processor for the Future Upgrades of the LHCb experiment. This thesis has shown that tracking performance obtainable with this approach is comparable with the offline software reconstruction performance.

---

[4]As examples of currently available high-end FPGA chips on the market, the Intel Stratix V (5SGSD8) has 0.7M LEs and 1900 variable-precision digital signal processing (DSP) blocks, while the Intel Stratix X (MX1650) has 1.6M of LEs and 3300 DSP blocks.

[5]Reconstruction efficiency is defined as the ratio of the number of truth-matched reconstructed tracks to the number of reconstructible tracks in the SciFi acceptance. The ghost rate, instead, is defined as the ratio of the difference between the number of reconstructed tracks and the number of truth-matched reconstructed track to the number of the reconstructed tracks.

Chapter 1

Physics Landscape

This chapter introduces the phenomenology of CP violation in the standard model of particle physics, with a particular focus on the primary role of heavy flavoured mesons. Finally, a short summary of the current and future experimental effort in searching hints of new phenomena in the heavy flavour physics is presented.

1.1 CP violation and heavy flavour physics

The CP violation, i.e. the non-invariance of the weak interactions with respect to a combined charge-conjugation (C) and parity (P) transformation, dates back to year 1964, when this phenomenon was discovered through the observation of $K_{\mathrm{L}} \to \pi^+\pi^-$ decays [8]. One of the key features of our Universe is the cosmological baryon asymmetry of $\mathcal{O}(10^{-10})$. As was pointed out by Sakharov [9], the necessary conditions for the generation of such an asymmetry include also the requirement that elementary interactions violate CP. Model calculations of the baryon asymmetry indicate, however, that the CP violation present in the Standard Model (SM), *i.e.* the theory which currently describes better the nature at the smallest scale of fundamental interaction, seems to be too small to generate the observed asymmetry.

The understanding of CP violation, and therefore of flavour physics, is particularly interesting since New Physics (NP), *i.e.* physics lying beyond the SM, typically leads to new sources of flavour and CP violation. Following this direction, an important field of investigation is represented by flavor physics at accelerating machines, and in particular by the beauty and charm sectors. Over years, numerous experiments were dedicated to b and c-hadron study, following different approaches. Two deeply different but complementary environments are represented by B-factories and by high energy hadron colliders. Both study CP invariance violation in bottom and charmed hadron physics by performing high precision measurements of CP violation, to increasingly constrain the theoretical uncertainties on SM and to search for NP.

As already mentioned above, the observation of neutral long-lived K mesons decay in both two and three pions states [8] showed, in 1964, that not all interactions in Nature are symmetric under CP transformation. The measurement of a $\mathcal{O}(10^{-3})$ branching fraction for the $K_L^0 \to \pi^+\pi^-$ was the first evidence for CP violation in

Nature. In particular, this is a manifestation of indirect CP violation, caused by the fact that the neutral kaon mass eigenstates, K_L^0 and K_S^0, are not eigenstates of the CP operator. This causes the small CP-even component of the K_L^0 state decay into the $\pi^+\pi^-$ final state. After 30 years of series of experiments, in 1999 was established the first direct CP violation evidence, still in neutral kaon states, by NA48 [10] and KTeV [11] collaborations. It directly concerns the decay amplitudes of two CP conjugate states, and confirms the theory for which the CP violation is an universal property of the weak interaction, proposed by Wolfenstein [12] in 1964 just after its first observation. Huge experimental efforts have been dedicated to extend the CP violation study on other systems than kaons, BaBar [13] and Belle [14] experiments observed for the first time the $B^0 \to J/\psi K$ decay-rate asymmetry, caused by the interference of decay amplitudes occurred with $B^0 - \overline{B}^0$ flavor mixing and the amplitude of the direct decays.

1.2 The quark mixing matrix

Since the first experimental evidence of CP violation in Nature, considerable efforts to describe it into a coherent theoretical environment have been performed. They significantly have contributed to build the SM, describing the electroweak interactions. In this framework, CP-violating effects originate from the charged-current interactions of quarks, having structure:

$$D \to U W^-,$$

where D denotes down-quark flavors (d, s, b), U denotes up-type quark flavors (u, c, t) and W^- is the usual gauge boson. The electroweak states (d', s', b') respectively of d, s, b quarks are connected with their mass eigenstates (d, s, b) through the following unitary transformation:

$$\begin{pmatrix} d' \\ s' \\ b' \end{pmatrix} = V_{\text{CKM}} \cdot \begin{pmatrix} d \\ s \\ b \end{pmatrix},$$

where V_{CKM} is the unitary Cabibbo-Kobayashi-Maskawa (CKM) matrix [15,16], which represent the generic "coupling strengths" V_{UD} of the charged-current processes:

$$V_{\text{CKM}} = \begin{pmatrix} V_{ud} & V_{us} & V_{ub} \\ V_{cd} & V_{cs} & V_{cb} \\ V_{td} & V_{ts} & V_{tb} \end{pmatrix}.$$

Expressing the non-leptonic charged-current interaction Lagrangian in terms of the mass eigenstates (d, s, b), we obtain:

$$\mathcal{L}_{int}^{CC} = -\frac{g_2}{\sqrt{2}} \left(\bar{u}_L, \quad \bar{c}_L, \quad \bar{t}_L \right) \gamma^\mu V_{\text{CKM}} \begin{pmatrix} d_L \\ s_L \\ b_L \end{pmatrix} W_\mu^\dagger + h.c., \tag{1.1}$$

where g_2 is a coupling constant, and the $W_\mu^{(\dagger)}$ field corresponds to the charged W bosons. Looking at the interaction vertices following from eq. 1.1, we observe that the V_{CKM} elements describe the generic strengths of the associated charged-current processes, as we have noted above. In a vertex $D \to U W^-$, CP transformation involves the replacement $V_{UD} \to V_{UD}^*$: CP violation could therefore be accommodated in the SM through complex phases in the CKM matrix. As pointed by Kobayashi and Maskawa in 1973 [16], the parametrization of V_{CKM} for three generations of quarks involves three Euler-type angles and one complex phase. However, further conditions have to be satisfied to observe CP-violating effects [17–19], related to quark mass hierarchy. Using the related experimental informations together with the CKM unitarity condition, and assuming only three quark generations, we obtain the following values for the CKM matrix elements [20]:

$$|V_{CKM}| = \begin{pmatrix} 0.974334^{+0.000064}_{-0.000068} & 0.22508^{+0.00030}_{-0.00028} & 0.003715^{+0.000060}_{-0.000060} \\ 0.22494^{+0.00029}_{-0.00028} & 0.973471^{+0.000067}_{-0.000067} & 0.04181^{+0.00028}_{-0.00060} \\ 0.008575^{+0.000076}_{-0.000098} & 0.04108^{+0.00030}_{-0.00057} & 0.999119^{+0.000024}_{-0.000012} \end{pmatrix}$$

Transitions within the same generation are governed by the CKM matrix elements of $\mathcal{O}(1)$, those between the first and the second generation are suppressed by CKM factors of $\mathcal{O}(10^{-1})$, those between the second and the third generation are suppressed by $\mathcal{O}(10^{-2})$, and transitions between the first and the third generation are suppressed by CKM factors of $\mathcal{O}(10^{-3})$.

To bring out the CKM matrix hierarchical structure, it is convenient to represent it in the so called "Wolfenstein parametrization" [21] as a function of a set of parameters λ, A, ρ, η:

$$V_{CKM} = \begin{pmatrix} 1 - \frac{1}{2}\lambda^2 & \lambda & A\lambda^3(\rho - i\eta) \\ -\lambda & 1 - \frac{1}{2}\lambda^2 & A\lambda^2 \\ A\lambda^3(\rho - i\eta) & -A\lambda^2 & 1 \end{pmatrix} + \mathcal{O}(\lambda^4),$$

The unitarity of the CKM matrix, which is described by the relationship:

$$V_{CKM}^\dagger \cdot V_{CKM} = V_{CKM} \cdot V_{CKM}^\dagger = I,$$

results into a set of 12 equations, consisting of 6 normalization and 6 orthogonality relations. The latter can be represented as 6 triangles in the complex plane, all having same area. However, only two of those are non-squashed triangles, having angles of same order of magnitude. They are defined by the relations:

$$\underbrace{V_{ud}V_{ub}^*}_{(\rho+i\eta)A\lambda^3} + \underbrace{V_{cd}V_{cb}^*}_{-A\lambda^3} + \underbrace{V_{td}V_{tb}^*}_{(1-\rho-i\eta)A\lambda^3} = 0,$$

$$\underbrace{V_{ud}^*V_{td}}_{(1-\rho-i\eta)A\lambda^3} + \underbrace{V_{us}^*V_{ts}}_{-A\lambda^3} + \underbrace{V_{ub}^*V_{tb}}_{(\rho+i\eta)A\lambda^3} = 0.$$

At λ^3 level, the two orthogonality relations agree with each other, yielding:

$$[(\rho + i\eta) + (-1) + (1 - \rho - i\eta)]A\lambda^3 = 0. \tag{1.2}$$

Therefore, those two orthogonality relations describe the same triangle in the (ρ, η) plane shown in Fig. 1.1, which is usually referred to as the unitarity triangle of the CKM matrix. Angles of unitarity triangle are usually called α, β, γ.
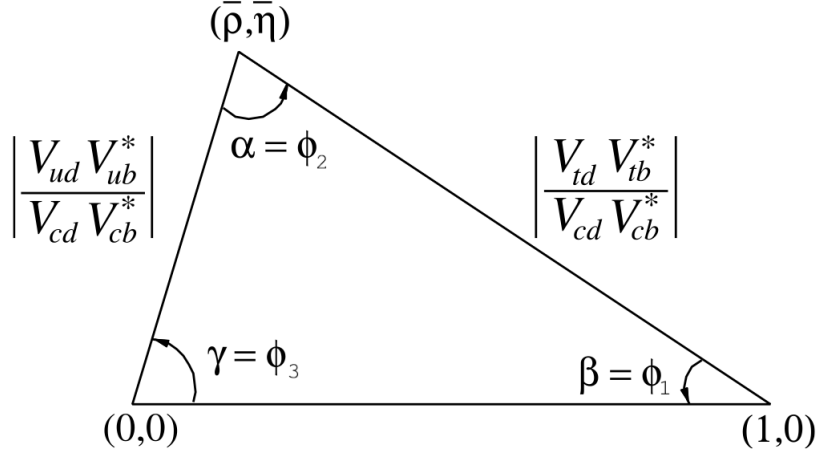

Figure 1.1: Rescaled unitarity angle.

The parametrization of the CKM matrix is not unique; in particular, we can replace the ρ, η parameters with a new set $(\bar{\rho}, \bar{\eta})$ in a such way to include in the equation 1.2 also terms $\mathcal{O}(\lambda^5)$, obtaining [22]:

$$[(\bar{\rho} + i\bar{\eta}) + (-1) + (1 - \bar{\rho} - i\bar{\eta})]A\lambda^3 + \mathcal{O}(\lambda^7) = 0,$$

where:

$$\bar{\rho} = \rho(1 - \frac{\lambda^2}{2}), \quad \bar{\eta} = \eta(1 - \frac{\lambda^2}{2}).$$

The CKM matrix has a great predictive potential on CP violating processes, and large experimental efforts have been performed to measure its parameters. Figure 1.2 shows the global fit of CKM parameters [20], in $(\bar{\rho}, \bar{\eta})$ plane, resulted by combining performed measurements. The study of several, different physics processes have provided measurements of CP asymmetry in Nature, which are all contained within the uncertainties of CKM parameters. Nevertheless, to the present day they are still not measured with great precision, such as for the γ parameter [20]:

$$\gamma = (72.1^{+5.4}_{-5.8})^\circ.$$

Much more, precise measurements of CKM parameters are required to seriously challenge the SM explanation of CP violation. This investigation represents a fundamental probe to validate at deeper scales of precision the SM predictions on observable physics processes, and to search for NP evidences.
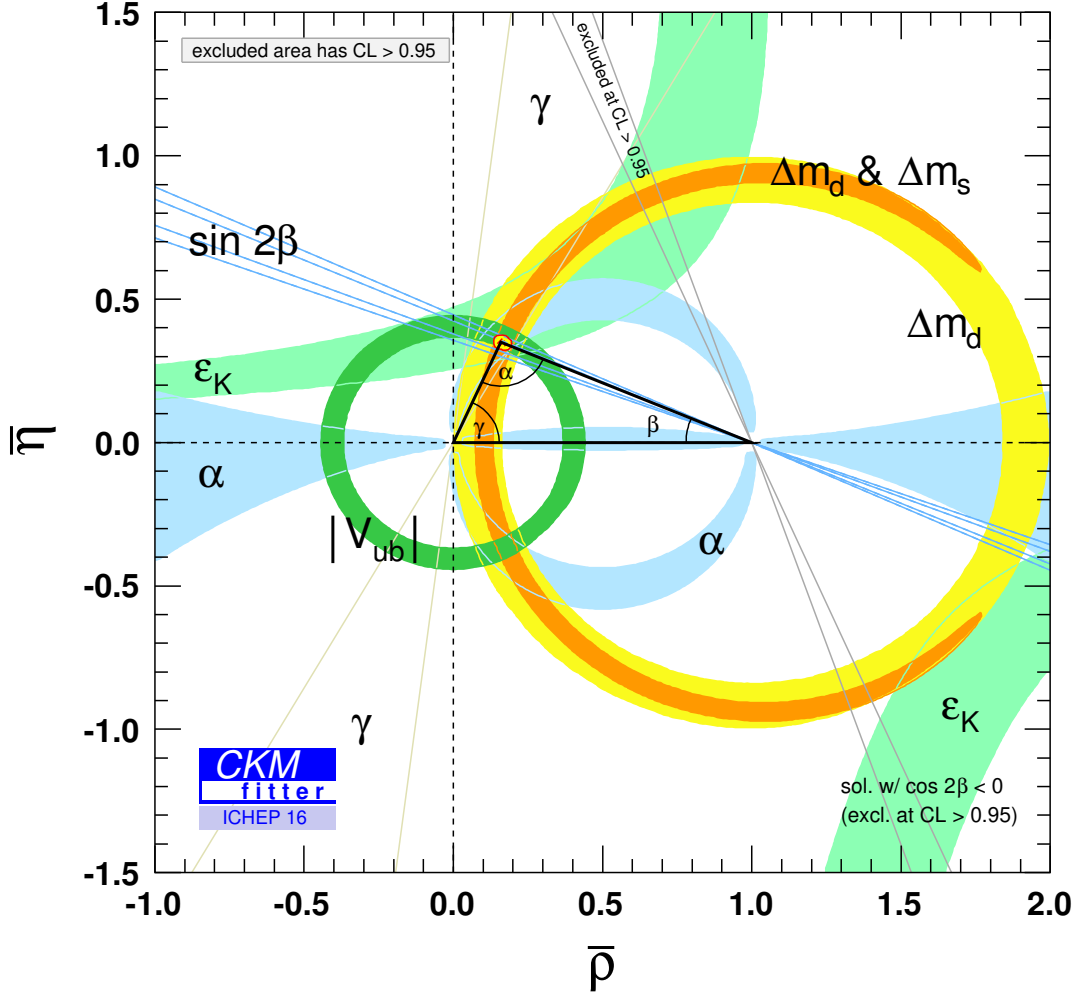
Figure 1.2: Global CKM fit in the $(\bar{\rho}, \bar{\eta})$ plane.

1.3 Experimental considerations on flavor physics

While *CP* violation might have a role in leptonic interactions as well, the most experimentally accessible field is that of quark interaction. In particular, due to its connection with the 3-generation structure of the matrix, the heavier quarks that are still able for form bound states (bottom and charm) play a central role. Luckily, the large mass of these quarks also helps in allowing some simplifying approximations in performing theoretical calculations of the relevant hadron dynamics. Past experiments on *b*- and *c*-physics have provided important contributions to the *CP* violation understanding, and to the determination of CKM matrix parameters.

At the same time, current and future experiments, such as LHCb at the LHC collider and Belle II at SuperKEKB machine, will be able to largely improve our knowledge on CKM parameters thanks to an huge production of b- and c-hadrons, resulting in a collection of very large samples of interesting physics processes.

The b-hadrons represent particularly interesting systems to study CP violation. First, they contain the b-quark, belonging to the third quark generation and therefore characterized by the possibility to decay to quarks of both first and second generations. This allows reaching larger CP violation effects than in kaon systems. Moreover, the larger mass of the b-quark compared to the s-quark one makes kinematically available many decay modes, offering multiple experimental possibilities to study CP-violating observables. Even if having a smaller mass, charmed hadrons equally represent very interesting systems, and they are the only system in which up-type quark interactions can be studied, which might in principle have a separate dynamics from down-type quarks. For these reasons, flavor physics represents a particularly promising and interesting sector to deeply study CP violation. However, the presence of multiple available channels results in small branching fractions of individual processes, and high statistic samples are therefore required.

Charmed hadron physics begun in lepton annihilation experiment in 1974, with the discovery of the J/ψ resonance at SLAC experiment [23] and Brookhaven Laboratory [24]. After only three years, the b-hadrons physics dates its beginning in proton-nucleus collisions with the discovery of the Υ resonance, in 1977 at Fermilab laboratory [25]. Measurements on heavy flavor states followed in UA1 experiment [26] and in CDF I from 1992 to 1996 (as example, see [27, 28]). Much more significant contributions to b-quark physics came from e^+e^- machines operating at the $\Upsilon(4S)$ resonance (the so named B-factories machines), or at the Z pole and more recently in hadronic machines, when the huge available cross section for production of heavy quarks started to be systematically exploited by means of new and improved experimental techniques.

1.3.1 The B-factories

B-factories are e^+e^- colliders with asymmetric beam energies, producing $\Upsilon(4S)$ resonances with 0.4-0.6 Lorentz boost. The $\Upsilon(4S)$ meson decays more than 96% of times into $B\overline{B}$ pairs (where B is B^0 or B^+) [29], which, thanks to the beam asymmetry, decay in vertices typically displaced by 200-300 μm. Exploiting the good spatial resolution of silicon detectors, this distance allows to determine the time-interval between the two decays with sufficient precision to measure time-dependent CP-violating asymmetries. Operating at an energy calibrated to the $\Upsilon(4S)$ production, just above the open beauty threshold, avoids the presence of fragmentation products and imposes kinematic constraints resulting in a background reduction. Pile-up events, that is multiple primary interactions in a single beam crossing, are typically absent and track multiplicity is typically not greater then ≈ 20 tracks per event. However, cross-section of $B\overline{B}$ production is limited to just $\sigma(b\bar{b}) \sim 1$ nb.

Past experiments installed at B-factories, such as BaBar [30] and Belle [31], successfully demonstrated the validity of this approach giving significant contributions to heavy flavor physics understanding, such as the measurement of the β angle of the unitarity triangle [32], shown in Figure 1.3 for the channel $B^0 \to \eta' K^0$. The Belle II experiment, at SuperKEKB B-factory, is currently being set up and is expected to begin data collection from 2019 [33].
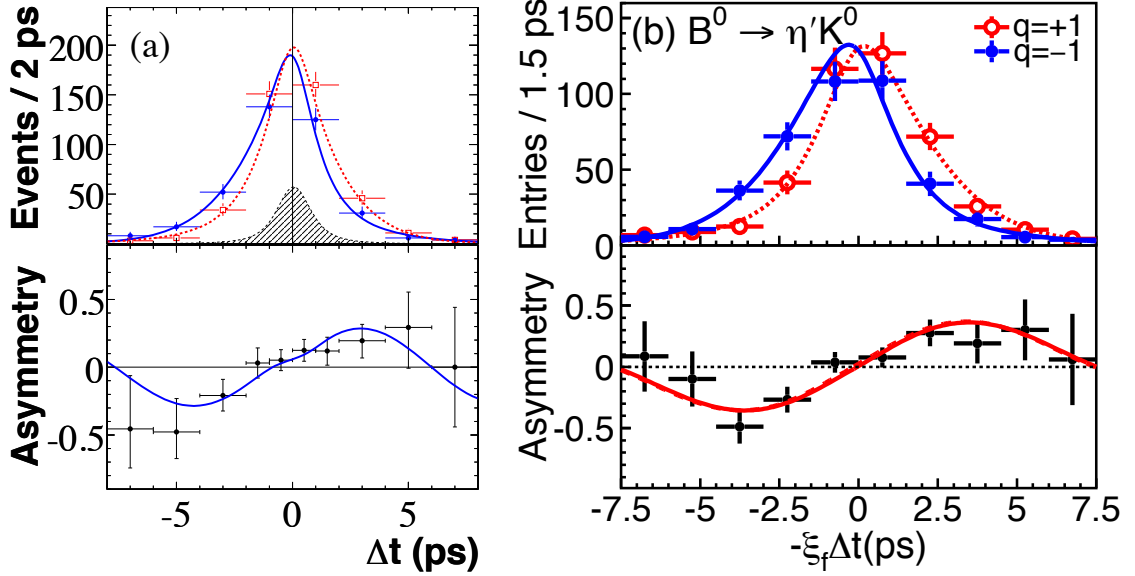

Figure 1.3: Measurement of Δt and asymmetries distributions in the $B^0 \to \eta' K^0$ channel, performed by BaBar (a) and Belle (b) experiments. For BaBar, only $\eta' K_{\mathrm{S}}^0$ mode is shown.

1.3.2 Hadron colliders

Hadron colliders have much larger cross-section for b- and c-quarks production. The dominant production process for b-hadrons is the non-resonant inclusive $b\bar{b}$ production, with typical values at Tevatron ($p\bar{p}$ collisions) and LHC (pp collisions), integrated on the entire solid angle:

$$\sigma(p\bar{p} \to b\bar{b}X, \sqrt{s} = 1.96\,\mathrm{TeV}) \sim 80\,\mu\mathrm{b},$$
$$\sigma(pp \to b\bar{b}X, \sqrt{s} = 14\,\mathrm{TeV}) \sim 500\,\mu\mathrm{b},$$

where $\sqrt{s}$ is the center-of-mass energy of the collision. These values can be compared with the typical $b\bar{b}$ cross-section production at B-factories, of $\sigma(b\bar{b}) \sim 1\,\mathrm{nb}$. Figure 1.4 reports the cross-sections trend for processes at pp and $p\bar{p}$ colliders, depending on machine $\sqrt{s}$. The $\sqrt{s}$ energy available at hadron colliders allows the production of all b-hadrons species: B^0 and B^+ mesons, but also B_s^0, B_c^+ mesons and b-baryons; moreover the typical $\beta\gamma$ Lorentz boost of produced b-hadrons are larger compared to B-factories. This results in larger decay lengths, which allow probing shorter scales

proton - (anti)proton cross sections
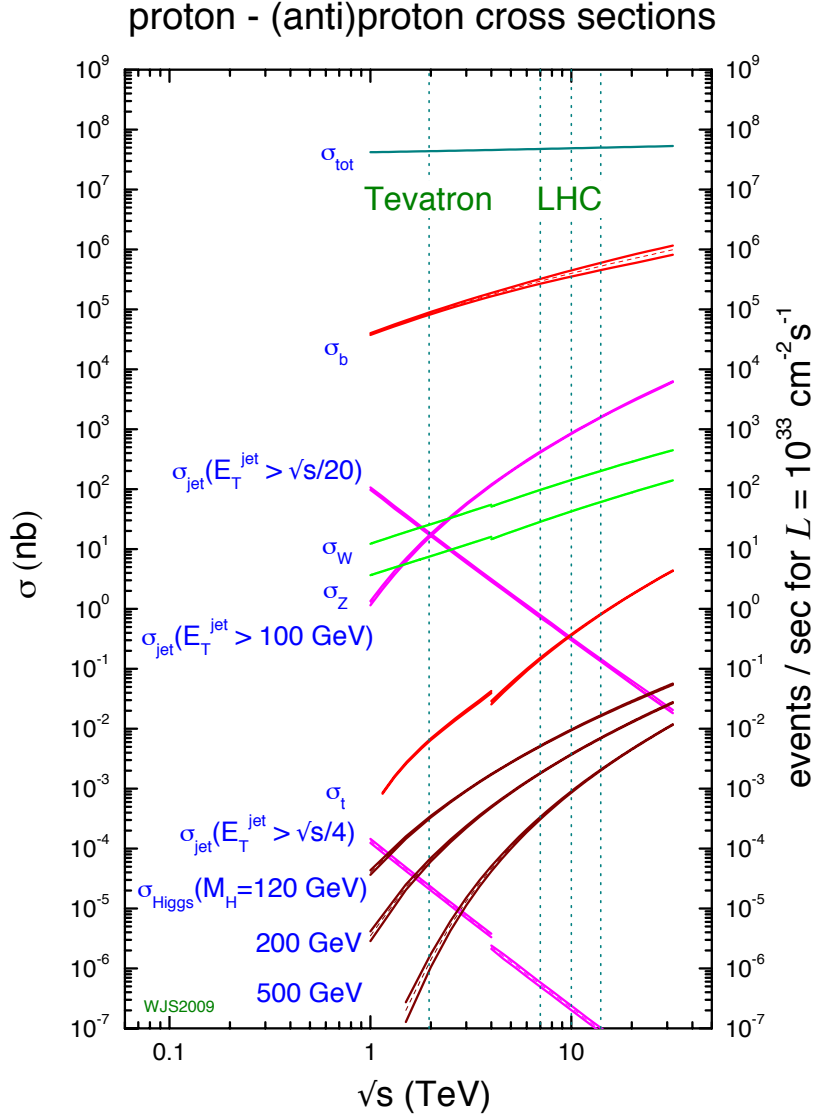
Figure 1.4: Cross-sections for processes at pp and $p\bar{p}$ colliders, depending on machine center-of-mass energy $\sqrt{s}$. Discontinuities are caused by transitioning from $p\bar{p}$ to pp collisions.

in heavy-flavor time-evolution. However, at hadron collisions the $b\bar{b}$ cross-section is about three order of magnitudes lower than hadron-hadron inelastic cross-section [34]:

$$\sigma(pp \text{ inelastic}, \sqrt{s} = 14\,\text{TeV}) \sim 100\,\text{mb},$$

resulting in high-suppressed signal-to-background ratio for typical interesting processes, for instance of the order $\mathcal{O}(10^{-9})$ for the $B^0 \rightarrow K\pi$ channel. Because of the limited bandwidth available for storing data, this makes it necessary tracker and trigger systems which operate in real-time, capable to discriminate interesting

events from the huge light-quark background and therefore to select high-purity signal sample to store. Events in hadron colliders are also more complex than in B-factories, resulting in more difficult reconstruction of b-hadrons decays and requiring higher granularity detectors. Indeed, in most hard interactions only one constituent (valence or sea quark, or gluon) of the colliding hadron undergoes an hard-scattering against a constituent of the other colliding hadron: this is the leading interaction that may produce a $b\bar{b}$ pair. Others hadron constituents rearrange in color-neutral hadrons, which may have transverse momentum (i.e. momentum perpendicular to the beam pipe) sufficient to enter the detector acceptance, resulting in the so named underlying event. In the underlying event multiple hard-scattering interactions may occur between the partons consisting the same pair of colliding hadrons. Furthermore, b-hadron fragmentation process, that is the transition from a not observable single-state quark to an observable color-singlet hadron, results in a number of accompanying hadrons produced in the local region around the hadronizing quark. Fragmentation of all quarks and gluons in the event represent an important source of track multiplicity. Finally, when beams collide multiple hard interactions may occur between their hadrons, resulting in pile-up events. Each hard interaction introduces related fragmentation processes and underlying events. Similar arguments are valid for charmed hadrons, although characterized by even higher production cross-section [35]:

$$\sigma(pp \rightarrow c\bar{c}X, \sqrt{s} = 14\,\mathrm{TeV}) \approx 10\,\mathrm{mb}.$$

B-factories and hadronic collider are both interesting facilities to study CP invariance asymmetry in High Energy Physics (HEP) environment. The two approaches are complementary, with peculiar features that deeply differentiate them. B-factories are characterized by typical simple events to reconstruct, and small production cross-sections. Instead hadronic collisions allows to study a larger fraction of b-physics sector and ensure much greater production cross-section for interesting events, but events are much more complex and huge underlying background is present. We summarize B-factory and hadronic collider main parameters, concerning flavor-physics production, in Table 1.1. Cross sections of $b\bar{b}$ pair production are calculated within the detector acceptance [36, 37].

1.4   The intensity frontier

The method of testing the SM through precision measurements in flavour physics is fully complementary to that of searching for on-shell production of new particles in high energy collisions. Mixing and decay of beauty and charm hadrons occur through weak interactions, mediated by gauge bosons with masses many times larger than those of the hadrons themselves (compare, for example, the W boson mass of 80 GeV with the B mass of around 5 GeV). Other, as-yet unknown particles could also contribute, in which case measured parameters such as decay rates and CP violation asymmetries would be shifted from the SM predictions. The reach of measurements of

	$e^+e^- \to \Upsilon(4S) \to B\bar{B}$	$pp \to b\bar{b}X$
accelerator	CESR, PEP-II, KEKB	LHC (Run I)
detector	CLEO, BABAR, Belle	ATLAS, CMS, LHCb
$\sigma(b\bar{b})$	$\sim 1\,\mathrm{nb}$	$\sim 75 - 150\,\mathrm{\mu b}$
$\sigma(b\bar{b})/\sigma(\mathrm{bck})$	~ 0.25	~ 0.005
typycal ($b\bar{b}$) rate	$10\,\mathrm{Hz}$	$\sim 30 - 100\,\mathrm{kHz}$
flavors	B^0 (50%), B^+ (50%)	B^0 (40%), B^+ (40%), B_s^0 (10%), B_c^+ ($< 0.1\%$), b-baryons (10%)
boost $< \beta\gamma >$	0.06-0.6	1-10
pile-up events	0	1-20
track multiplicity	~ 5	$\mathcal{O}(100)$

Table 1.1: B-factory and hadronic collider main parameters concerning flavor physics production.

these observables is therefore limited only by precision, both experimental and on the SM predictions. Rare processes, where the SM contribution is small or vanishing, and as such has low uncertainty, are therefore of special interest. In particular, processes for which the SM contributions occur through loop diagrams, i.e. flavour changing neutral currents, are often considered golden channels for potential discoveries of physics beyond the SM.

Currently, the LHCb detector is operating at a luminosity of $4 \times 10^{32}\mathrm{cm}^{-2}\mathrm{s}^{-1}$, and will continue data taking until the end of Run 2 of the LHC, in 2018, collecting a data sample of about 9 fb^{-1}. During Long Shutdown 2 (LS2) it will be replaced by an upgraded experiment, referred as the Phase-I Upgrade (LHC Run 3, 2021-2024 and LHC Run 4, 2027-2030). The Phase-I Upgrade, operating at a luminosity of $L = 2 \times 10^{33}\mathrm{cm}^{-2}\mathrm{s}^{-1}$, will greatly improve the sensitivity of many flavour studies. However, the precision on a host of important, theoretically clean, measurements will still be limited by statistics, and other observables associated with highly suppressed processes will be poorly known. There is therefore a strong motivation for a consolidation of the the Phase-I Upgrade in view of the LHC Run 4[1], and for building a Phase-II Upgrade, which will fully realize the flavour potential of the HL-LHC during the LHC Run 5 ($\geq$ 2031) at luminosity $L > 10^{34}\mathrm{cm}^2\mathrm{s}^{-1}$ [1, 2]. The LHCb Phase-I Upgrade experiment [38] is expected to collect a sample of 50 fb^{-1} by the end of the LHC Run 4 (2030), including the LHC Run-3, while the envisioned LHCb Phase-II will collect a sample of 300 fb^{-1} by the end of Run-5 (2033). From the other side, the Belle-II experiment [39, 40] installed at the SuperKEKB accelerator (Tsukuba, Japan) [41] will also significantly contribute to shrink experimental uncertainties. It is expected to collect a sample of about 50 ab^{-1} of e^+e^- collisions data at around the $\Upsilon(4S)$ resonance by the end of 2025,

---

[1]In the current scheme no upgrades of the experiment are planned and funded in the LS3, neither for the sub-detectors nor for the data acquisition and trigger systems.

when SuperKEKB will conclude operations[2], increasing by about a factor of 50 the size of the previously collected samples from Babar and Belle experiments.

Both Belle II and LHCb experiments have entered the high intensity frontier and will significantly contribute to the search of New Physics phenomena in the next decade (and likely beyond) trough high precision measurements in the Heavy Flavour Physics. The work described in this thesis aims at contributing to the R&D effort for the Future Upgrades of the LHCb experiment (LHC Run 4 and LHC 5) with a first study of the performance of a innovative tracking device, the so called Downstream Tracker, capable of reconstructing in real-time long-lived particles.

---

[2]At the moment there are no current plans for any subsequent run of SuperKEKB accelerator or upgrades of the Belle II detector.

Chapter 2

LHCb experiment and Future Upgrades

This chapter briefly describes the Large Hadron Collider complex ,along with the present and future LHCb experiment, with a particular focus on the aspects that are more relevant to the work described in the thesis, namely the tracking and the trigger system. Further information on the LHC and the LHCb experiment can be found in the references cited throughout the chapter.

2.1 The Large Hadron Collider

The Large Hadron Collider (LHC) is a proton-proton and heavy ion collider [42] located at the CERN laboratory, on Swiss-French state border. The LHC is installed in a 27 km long circular tunnel, about 100 m underground. Protons are extracted from hydrogen gas and their energy are gradually increased by a series of accelerator machines, shown in Figure 2.1. Extracted protons are first accelerated by the Linac 2 up to an energy of 50 MeV, then by the Booster up to an energy of $1.4\,\text{GeV}$. The Proton Synchrotron (PS) and Super Proton Synchrotron (SPS) respectively accelerate them to an energy of $25\,\text{GeV}$ and $450\,\text{GeV}$. Finally protons are injected in the LHC.

In the LHC, two protons or ion beams circulate in opposite directions in two separate beam pipes. Beams are bent by more of 1,200 superconducting dipole magnets 15 m long, cooled at temperature of 1.9 K by 120 tons of superfluid helium, which generate a magnetic field of 8.3 T. Beams collide in four point placed along the LHC ring, where the detectors of the four major LHC experiments are installed. ATLAS and CMS are general-purpose experiments, while ALICE and LHCb are specifically dedicated to heavy-ion and heavy-flavor physics respectively. Other three smaller experiments are installed, TOTEM for the measure of total pp cross section, LHCf to study astroparticle physics, and MoEDAL to look for magnetic monopole. Proton beams are split in bunches each one consisting of about 10^{11} protons, and are time-spaced for a multiple of 25 ns corresponding to a bunch-crossing rate up to $40\,\text{MHz}$. The maximum number of bunches per beam is 2808, so the average bunch-crossing rate is $\sim 30\,\text{MHz}$. The peak instantaneous luminosity of the LHC
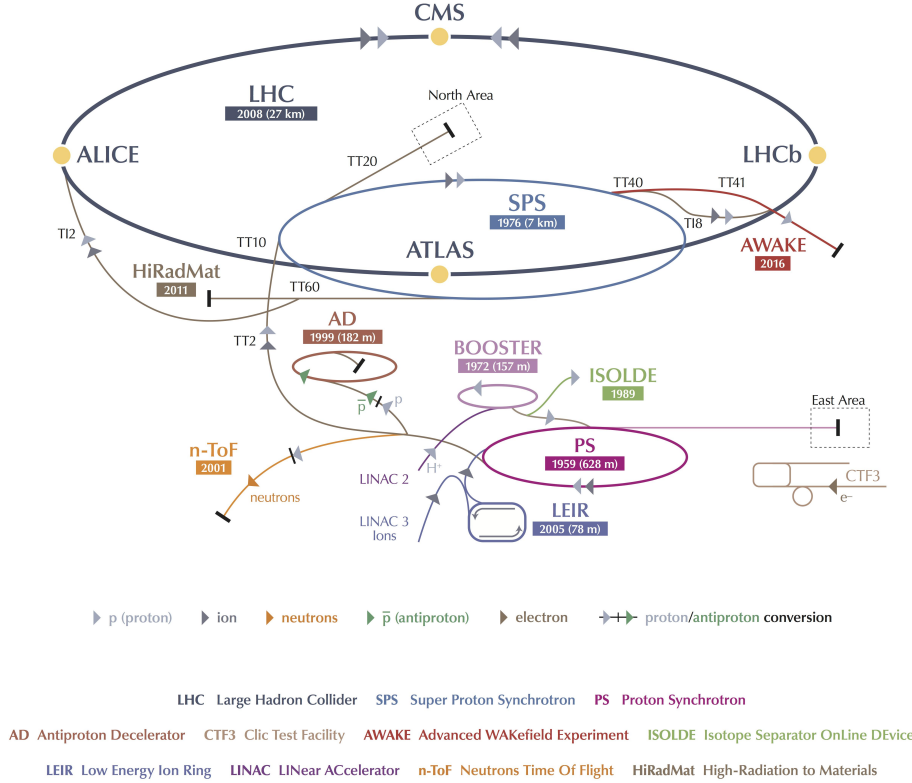
Figure 2.1: The accelerator complex at CERN is a succession of machines that accelerate particles to increasingly higher energies. Each machine boosts the energy of a beam of particles, before injecting the beam into the next machine in the sequence. In the Large Hadron Collider (LHC) the last element in this chain particle beams are accelerated up to the record energy of 6.5 TeV per beam. Most of the other accelerators in the chain have their own experimental halls where beams are used for experiments at lower energies.

project design is of $\mathcal{L} = 10^{34}\,\mathrm{cm}^{-2}\,\mathrm{s}^{-1}$ at a center of mass energy $E_{\mathrm{cm}} = 14\,\mathrm{TeV}$. As shown in tab. 2.1, all the design parameters will be achieved in 2021 during the Run 3. In 2024 LHC will be upgraded for increase significantly its luminosity entering the High-Luminosity Large Hadron Collider (HL-LHC) era. ATLAS and CMS will be upgraded to work in the new environment during the LS3. In 2021 LHCb will receive a major upgrade (LHCb Upgrade-Ia or the so-called LHCb Upgrade, Run 3). The currently LHCb baseline plan is to also run during the LHC Run 4 (2027-2029) without any upgrades during the LS3 at the same instantaneous luminosity of $2 \times 10^{33}\,\mathrm{cm}^{-2}\,\mathrm{s}^{-1}$, to integrate a total data sample of 50 fb^{-1}. However, the precision on several important, theoretically clean, measurements will still be limited

by statistics, and other observables associated with highly suppressed processes will be poorly known, at that time. Therefore, the LHCb Collaboration is currently proposing an ambitious plan of Future Upgrades: a consolidation of the the Phase-I Upgrade in view of the LHC Run 4, the so-called Phase-Ib Upgrade, and for building a major Phase-II Upgrade, which will fully realize the flavour potential of the HL-LHC during the LHC Run 5 ($\geq$ 2031) at luminosity $L > 10^{34} \mathrm{cm}^2 \mathrm{s}^{-1}$ [1, 38]. Table 2.1 recaps LHC energies and luminosities for different runs of the four major major LHC experiments.

	2010–12	2015–18	2021–23	2026–29	2031-33
LHC Run	1	2	3	4	5
E_{cm} (TeV)	$7-8$	13	14	14	14
LHC L_{peak} ($\mathrm{cm}^{-2}\,\mathrm{s}^{-1}$)	$7.7 \cdot 10^{33}$	$1.7 \cdot 10^{34}$	$2 \cdot 10^{34}$	$7 \cdot 10^{34}$	$7 \cdot 10^{34}$
LHCb L_{peak} ($\mathrm{cm}^{-2}\,\mathrm{s}^{-1}$)	$2 - 4 \cdot 10^{32}$	$2 - 4 \cdot 10^{32}$	$2 \cdot 10^{33}$	$2 \cdot 10^{33}$	$> 10^{34}$

Table 2.1: LHC parameters of pp runs from 2010 to 2033. The LHCb experiment is not limited by the number of $c\bar{c}$ and $b\bar{b}$ produced in the pp interactions but by the trigger and reconstruction efficiencies and by the amount of data that can be saved to be analysed. LHCb is, therefore, able to limit the luminosity level by shifting the colliding beams in the plane transverse to their direction, thus reducing their overlap at the collision region. Thanks to this choice, the number of pp interactions per bunch crossing can be kept lower than general purpose experiments as ATLAS and CMS, limiting the detector occupancy and facilitating the trigger selection and reconstruction.

Figure 2.2: LHCb time schedule.

2.2 The LHCb detector

The LHCb detector [43, 44] is a single-arm forward spectrometer covering the pseudorapidity range $2 < \eta < 5$, designed for the study of particles containing b- or c-quarks. The LHCb detector layout, shown in figure 2.3, is motivated by the fact that at high energies both b-hadrons are produced in the same forward or backward cone, as shown in fig. 2.4. The LHCb detector includes a high-precision tracking system consisting of a silicon-strip vertex detector surrounding the pp interaction region [45], a large-area silicon-strip detector located upstream of a dipole
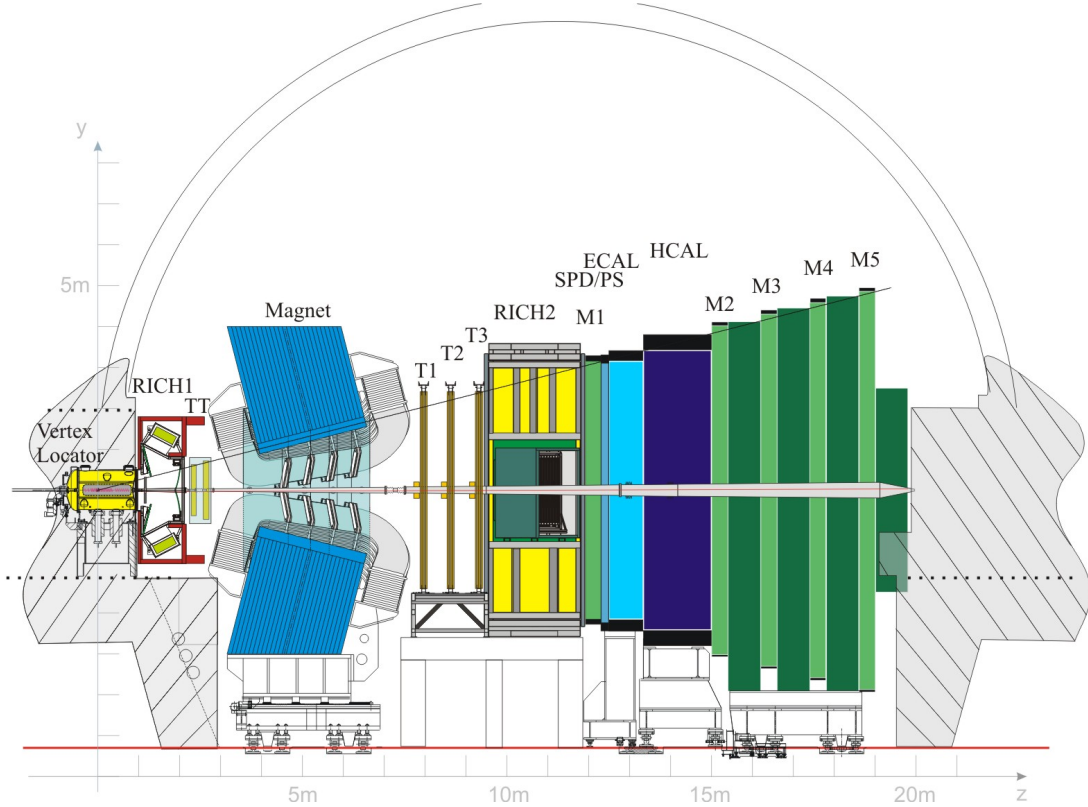
Figure 2.3: Layout of LHCb detector.

magnet with a bending power of about $4\,\mathrm{Tm}$, and three stations of silicon-strip detectors and straw drift tubes [46] placed downstream of the magnet. Different types of charged hadrons are distinguished using information from two ring-imaging Cherenkov detectors [47]. Photons, electrons and hadrons are identified by a calorimeter system consisting of scintillating-pad and preshower detectors, an electromagnetic calorimeter and a hadronic calorimeter. Muons are identified by a system composed of alternating layers of iron and multiwire proportional chambers [48]. LHCb adopts a right-handed coordinate system with z coordinate along the beam, and y coordinate along the vertical.

The nominal LHC luminosity value is reduced to $\mathcal{L} = 4 \cdot 10^{32}\,\mathrm{cm^{-2}\,s^{-1}}$ in the LHCb intersection point. Lower luminosity is obtained by appropriately defocusing the beams by moving them apart transversely. This transverse separation is progressively modified during a fill, to keep the luminosity constant as the beam current decreases. The chosen luminosity value is optimized to obtain one or two inelastic interactions per bunch crossing according to trigger bandwidth, and for limit radiation damage.

The tracking system provides a measurement of momentum of charged particles, p, with a relative uncertainty that varies from 0.5% at $20\,\mathrm{GeV}/c$ to 1.0% at $200\,\mathrm{GeV}/c$. The minimum distance of a track to a primary vertex, the impact parameter, is measured with a resolution of $(15 + 29/p_\mathrm{T})\,\mathrm{\mu m}$, where p_T is the component of the
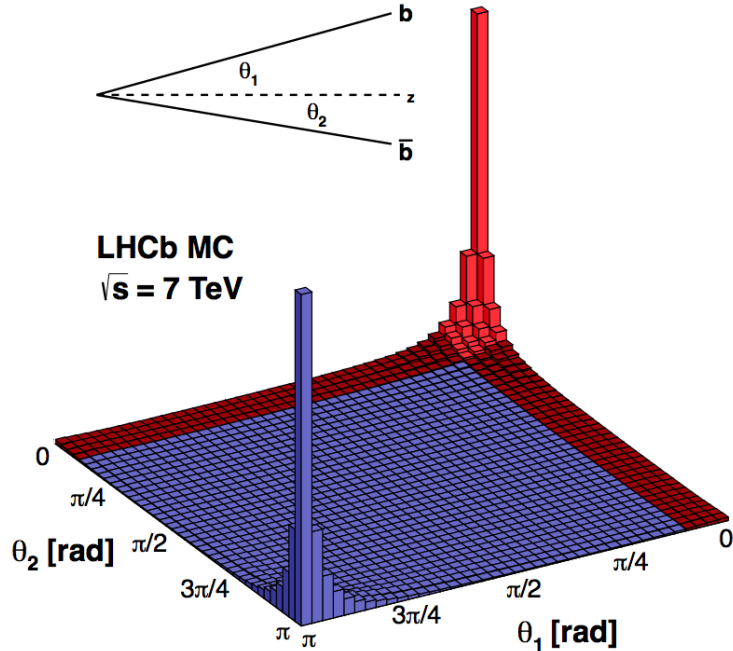
Figure 2.4: Angular correlation between b and $\bar{b}$ quarks in $b\bar{b}$ pair production, simulated with PYTHIA event generator.

momentum transverse to the beam, in GeV/c.

Next sections describe the VErtex LOcator (VELO) detector used for reconstruct primary and secondary vertexes, the spectrometer composed by the Tracker Turicensis (TT) upstream a dipole magnet, the Inner Tracker (IT) and the Outer Tracker (OT) downstream the magnet. Finally, the current trigger system is described.

2.2.1 VErtex LOcator

The VELO detector measures charged particle trajectories in the region closest to the interaction point. Its main purpose is to reconstruct primary and secondary vertexes with a spatial resolution smaller than typical decay lengths of b- and c-hadrons in LHCb ($c\tau \sim 0.01$ - $1\,\text{cm}$), in order to discriminate between them. Therefore it plays a fundamental role for discriminating heavy flavors signals from the underlying background, especially at the High Level Trigger (see Section 2.2.6). The VELO consists of 21 disk-shaped stations installed along the beam axis inside the beam pipe, both upstream ($z > 0\,\text{cm}$) and downstream ($z < 0\,\text{cm}$) of the nominal interaction point. Figure 2.5 shows the layout of the system. Stations placed at $z > 0\,\text{cm}$ provide precise measurements of vertexes positions. While the stations at $z < 0\,\text{cm}$ constitute the pile-up veto system, which provides position of primary vertices candidates along the beam-line and measures the total backward charged track multiplicity. The stations are made by two type of silicon strip sensors, the r and ϕ sensors, arranged with radial and azimutal segmentation to measure r and ϕ particle intersection
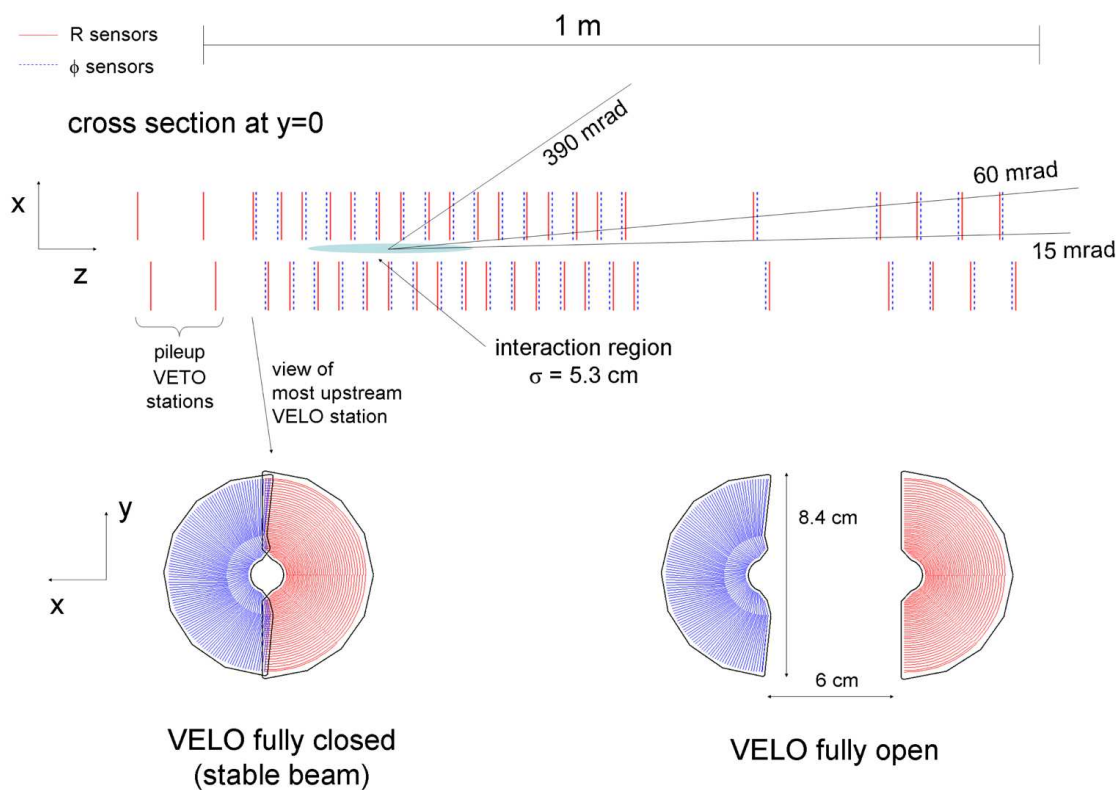
21

Figure 2.5: Representation of VELO detector, with a transverse view of a VELO station in closed and open configurations.

coordinates. Each station is divided into two retractile halves, called modules, as shown in Figure 2.5. Each halves consists of both r and ϕ sensors. VELO veto stations consist of r sensors only. The retractile halves allow to move the sensors away from the beam, to do not damage silicon sensors during LHC injection phases, when VELO stations are "opened" and the sensors have a minimum distance of 30 mm from the beam axis, instead, when stable beams are circulating for data taking, station are "closed" and the sensors reach a minimum distance of 5 mm from the beam axis.

Both r and ϕ sensors are centered around the nominal beam position, and are covering a region between 8 and 42 mm in radius. The r sensors consist of semicircular, concentric strips with increasingly pitch from 38 μm at the innermost radius to 102 μm at the outermost radius. The ϕ sensors are subdivided in two concentric regions: the inner one covers a radius r between 8 and 17.25 mm, the outer one covers r between 17.25 and 42 mm with pitch linearly increasing from the center. ϕ sensors are designed with an angular tilt of $+10°$ in the inner region and $-20°$ in the outer region, respect to the radial direction; for adjacent sensors, the tilt is reversed. This layout is designed to improve pattern recognition and to better distinguish noise from genuine hits. Each VELO module is encased in a shielding box, to protect it from the

22

radiofrequency electric field. The individual hit resolution of the sensors is strongly correlated to the sensor pitch and projected angle, that is the angle perpendicular to the strip direction. Raw hit resolution varies from $\approx 10\,\mu\text{m}$ for smallest pitch to $\approx 25\,\mu\text{m}$ for biggest pitch.

2.2.2 Tracker Turicensis

The TT uses silicon microstrip sensors, with a strip pitch of $183\,\mu\text{m}$. The sensors are $500\,\mu\text{m}$ thick, $9.64\,\text{cm}$ wide and $9.44\,\text{cm}$ long. TT is located upstream the dipole magnet, and covers the full acceptance of the experiment ($\approx 300\,\text{mrad}$). It is designed for reconstructing low-momentum tracks that are swept out of the detector acceptance by the magnet. The TT consists of one tracking station subdivided in four layers in a x-u-v-x arrangement, with vertical strips in first and last layers, and tilted strips by a stereo angle of -5° and of +5° in central layers. Each TT layer is subdivided in two half-modules, each consisting of seven silicon sensors. TT layout is shown in Figure 2.6. Single-hit resolution is of $\approx 50\,\mu\text{m}$.

2.2.3 The dipole magnet

The LHCb warm dipole magnet generates an integrated field, of about $4\,\text{Tm}$, manly along the vertical direction and between $z = 3$ and $8\,\text{m}$. A fringe field is present in the region where the tracking detectors are installed, between $z = 0$ and $10\,\text{m}$. The dipole magnet consists of two identical coils each one formed by 15 laminated low carbon-steel plates, $10\,\text{cm}$ thick. The coils, weighting a total of 54 tons, are symmetrically installed in a iron yoke of 1500 tons. A magnet perspective view is proposed in Figure 2.7. Overall dimensions of the dipole magnet are of $1\,\text{m}$ x $8\,\text{m}$ x $5\,\text{m}$. The magnet dissipates an electric power of $4.2\,\text{MW}$, and the nominal current in conductor material is of $5.85\,\text{kA}$ while the maximum permitted current is of $6.6\,\text{kA}$. Current in the magnet, and therefore the field direction, are periodically inverted, to reduce systematic effect in precision measurements of CP asymmetries.

To provide a good particle momentum reconstruction, the magnetic field intensity must be known with great precision. An array of 180 Hall probes, calibrated to a relative precision of 10^{-4} on field intensity measurement, allow to achieve a field mapping with measurement precision of about $4 \cdot 10^{-4}$ in the entire tracking volume. Measured vertical component of this magnetic field, B_y, is shown in Figure 2.8.

2.2.4 Inner Tracker

The IT detectors is located downstream the dipole magnet, and it consists of 3 cross-shaped stations, it covers an acceptance of $\sim$ 150-200 mrad in the bending plane and of $\sim$ 40-60 mrad in the yz plane. The IT reconstruct tracks that passed through the magnetic field region lying near the beam axis. It uses the same microstrip sensors used in the TT. Like the TT, each IT station is subdivided in four layers in a x-u-v-x arrangement. Each IT layer consists of four subunits, positioned around
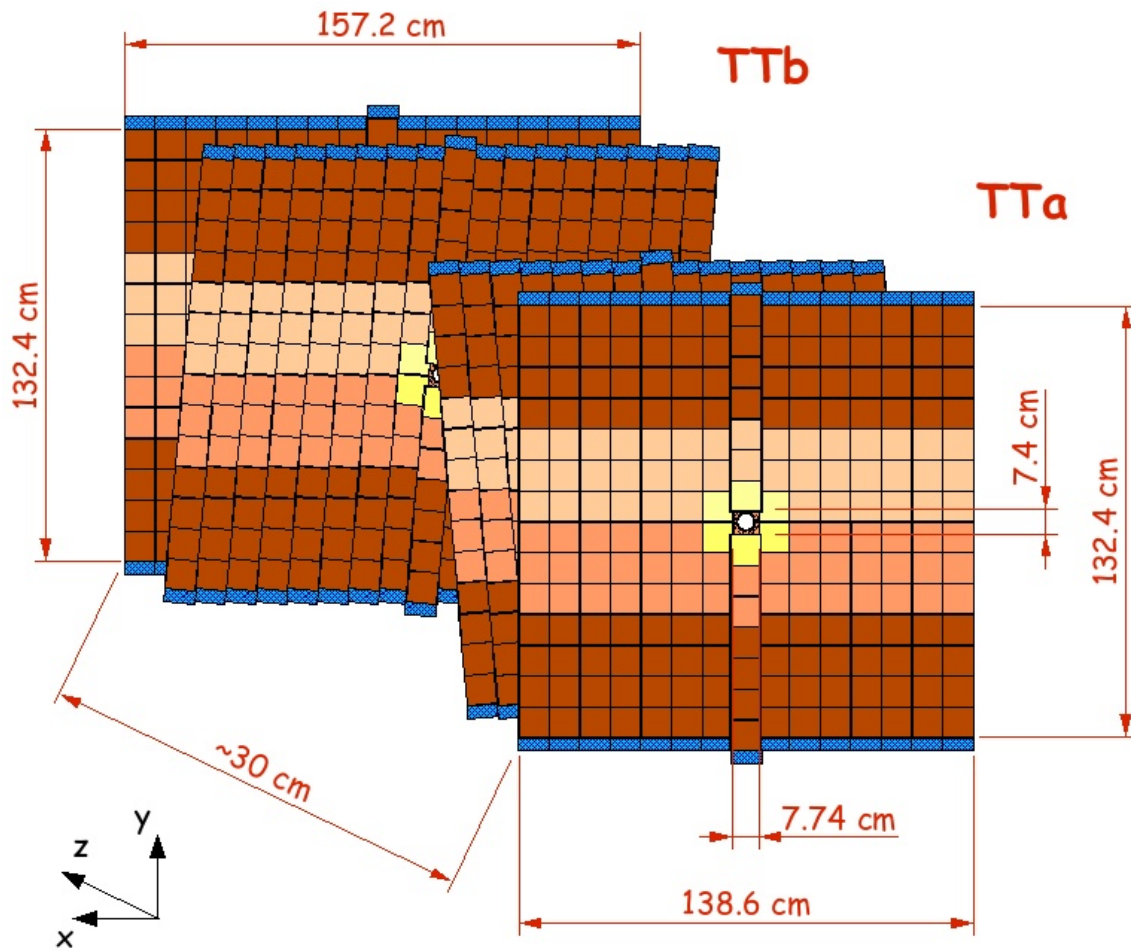
Figure 2.6: Layout of TT.

the beam pipe, and each subunits includes seven modules. In the subunits above and below the beam pipe a module corresponds to one silicon sensor, while subunits on right and left have modules with two silicon sensors each one. IT layout is shown in Figure 2.9. Single-hit resolution of IT detectors is of $\approx 50\,\mu$m.
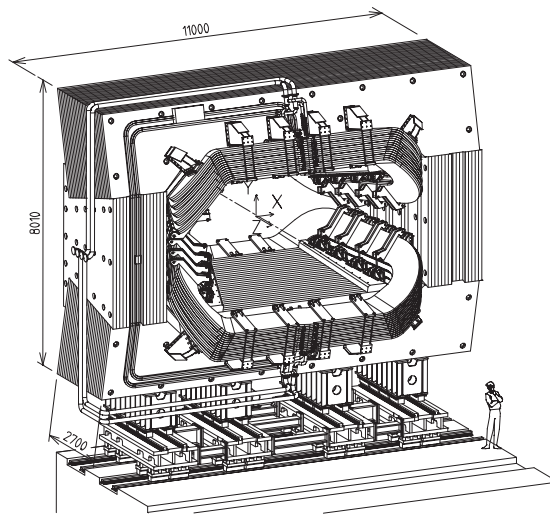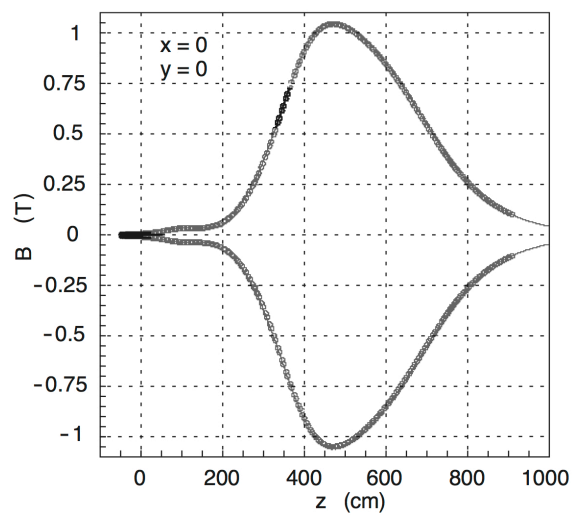
Figure 2.9: Layout of one IT layer.

2.2.5 Outer Tracker
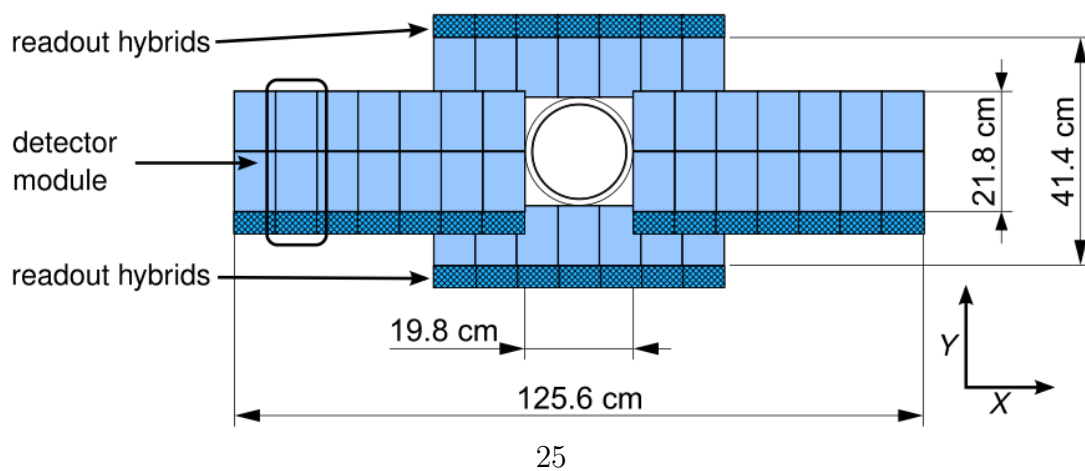
The OT is used to measure track bending in the acceptance region not covered by the IT subdetector. The OT consist of three straw tubes stations, each station is located downstream a IT station, which together form a T-station. OT layout is shown in Figure 2.10. Each OT station is subdivided in four layers x-u-v-x. Each layer is subdivided in modules, consisting of 64 straw tubes. Straw tubes are filled with a mixture of 70% Ar and 30% CO_2, with a drift time up to 50 ns. The straw tubes allow to reconstruct tracks with a spatial resolution of $\approx 200\,\mu$m.
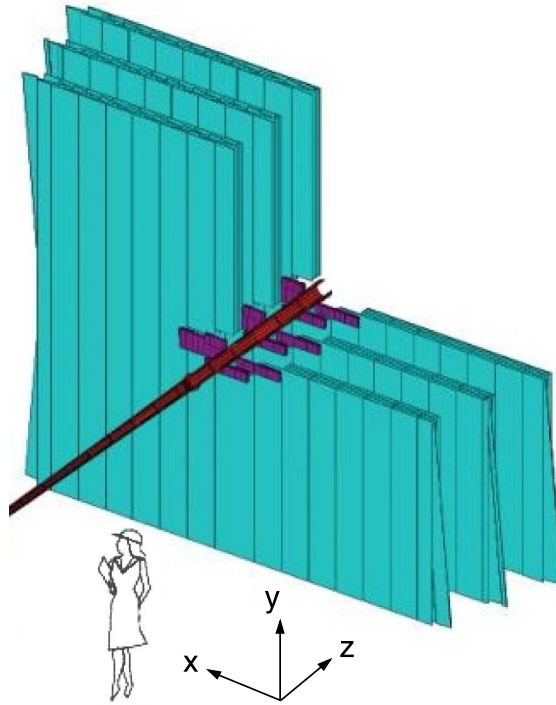
Figure 2.10: Layout of OT subdetector. The IT in purple.

2.2.6 Trigger

The LHCb trigger was designed to select heavy-flavor decays from the huge light-quark background, sustaining the LHC bunch-crossing rate of 40 MHz and selecting up to 5 kHz of data to store [49]. Only a small fraction of events, about 15 kHz, contains a b-hadron decay with all final state particles emitted in the detector acceptance. The rate of "interesting" bottom hadron decays is even smaller, of a few Hz. Corresponding values for charmed hadrons are about 20 times larger. It is therefore crucial, for the trigger, to reject background as early as possible in the data flow.

The LHCb trigger is organized into two sequential stages, the L0 trigger and the High Level Trigger (HLT). This two-level structure helps coping with timing and

selection requirements, with a fast and partial reconstruction at low level, followed by a more accurate and complex reconstruction at high level. The hardware-based L0 trigger operates synchronously with the bunch crossing. It uses information from calorimeter and muon detectors to reduce the 40 MHz bunch-crossing rate to below 1.1 MHz, which is the maximum value at which the whole detector can be read out by design. Then, the asynchronous software-based HLT performs a finer selection based on information from all detectors, and reduces rate to 5 kHz, after an upgrade to the storage in Run 2 the output rate was increased to 12 kHz. Figure 2.11 shows the LHCb trigger flow for Run 1 and Run 2, and typical event-accept rates for each stage.
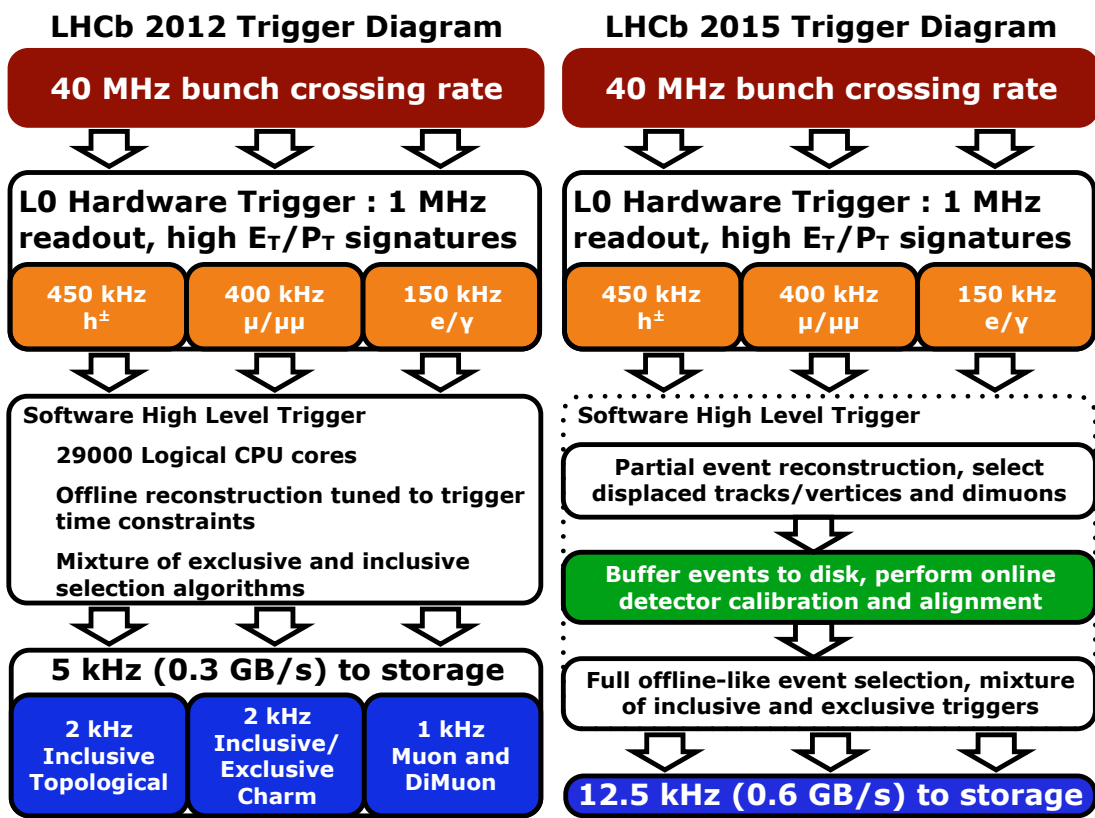
Figure 2.11: Representation of LHCb trigger flow and typical event-accept rates for each stage.

The L0 trigger

The task of L0 trigger is to reduce the event rate from 40 MHz (same as the bunch-crossing rate) to 1 MHz, that is the maximum rate at which the full detector can be read. Data from all detectors are stored in memory buffers consisting of an analog pipeline that is read out with a fixed latency of 4 μs. The L0 decision must

be available within this fixed time, therefore the L0 trigger is entirely based on custom-built electronic boards, relying on parallelism and pipelining. At this stage, trigger requests can only involve simple and immediately available quantities, like those provided by calorimeter and muon detectors. The L0 trigger consists of three independent trigger decisions, the *L0 hadron*, the *L0 muon*, the *L0 calorimeter*. Each decision is combined with the others through a logic "or" in the L0 decision unit.

The L0 hadron trigger aims at collecting samples enriched in hadronic *c*- and *b*-particle decays. Final-state particles from such decays have on average higher transverse momenta than particles originated from light-quark processes, and this property helps in discriminating between signal and background.

The L0 muon trigger uses the information from the five muons stations, to identify the most energetic muons. Once the two muons candidates with highest transverse momentum per quadrant of the muons detectors are identified, the trigger decision depends on two thresholds: one on the highest transverse momentum (L0 muon) and one on the product of the two highest transverse momenta (L0 dimuon).

The L0 calorimeter trigger uses the information from the electromagnetic calorimeter, the hadron calorimeter, the preshower detector, and the scintillator pad detector. It calculates the transverse energy $E_{\rm T}$ deposited in a cluster of 2x2 cells of the same size, for both the electromagnetic calorimeter and the hadron calorimeter. The transverse energy is combined with information on the number of hits on preshower and scintillator pad detectors to define three types of trigger candidates, photon, electron, and hadron.

The High Level Trigger

Events accepted at L0 are transferred to the Event Filter Farm (EFF), an array of computers consisting of more than 15,000 commercial processors, for the HLT stage. The HLT is implemented through a C++ executable that runs on each processor of the farm, reconstructing and selecting events in a way similar to the offline processing. A substantial difference between online and offline algorithms is the time available to completely reconstruct a single event. The offline reconstruction requires almost 2 s per event in average, while the maximum time available for the online reconstruction is typically 50 ms, determined by the L0 event-accept rate (870 kHz in 2011) and the computing power of the farm.

The HLT consists of several trigger selections designed to collect specific events, in particular, *c* or *b*-hadron decays. Every trigger selection is specified by reconstruction algorithms and selection criteria that exploit the kinematic features of charged and neutral particles, the decay topology, and the particle identities. The HLT processing time is shared between two different levels, a first stage called HLT1 and a second stage HLT2. A partial event reconstruction is done in the first stage in order to reduce the event accept rate to 30 kHz, and a more complete event reconstruction follows in the second stage.

At the first level, tracks are reconstructed in the VELO and selected based on their probability to come from heavy-flavor decays, by determining their impact

parameter with respect to the closest primary vertex. At the second level, a complete forward tracking (see following section) of all tracks reconstructed in the VELO is performed. Secondary vertex reconstruction is performed and requirements on decay length and mass are applied to reduce the event-accept rate to 5 kHz, at which events are stored. Several trigger selections, inclusive and exclusive, are available at this stage.

2.3 LHCb tracking

The LHCb tracking reconstruction is currently performed in stages [50]. First, tracks are reconstructed as straight lines using the R sensors of the VELO. Then, hits from the ϕ VELO sensors are added to these tracks. Two different algorithms are used to combine these VELO tracks with hits in the other tracking stations. The first method propagates VELO tracks through the magnetic field, and adds hits in the downstream tracking stations (forward). The second method finds straight track segment in the downstream tracking stations (track seeds) and then attempts to propagate them in the opposite direction, matching them to VELO tracks (backward). Finally, hits from the TT (UT in the LHCb Upgrade) are added to the track to improve the momentum resolution and reject incorrect combinations of hits.
Within the LHCb tracking environment, tracks are classified as follows:

- **long track**: a track reconstructed both in VELO and T-stations subdetectors;

- **upstream track**: a track reconstructed both in VELO and TT subdetectors;

- **downstream track**: a track reconstructed on TT (or UT in the Upgrade era) and T-stations subdetectors;

- **T-track**: a track reconstructed on T-stations only;

- **VELO-track**: a track reconstructed on VELO only.

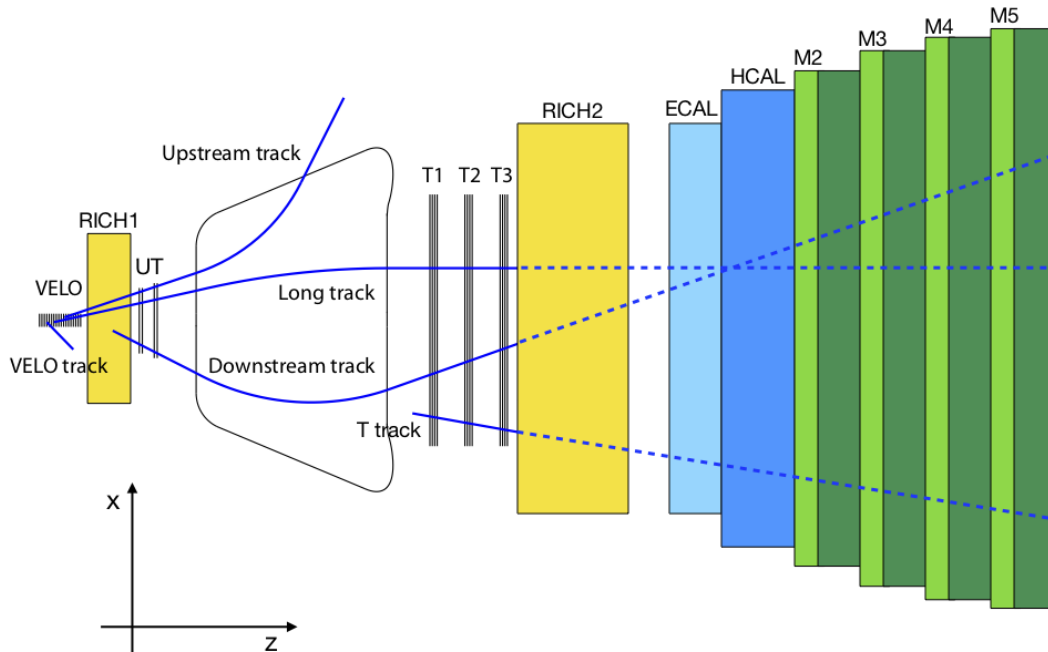Figure 2.12 shows a representation of this track classification.

Figure 2.12: LHCb tracking scheme in the $x - z$ view. The scheme will remain almost unchanged moving from the current LHCb to the LHCb Upgrade. In particular the figure refers to the LHCb Upgrade, where the TT sub-detector will be replaced by a new silicon micro-strips detector, the Upstream Tracker (UT), while both the Outer and the Inner Tracker in the forward region (the so-called T-Stations) will be replaced by the new Scintillating Fibre Tracker (SciFi Tracker). Also the VELO will be replaced be replaced by a detector based on silicon pixel technology (VELOPIX).

2.4 The LHCb Upgrade-I

With the intent of collect $50\,\text{fb}^{-1}$ in Run 3 and Run 4, during the Long Shutdown 2 of the LHC collider $(2019 - 2020)$, the LHCb experiment will receive substantial upgrades concerning both detector and online systems [51]. After the upgrade, the readout rate will be Among the major changes, there will be the upgrade of the readout system, capable to readout the whole detector at $40\,\text{MHz}$ instead of the current frequency of $1.1\,\text{MHz}$, and the development of a purely software-based trigger. This will allow a huge increase of data rate, leading to important improvements in annual signal yields, but will also enormously increase the demands on EFF and off-line processing. Other important upgrades will concern all the LHCb subdetectors. All upgrades must take into account the new experimental environment, with a

center-of-mass energy of $\sqrt{s} = 14\,\text{TeV}$ and an important increase of luminosity, set to $\mathcal{L} = 2 \cdot 10^{33}\,\text{cm}^{-2}\,\text{s}^{-1}$ in order to reach the desired goal of $50\,\text{fb}^{-1}$ collected. This results in a much higher track multiplicity then nowadays, and in an average number of primary pp interactions per bunch crossing equal to $\mu = 7.6$ that will require new detectors with greater granularity to maintain a good track reconstruction performance.

The VELO and the TT will be replaced respectively by the VELOPIX and the Upstream Tracker (UT). The IT and the OT will be replaced by the Scintillating Fibre Tracker (SciFi). In addition, the amount of off-line processing that will be feasible for each event in these new conditions will be more limited than in the past, and the plan is to perform most, if not all, of the tracking reconstruction work within the HLT process in real-time. This further increases the demands on the EFF, and will require some compromise on reconstruction strategies, as it will be further discussed later.
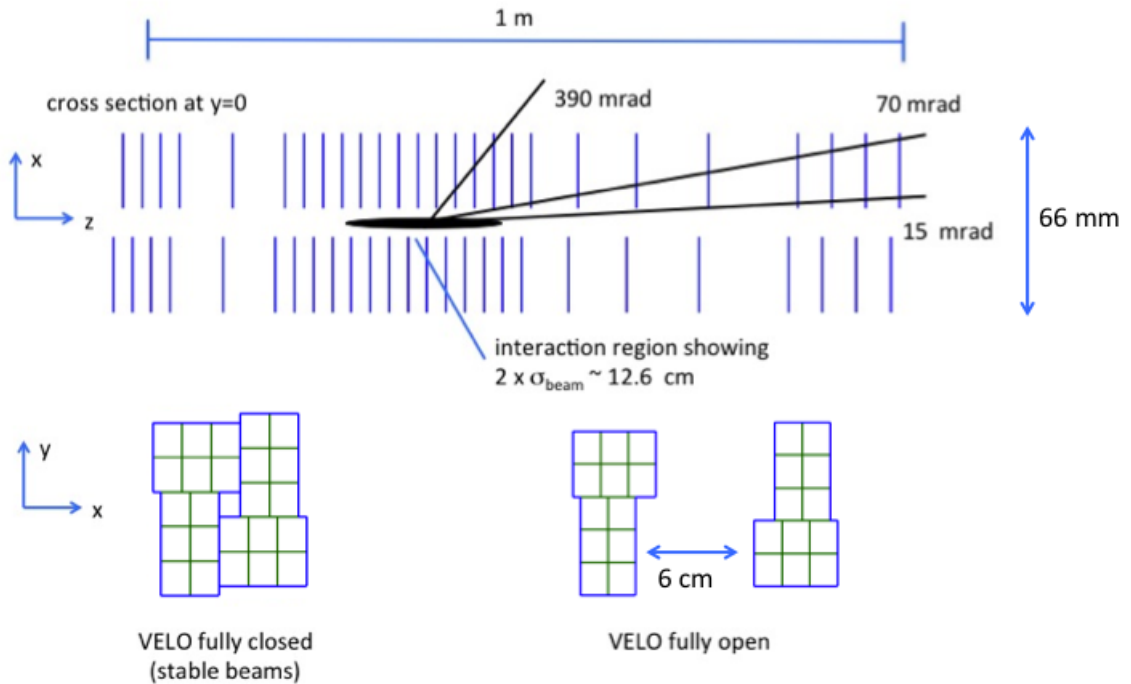
2.4.1   VELOPIX detector

Figure 2.13: Layout of VELOPIX.

The VELO will be replaced by a detector based on silicon pixel technology (VELOPIX [52]). The VELOPIX consists of 26 tracking layers, as shown in Figure 2.13, and two of them are pile-up stations used to measure backward track multiplicity. Each station is subdivided in two modules, with the ability of distancing them from the

beam axis such as for the current VELO detector. Each module contains four silicon sensors with an active area of 42.46 x 14.08 mm^2. The pixel sizes are 55 x 55 μm^2 and the entire VELOPIX detector includes about 41 M pixels. The inner radius of sensitive area from beam axis will be reduced from current $r = 8.2$ mm to less of $r = 5.1$ mm, to improve impact parameter resolution. The single hit resolution is expected to be about $12 - 15$ μm for both x and y coordinates.

2.4.2 Upstream Tracker
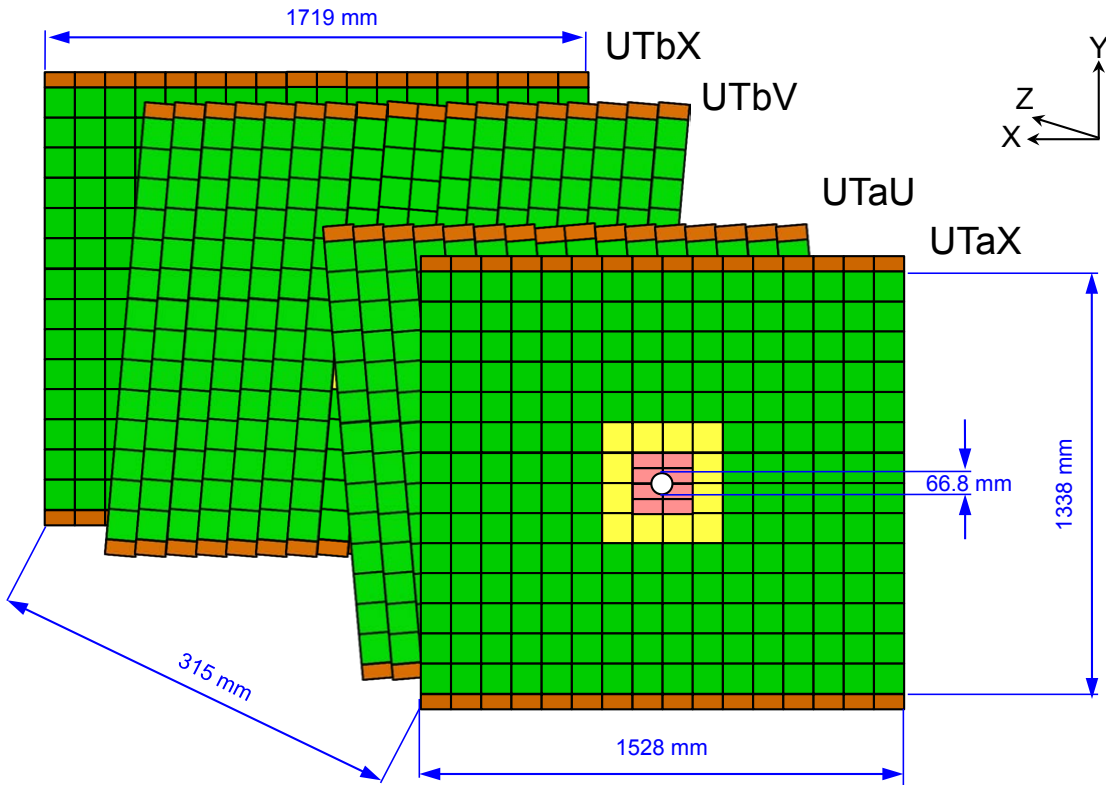
Figure 2.14: Layout of UT detector.

The current TT will be replaced by the UT [7], a new detector consisting of four planes of silicon micro-strips. With respect to the TT, UT planes use thinner sensors (250 μm $vs.$ 500 μm) with finer segmentation in the central region (95 μm $vs.$ 183 μm), and provide a larger acceptance coverage. UT planes are arranged in a x-u-v-x configuration, with vertical strips in the first and last layers, and tilted strips by a stereo angle of -5° and of +5° in the central layers. Pitches and lengths of sensors vary depending on their position. Around the beam pipe, sensors with 95 μm pitch and 5 cm long are used, while in central areas we have sensors with 95 μm pitch and 10 cm long. Finally, more externally sensors with 190 μm pitch and 10 cm long

are used. Figure 2.14 shows the UT layout. Angular coverage of UT detector is of 314(248) mrad in the bending (non bending) plane.

2.4.3   Scintillating Fibre Tracker

Since the Scintillating Fibre Tracker is the most relevant sub-detector for this thesis work, its layout and readout, along its performance, are accurately described, much more than other sub-detectors.

The tracking detectors upstream (UT) and downstream (SciFi Tracker) of the dipole magnet have to provide high precision momentum measurements for charged particles. With this information precise mass and lifetime resolutions of decaying particles can be determined. As described in the previous sections the upgraded LHCb detector is planned to run with an increased instantaneous luminosity of $2 \cdot 10^{33} \text{cm}^{-2} \text{s}^{-1}$, 25ns bunch crossing and an average number of proton-proton interactions per bunch crossing of about five. The current Tracking System was designed to operate with an instantaneous luminosity of $2 \cdot 10^{32} \text{cm}^{-2} \text{s}^{-1}$ and assures that the occupancy in the hottest region is limited to 10%. However, improvements to the track reconstruction algorithms allowed data collection at an instantaneous luminosity of $5 \cdot 10^{32} \text{cm}^{-2} \text{s}^{-1}$ with an increased maximum occupancy of 25% and no loss in the track finding efficiency [7]. A high hit efficiency, good spatial resolution in the bending plane of the magnet and low material budget in the acceptance is highly required by the track reconstruction. Furthermore the LHCb upgrade demands to operate during the full lifetime of the upgraded LHCb detector and for the FE electronic to work at 40MHz. Summarized, the strongest requirements for an upgrade of the T-stations, as listed in the LHCb Tracker Upgrade TDR [7], are:

- Hit detection efficiency as large as possible (about 99%). The reconstructed noise cluster rate at any location of the detector has to be in addition well below ($< 10\%$) the signal rate at the same location.

- Spatial resolution below 100μm in the bending plane of the magnet.

- Radiation length $X/X_0 \leq 1\%$ per tracking layer to minimise multiple scattering and have that effect smaller than in the tracking system upstream of the magnet.

- FE electronics running with the LHC clock at 40MHz. Short recovery times should minimize inefficiencies due to dead-time.

- Operate with the required performance the full lifetime of the LHCb upgrade with an integrated luminosity of 50fb^{-1}.

Despite of that, it is shown in Ref. [53] that the detector occupancy of the OT becomes too high at higher luminosities. An operation at such luminosities would require either replacing some OT modules by shorter ones, or using a detector with higher granularity. Nevertheless, all read out electronics of the IT and OT would need to be replaced to allow a triggerless read out of the complete LHCb events

at 40MHz. The evolution of this major tracking upgrade through several stages. At the end of 2013 it was chosen to replace the tracking stations by a Scintillating Fibre Tracker (SciFi Tracker). This complete new detector technology will cover the full acceptance after the magnet. Scintillating fibres with a length of 2.4m and a diameter of 250μm will be the active material of this detector and will be stacked to fibre mats with 6 layers. These detector modules are going to be read out with Silicon Photomultipliers (SiPM).
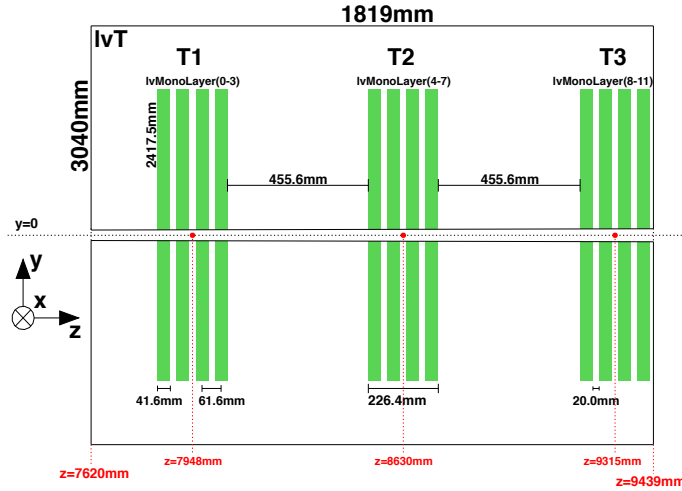

Figure 2.15: Arrangement of the SciFi within the tracker volume in the $x - z$ view.
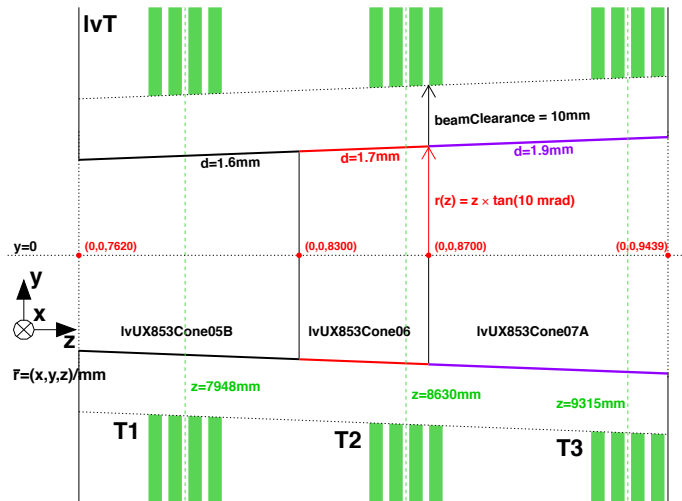

Figure 2.16: Arrangement of the SciFi within the tracker volume in the $x - z$ view. Zoom around the beam pipe.

The SciFi Tracker will be located between the LHCb magnet and RICH2 and the space is constrained by the one currently used by the IT and OT. The SciFi Tracker

will have three stations (T1, T2, T3) which are composed of four detection layer with a $x - u - v - x$ geometry like shown in Fig. 2.17. Each detection layer will have a rectangular stepped hole in the center to incorporate the beam pipe structure. The detection layers are separated into 10 to 12 modules per layer, which host the active material consisting of eight fibre mats. The fibre mats consist of 6 layers of densely packed blue-emitting scintillating fibres with a diameter of 250 μm. The scintillation photons are guided through the fibres and their detection is realised by multichannel Silicon Photomultipliers (SiPM) with rectangular channels of 250 μm. The read-out of the SiPMs is based on a custom-designed ASIC chip which integrates the signal over 25 ns.
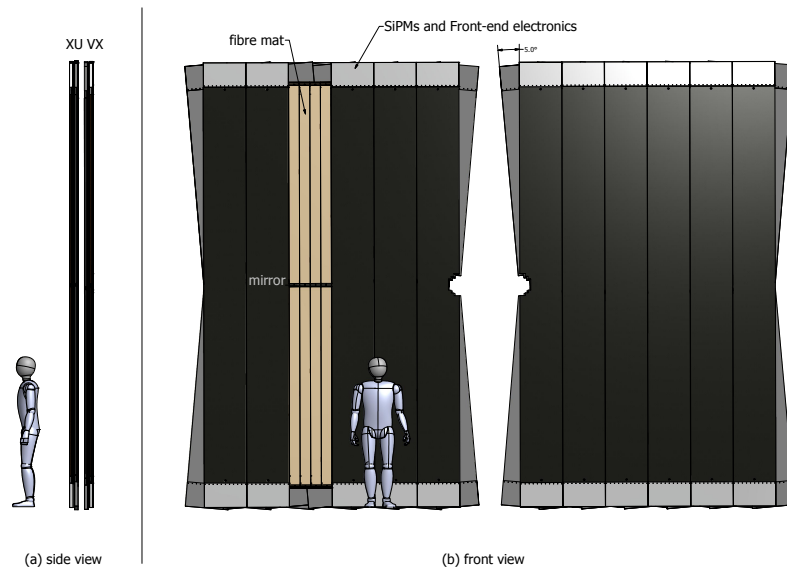
Figure 2.17: Schematic view of one station of the SciFi Tracker.

The fibres are supported by sandwich panels. The SiPMs are housed in a closed volume and cooled to -40 °C. When a particle passes through a fibre mat it deposits energy in more than one fibre. The scintillation photons travel along the fibres and are detected by multichannel SiPMs. To reduce the noise, thresholds are applied in the electronics and clusters are formed, see Fig. 2.18. The hit position is calculated as the weighted average in a cluster which improves the spacial hit resolution. The most important characteristics of the SciFi Tracker are the hit detection efficiency and spatial resolution, which are dominated by the overall light yield of the photon detectors. The spatial resolution is provided by the width of SiPM channels and therefor nominal 250 μm $/\sqrt{12} = 72$ μm. However the spatial resolution depends also on manufacturing tolerance of the fibre mats and modules. Providing a high

signal to noise ratio is necessary to achieve the highest possible hit detection efficiency. In addition with the clustering procedure, a spatial resolution better than 100 μm can be achieved. Though, the hit efficiency depends on the number of photons reaching the fibre end and getting detected. Thus, a mirror is paced at one side of the fibre mat, so that photons emitted in the opposite direction of the SiPM have the chance to get detected as well.
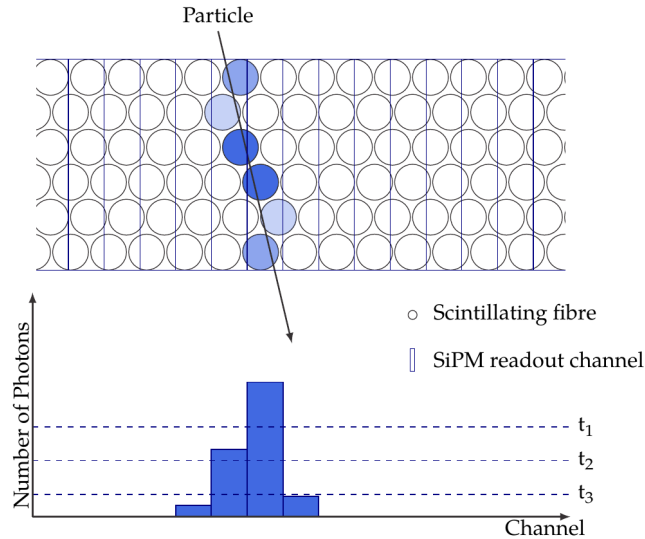
Figure 2.18: SciFi clustering procedure. A crossing particle typically creates photons in more than one channel. The signal gets discriminated by three different thresholds (t_1, t_2, t_3). Channels which exceed the seed threshold t_2 are selected. If the sum of neighbouring channels above the neighbour threshold t_3 is higher than the sum threshold t_1 these channels are forming a cluster. The actual hit position is calculated as the weighted of all channels inside this cluster.

For the SciFi Tracker scintillating fibres with a round cross section of the type SCSF-78MJ from the company Kuraray are used. A schematic of the fibre is shown in Fig.2.19 They have been chosen for their fast decay constant of 2.8 ns and their high light yield. These are multicladded plastic fibres. The core is based on polystyrene with additives. The claddings have descending refractive indices to enable light transport via total refraction. The inner cladding is used as linkage to the outer one, which would not be compatible with the core. The amount of light produced scales with the deposited energy. The photons produced travel along the fibre in both directions. To increase the light yield at the SiPMs, the fibres are mirrored at the inner end of the detector. This extends the maximum signal travel time in the fibre. The effective travel speed along the fibre is 6 ns m^{-1}, which gives 30 ns for 5 m.

The fibre transparency and therefore the light guiding procedure is decreased by the radiation environment in the LHCb cavern. In Fig 2.20, the integrated ionising dose after an integrated luminosity of 50 fb^{-1} is shown. It peaks close to the beam

pipe at 35 kGy for T1 and drops steeper than exponential to the outer regions. From results seen in irradiation measurements performed by the LHCb SciFi group, the total expected loss of signal near the beam pipe is expected to be 35 %. The typical light yield of an unirradiated SciFi module at the mirror is about 16-20 photoelectrons. The best performing modules will be selected to be placed in the central region of the SciFi tracker, where the dose is the highest. Nevertheless after 10 years of operation in the most irradiated region at the mirror, a light yield of about 12 photoelectrons is expected. For this reason six layers of fibres have been chosen to be the best solution of having a high light yield without exploiting the material budget. The nominal diameter of the fibres is 250 μm, but however short parts of the fibre can exceed this to above 400 μm, so called bumps. These bumps are an issue in the production of the fibre mats.
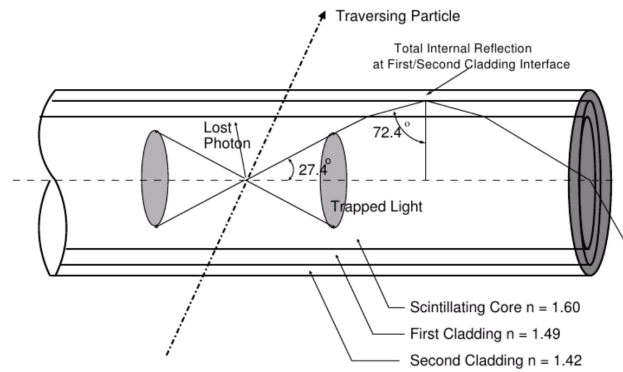

Figure 2.19: Fibre schematic. Light is produced in the core material and then trapped and propagated within the fibre through total internal reflection. The claddings have decreasing indices of refraction.
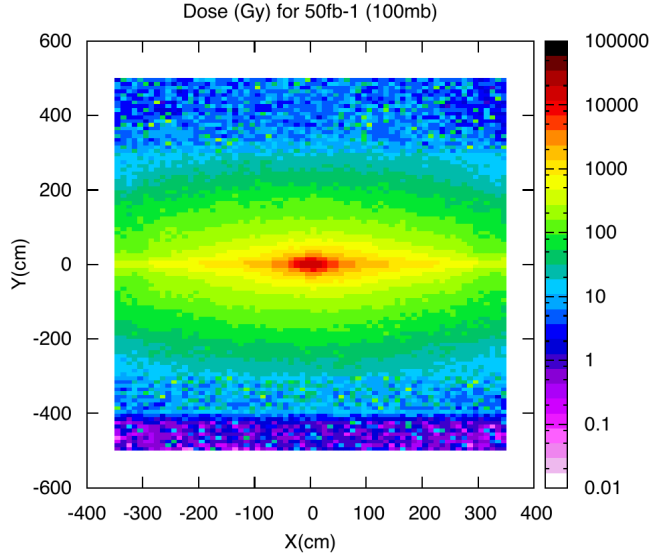
Figure 2.20: Simulated dose distribution in Gy at the position of T1 for 50 fb^{-1}.

The specific electronics for the LHCb SciFi Tracker are separated in front end and back end. As the front end electronics are directly situated at the detector as part of the module, the back end electronics will be placed outside the LHCb cavern in the counting house. The FE boards interface on the one side directly to the SiPMs and to the experiments data-acquisition and control system on the other side. The FE electronics provide a digitisation of the SiPM signals and perform the clustering. On the back end side these data are processed. As shown in Fig. 2.21 on the FE board a custom designed ASIC called the low-Power ASIC for the Scintillating FIbres traCker (PACIFIC) is situated along with an FPGA (Field Programmable Gate Array)responsible for the clustering algorithm. The signal of each SiPM is amplified, shaped and integrated over the 25ns LHC bunch crossing rate in the PACIFIC chip. Afterwards a fast clustering algorithm is executed on the FPGA to reduce the data volume. These formed clusters are transferred to the back end electronics by a GBT (GigaBit Transceiver), subsequently. Each PACIFIC is assigned to one SiPM dye (64 channels) and will have the same granularity. It uses two interleaved gated integrators to avoid dead time. Hence, the goal is to process all photons of a particle hit, but the output is also dependent on the arrival time of the photon inside the SiPM. As already mentioned before, the maximum travel time for a photon inside the scintillating fibre can be 30ns, therefore photons can also arrive outside the 25ns integration window and will be assigned to the next bunch crossing [7]. To distinguish signal from noise a fast clustering algorithm is executed on FPGAs. It also serves as zero suppression and hence reduces the required bandwidth after the ASIC. The typical signal created by a particle crossing a fibre mat is dispersed over several fibres and therefore a few SiPM channels, see Fig. 2.18. The mean position of this cluster is the best estimate of the hit position. The cluster algorithm provides

three different thresholds. Each signal exceeding the *seed threshold* (e.g. 2.5p.e.[1]) is directly accepted. In addition one neighboring channel on the left and on the right is accepted if their signal is above the *neighbor threshold* (e.g. 1.5p.e.). The cluster is finally accepted if the total signal height inside the cluster exceeds the *sum threshold* (e.g. 4.5p.e.) [54].
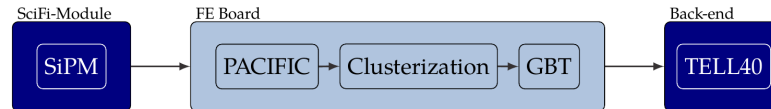

Figure 2.21: Scheme of readout electronics. The signal of one SiPM gets digitised, shaped and integrated via the PACIFIC ASIC. Afterwards clusters are formed via a fast algorithm on Field Programmable Gate Arrays and transferred to the back end electronics with a GigaBit Transceiver.

The module geometry technology has been chosen such that the requirements addressed before can be achieved. Single scintillating fibres with a diameter of $250\mu m$ are glued to a matrix with 6 layers to produce a sufficient signal amplitude and hit resolution. Low occupancy is provided by the small spacing of the fibre matrix and the narrow SiPM channels. A support structure composed of a carbon fibre, honeycomb sandwich structure ensures a light and stable detector. With cooled photo-detectors noise and false clusters are being reduced. A SciFi Tracker module consists of 2×4 fibre mats. Hence, four mats are arranged next to each other while two are sitting one upon the other. At the height of the beam pipe the fibre mats have a mirrored end, to increase the light yield on the other side, where the photo-detectors are located. The SiPMs are situated in a so-called Read Out Box, where their cooling is realized and the FE electronics is housed. A typical SciFi module is 5m tall with a width of 0.52m.

2.4.4 The Data acquisition in the LHCb Upgrade-I

The Trigger system and event reconstruction will be fully software based on the HLT [38]. Figure 2.22 shows the trigger scheme for LHCb Upgrade-I. All needed hardware will be installed on the surface, and it will be consist of an Event-Builder (EB) and the EFF. The full system is visible in Figure 2.23.

The Event-Builder

The EB collects data from the detector, and sends data packets to the EFF. Data movement inside the EB is performed by commercial CPUs organized in 500 rack-mounted PC boxes [38]. Every node will mount a PCIe40 board for receiving data from the detector and two network interfaces, one connected to the EB network and one to the EFF. The PCIe40 is a custom board carrying an Altera Arria 10 Field

---

[1]It is very unlikely that noise could reach that signal height

LHCb Upgrade Trigger Diagram
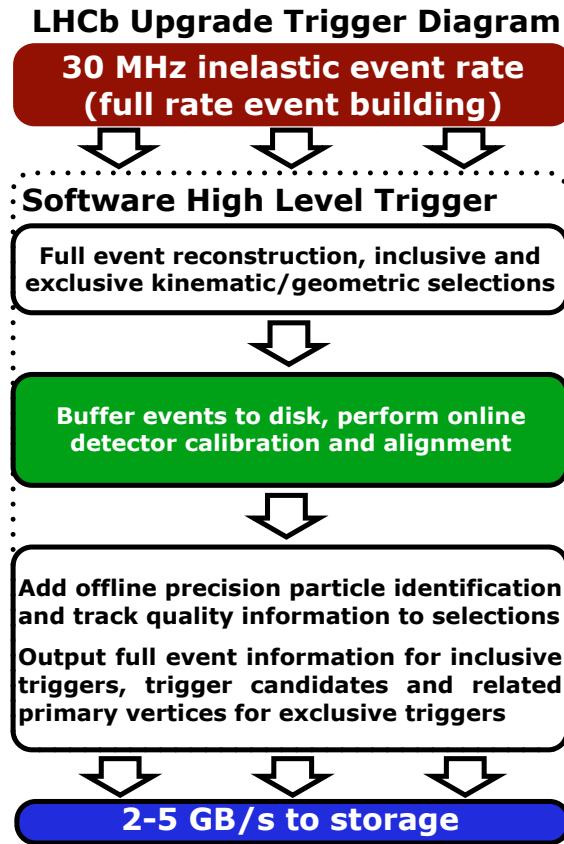
Figure 2.22: Representation of LHCb Upgrade 1a trigger flow and typycal event-accept rates for each stage.

Programmable Gate Array (FPGA) used for receiving and reformatting the data coming from the detector front-end. The board can be connected up to 48 optical links. Data are pushed by the PCIe40 FPGA into the main-memory of the EB PC. Data from several bunch-crossings are grouped together into a multi-event fragment packet (MEP) to ensure efficient link-usage. A single node receives through the EB network all MEPs containing data from the same bunch crossing and builds the events merging all the packets together. Each EB node then sends the events to a sub-farm of the EFF, where the High Level Trigger will process them. Each node will send an event every $\sim 13\,\mu$s. Figure 2.24 shows the data-flow in the EB server.

The Event Filter Farm

The EFF will be responsible for reducing the event-rate from the 30 MHz of colliding bunches to the accepted output rate of the storage. The baseline EFF will have 1000 servers running the HLT software. It is estimated that in 2020, using multicore CPU, a server will be able to run 400 HLT instances. Thus the maximum processing time allowed for each event in the EFF is 13 ms [38]. The trigger system will use track

Figure 2.23: The architecture of LHCb Upgrade-I readout-system.

Figure 2.24: Data-flow in the Event-Builder server.

Offline Tracking	Online Tracking
Velo tracking	**Velo tracking**
	Velo-UT tracking p_T > 200 MeV, ðp/p ~ 15%
Forward tracking p_T > 70 MeV, ðp/p ~ 0.5%	**Forward tracking** p_T > 500 MeV, ðp/p ~ 0.5%
PV finding	**PV finding**
	Rate reducing cuts Output < 1 MHz
	Muon Identification
Full Kalman fit	**Simplified Kalman fit**
Particle Identification	**Particle Identification**
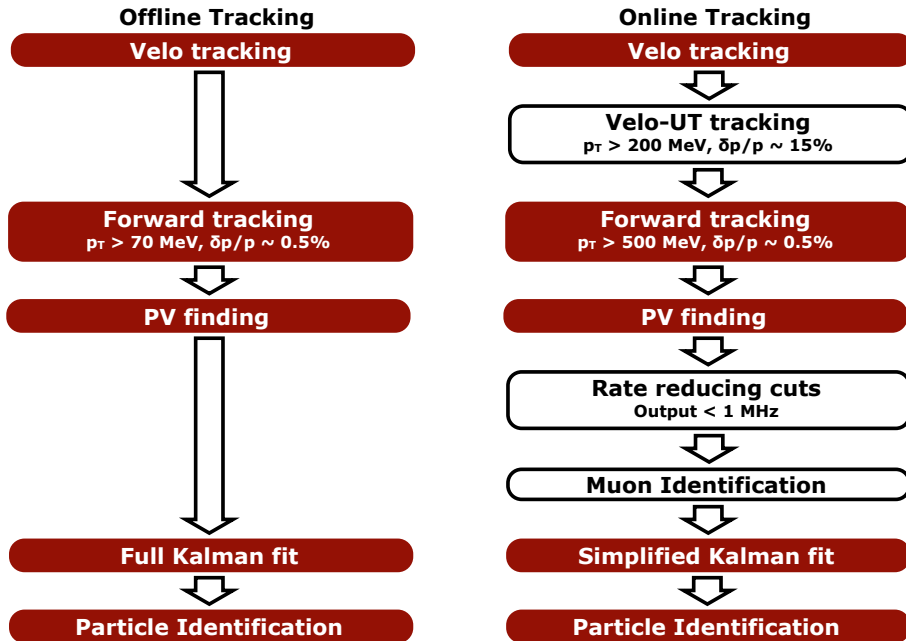
Figure 2.25: Track reconstruction sequences used (left) in the offline and (right) in the online trigger reconstruction. The offline reconstruction considers all VELO tracks for extension in the SciFi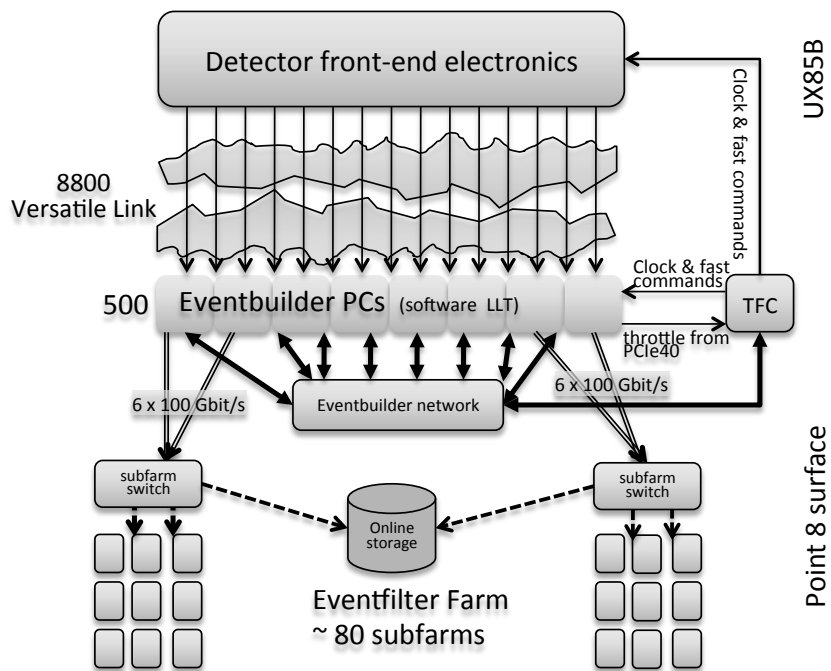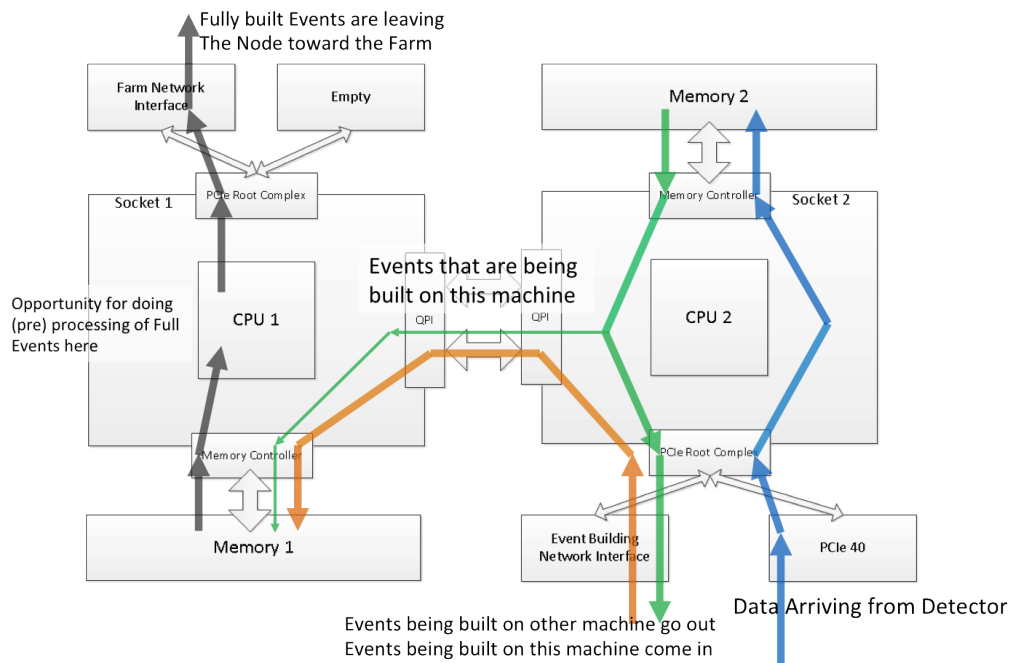, whereas in the trigger information from the UT sub-detector is used to determine the charge and remove low p_T tracks before the Forward tracking. The use of the UT significantly reduces the execution time of the Forward tracking.

reconstruction algorithms similar to those currently used offline, but prioritized to reconstruct the most valuable tracks first, with more specialised track reconstruction algorithms only being used later in the process. Figure 2.25 shows a diagram of the track reconstruction sequence used in the trigger, as well as the main offline reconstruction sequence. Track reconstruction in the trigger begins with execution of the full VELO tracking. Information from the UT sub-detector is then used to extend every VELO track which is consistent with a transverse momentum of at least $0.2\,\text{GeV}/c$. For the subset of tracks which were successfully extended, the charge and momentum is estimated. These tracks are then extended further by searching for hits consistent with $p_T > 0.5\,\text{GeV}/c$ in the SciFi sub-detector. The size of the search regions used to extend tracks in the SciFi are reduced by taking into account the charge and momentum measured in the UT.

Due to the limited storage bandwidth and size, only exclusive channels will be selected and recorded by the trigger system. Track not reconstructed by the HLT software will therefore not be reconstructable later. One notable example is the category of tracks named "downstream tracks", as they will require a significantly longer CPU time to reconstruct that what could be affordable in Run 3 (see Table 2.2). This is due to the lack of a starting seed in the VELO (see Figure 2.25 (right)). They will not therefore be generally available from Run 3 onward.

The work performed in this thesis revolves around a project of making downstream tracks reconstructable and available to the HLT for triggering, even in the harsh conditions of rate and luminosity that LHCb will face in the Future Upgrades runs with a full readout of the detector at 40 MHz.

	time/event (ms)	
	current $\nu = 2$	Upgrade-I, Upgrade-Ib $\nu = 7.6$
T track reconstruction	18	172
matching	8	100
Downstream reconstruction (T track + matching)	~ 26	~ 272

Table 2.2: Execution time of software downstream tracking [7, 55, 56]. The maximum processing time allowed for each event is 13 ms [38]

Chapter 3

The LHCb "downstream tracker"

An innovative tracking device, the so called Downstream Tracker, capable of reconstructing in real-time long-lived particles in the context of the envisioned Future Upgrades (beyond LHC Run 3) of the LHCb experiment, is under development. Motivations, architectural choices, integration in the LHCb-Upgrade DAQ system, and budget constraints will be discussed in this chapter.

3.1   Introduction

The LHCb collaboration has recently published an Expression of Interest [1] and a Physics Document [2] for a future upgrade program beyond the Run 3. This is motivated by the fact that many interesting physics measurements in its current program will still be limited by statistic by the end of the current program (end of Run 3), and, on the other end, continuation of data taking with the Run 3 detector will stop being attractive, on account of the excessive running time needed for a further significant increase of statistical precision. This becomes even less attractive starting from Run 5, when LHC will operate at even higher luminosities, approaching $10^{35} \, \mathrm{cm}^{-2} \, \mathrm{s}^{-1}$ (HL-LHC), thus making the LHCb Upgrade-I detector using only a modest fraction of the available flow of data, that could in principle offer much greater physics possibilities, enabling many important observables to be measured with a precision unattainable at any other experiment [2].

The plan set forth by the LHCb collaboration includes a first "consolidation" phase (Upgrade-Ib) including modest improvements to the current scheme to be commissioned for a Run 4 at the same instantaneous luminosity of Run 3, followed by more extensive upgrades for a higher-luminosity phase ($L \geq 2 \cdot 10^{34} \, \mathrm{cm}^{-2} \, \mathrm{s}^{-1}$) starting in Run 5, with the ultimate goal of collecting $300 \, \mathrm{fb}^{-1}$.

A natural candidate for the consolidation phase is the realization of a specialized device capable of supplementing the Run 3 system with the capability of fully reconstructing all downstream tracks in every event, that would otherwise be lacking for the reasons explained in the previous sections. This is explicitly discussed in the EoI [1] and in the recently released Physics Document on Phase II Upgrade [2] as an attractive addition to the existing system, because not having access to this

information limits efficiency for decay modes with downstream tracks that cannot easily be triggered through another signature. Examples are any channel containing a K_S^0 meson and any channel with less than two prompt charged hadrons, like $B \to K_S^0 K_S^0$, $B \to K_S^0 K_S^0 K_S^0$, $B \to \eta K_S^0$, $B^0 \to \phi K_S^0$, $B \to \omega K_S^0$, $B^0 \to J/\psi K_S^0$, $D^0 \to K_S^0 K_S^0$, $D_s^\pm \to K_S^0 \pi^\pm$, $D^+ \to K_S^0 K^+$, $K_S^0 \to \mu^+ \mu^-$ etc. The same is true for decays involving Λ baryons like $\Lambda_b^0 \to \Lambda \mu^+ \mu^-$, $\Lambda_b^0 \to \Lambda \gamma$, $\Lambda_b^0 \to 3\Lambda$, or long-lived exotic particles (hidden sector WIMP Dark Matter and Majorana neutrinos) . The study of these channels was already planned in the physic program of Upgrade-I and Upgrade-II. The Downstream Tracker can increase the sensitivity for these channel by a factor from 2 to 10. Figure 3.1 shows the invariant mass distributions of $K_S^0 \pi^+ \pi^-$ candidate events in LHCb, data corresponds to an integrated luminosity of $1\,\mathrm{fb}^{-1}$. Yields obtained from the fit are 845 ± 28 downstream decay $B^0 \to K_S^0 \pi^+ \pi^-$, and 360 ± 21 long decay [57].
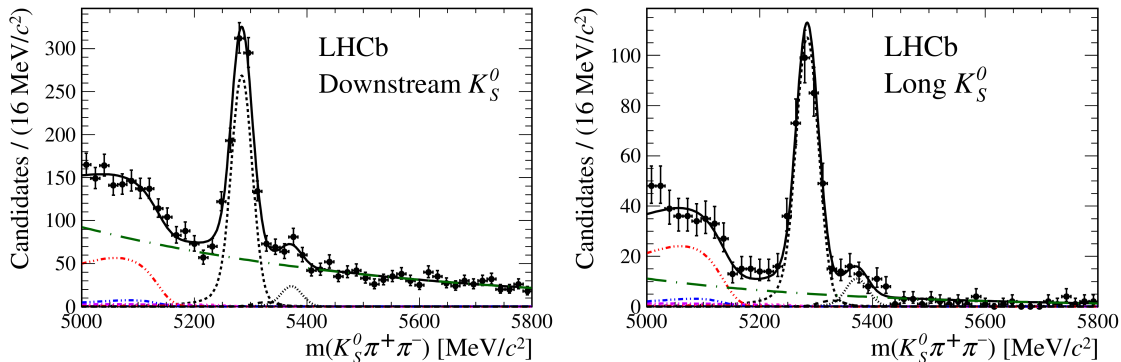
Figure 3.1: Invariant mass distributions of $K_S^0 \pi^+ \pi^-$ candidate events in LHCb [57].

In order to be useful, a Downstream Tracker needs to provides tracks to the software trigger in parallel with all the rest of raw detector information in the event [58]. Also, it needs to do it with a fraction of the huge size, cost and power consumption that would otherwise be needed by an implementation based on conventional CPU technology, and must be able to seamlessly work within the existing Run 3 Data acquisition (DAQ) that has been described in the previous chapter. This is clearly a difficult task, but a worthwhile one, as it is a great opportunity not only to solve a specific well-defined physics need, but also to develop and test new and more advanced technologies of fast data reconstruction, that will be more and more needed in future experiments at high intensities.

3.2   The "Artificial Retina" approach

The "Artificial Retina" architecture was proposed in 2000 [3] as a fast parallel track reconstruction system applicable to HEP experiments inspired by the mechanisms of vision in the natural brain. The mathematical aspects of the algorithm have some

similarities with the "Hough transform" [59,60], a method already applied for finding lines in image processing. However, the crucial feature of the "artificial retina" is the design of a layout and an implementation with the potential of sustaining the event rate at HL-LHC experiments. Thanks to the exploitation of some structural ideas extracted from the current knowledge of the visual system of mammals, that allows them to recognize specific "patterns" in the incoming data with throughput and latency performances vastly superior to what has been achieved in artificial systems to date.

Compared to previous successful real-time tracking systems based on patterns stored in databases (like Associative Memories-based systems) developed for HEP experiments, one of the "Artificial Retina" distinctive element is the way to compare the stored patterns with the incoming detector informations. While other systems provide a binary response ("yes" or "no") from the comparison with stored patterns, the "Artificial Retina" returns a response that continuously varies depending on the "distance" of the track from the patterns imitating the continuous neuron response to exciting stimuli. Interpolating the comparison responses from different patterns allows to obtain higher tracking performances with a reduced number of stored patterns. Another important feature suggested by the structure of natural neural system is a fully data-flow organization with a very high degree of parallelization, with careful avoidance of any sequential steps and wait states. This brings together a further feature known to exist in the natural vision, that is a peculiar organization of the overall system bandwidth: in traditional trigger systems the bandwidth is progressively reduced during processing, while in the "Artificial Retina" the bandwidth increases significantly, because multiple copies of the same data are allowed to be produced, shrinking down only at a later stage as shown in Figure 3.2. This approach has only recently become technically feasible due to the progress of telecommunication technology. A selective data distribution reduces the amount of required bandwidth for single device to a rate feasible in current devices.
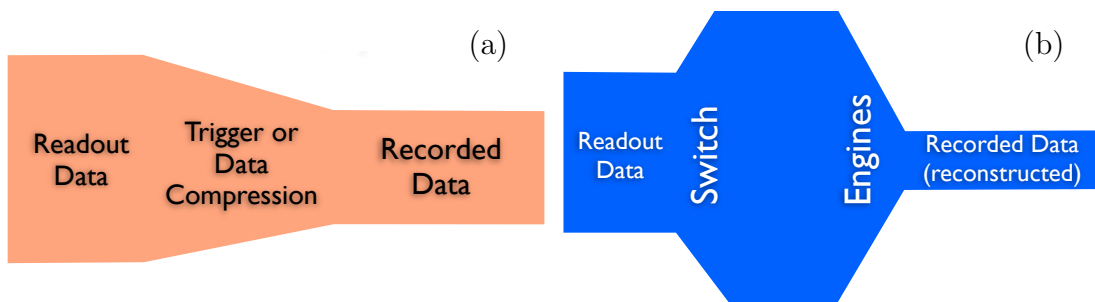

Figure 3.2: Bandwidth flow in a generic trigger system (a) and in the "Artificial Retina" architecture (b).

3.2.1 Basic Concepts

To describe the "Artificial Retina" architecture working principle, we consider the simplified case of straight tracks intersecting a few parallel planar detector layers. Given the coordinates of the hits, we want to estimate the parameters off all the tracks that generated them. If we consider only one transverse view, a track can be described by two parameters only. The tracks parameters are the coordinate of intersection of the track with the first and the last layer of the detector, we call them respectively U and V. We divide the two-dimensional phase space in a grid consisting of cells, and label each cell with a pair of parameters (U_i, V_j). Each cell corresponds to a mapped track. The coordinates of the intersection of a mapped track with the detector layers are $t_l(U_i, V_j)$ where l is the layer number, that we call receptors.

For each event we compute the excitation level defined as:

$$R_{ij} = \sum_{lr} \exp \left(\frac{- \left(x_r^{(l)} - t_l(U_i, V_j) \right)^2}{2\sigma^2} \right)$$

where x_r is the hit on layer l and $t_l(U_i, V_j)$ is the receptor, i.e. the intersection of the mapped track with parameter (U_i, V_j) with the detector layer l. The sum is extended to all hits present in all the layers and computed for all the cell. The parameter σ can be adjusted to optimize the sharpness of the response of the receptor.

Pattern recognition can be reduced to finding cluster in this cell array. Information on the parameters of the tracks can be obtained from the position of each cluster in phase space. Since the response of each receptor is a smooth function of the coordinate of the hits, the excitation level can be used as a weight and the position of the cluster of the center of the cluster can be obtained by interpolation. In this way, the precision on track parameters that can be achieved is typically much better than the pitch of the grid. Plus, the needed computations can be performed in parallel over the array.

Figure 3.3 shows the block diagram of a generic "artificial retina" system. Each cell is implemented as an independent block of logic (engine) that performs autonomously all the necessary operations. Hits flow from the detector into a custom switching network, that delivers each hit to all relevant engines in parallel duplicating them as necessary. Local maxima are found in parallel in all engines, with some limited exchange of information between neighbor engines. The coordinates and excitation level of the local maxima, and the excitation level of their nearest neighbors are outputted sequentially. A final parallel linearized fitter stage extracts track parameters from the cluster informations. The reconstructed tracks are then made available to the trigger/DAQ system. The whole system works as a short asynchronous pipeline accepting an uninterrupted flow of events, that when implemented in modern programmable digital devices endowed with large internal bandwidths, can operate with very high throughputs and low latencies. This opens the possibility of operating the device transparently, so that it effectively appear to the rest of
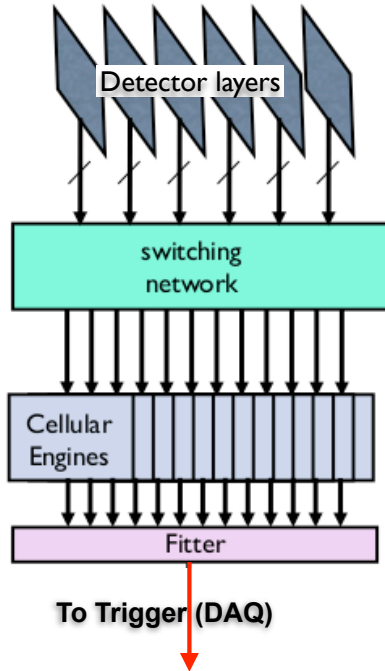
Figure 3.3: Integration of the "Artificial Retina" architecture in the DAQ system of a real experiment.

the DAQ as if tracks are coming out of the detector directly, making it particularly suitable to high-rate, high volume applications.

3.3 The LHCb Downstream Tracker architecture

The Downstream Tracker project must be integrated inside the EB of LHCb Upgrade-Ib. As explained in Section 2.4.4 the EB is a cluster implemented as 500 PC. Gathering data from a such large number of nodes require an equally large number of devices to perform the switching function. Since the switching network only requires a small amount of the logic, using these devices only for this task is a waste of resources. Figure 3.4 shows a modified design conceived for the specific purpose of integrating the Downstream Tracker in the EB. In the new design a large number of individual Tracking Boards are aggregated to form the Downstream Tracker. The Tracking Boards carry out the function of the switching network and the engines together. Every board is connected to a EB node from which it reads the hit. Each portion of the switching network delivers hits to all relevant engines. A mesh network labeled Patch Panel in the figure allows to exchange hits between different Tracking Boards. Each Tracking Board returns a subsample of the reconstructed tracks to the EB node it is connected to. Those tracks are added to the raw data collected by that node, and from this point on the Event Building proceeds normally. As a results, the EFF

49
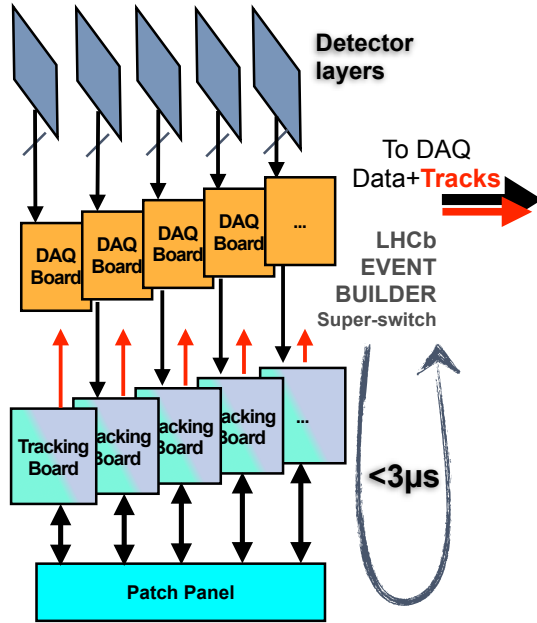
Figure 3.4: Integration in LHCb DAQ.

will receive "raw data" that additionally contain fully reconstructed tracks, that appear as if having been produced by an additional virtual detector. This solution allows to use all the resource of the devices and the full-duplex capabilities of the inter-devices connection.

For not modify the EB specification the latency of the Downstream Tracker must be somewhat smaller than the latency of the EB ($\sim 13\,\mu s$). With the data currently at hand, a sensible objective seems to be a latency $< 3\,\mu s$.

We can implement this design in different ways. One option is to add a PCIe board with a large FPGA in a empty slot of the EB nodes. The Tracking Board could read the data from the PCIe40 through the PCIe bus. The reconstructed tracks can be returned to the EB through the same PCIe bus. This option uses the existing hardware of the EB adding only the Tracking Board and the Patch Panel resulting in a cheap system, but it requires that the EB nodes have a PCIe slot available. Due to the low number of PCIe line in actual CPU this option might turn out to be unfeasible. The DAQ system don't use all the optical links of the PCIe40 board. 24 optical links are used at half speed for data. This board can send data to Downstream Tracker through the 12 free links at full speed. The Downstream Tracker can thus work as a standalone system. It can return the reconstructed tracks to the EB through some dedicated additional EB nodes. This option is a more flexible solution but it requires more hardware to read data through the optical links, plus some modification of the PCIe40 firmware. At the time of this writing, the precise details of the EB implementation that we would need to know to make a definite decision are still subject to change, therefore we will keep both possibilities

open for the time being. They have anyway negligible impact on the rest of the discussion in this thesis. Tab. 3.1 reports the number of Event Builder PC nodes for each LHCb Upgrade sub-detectors, while fig. 3.5 shows the envisioned integration scheme of the Downstream Tracker (or in general of a generic embedded retina-like device) into the LHCb Upgrade Event Builder system.

Sub-detectors	VELO	UT	SciFi	RICH	Calorimeter	Muons
EB node	56	72	156	114	55	30

Table 3.1: Number of Event Builder PC nodes for each LHCb Upgrade sub-detectors.
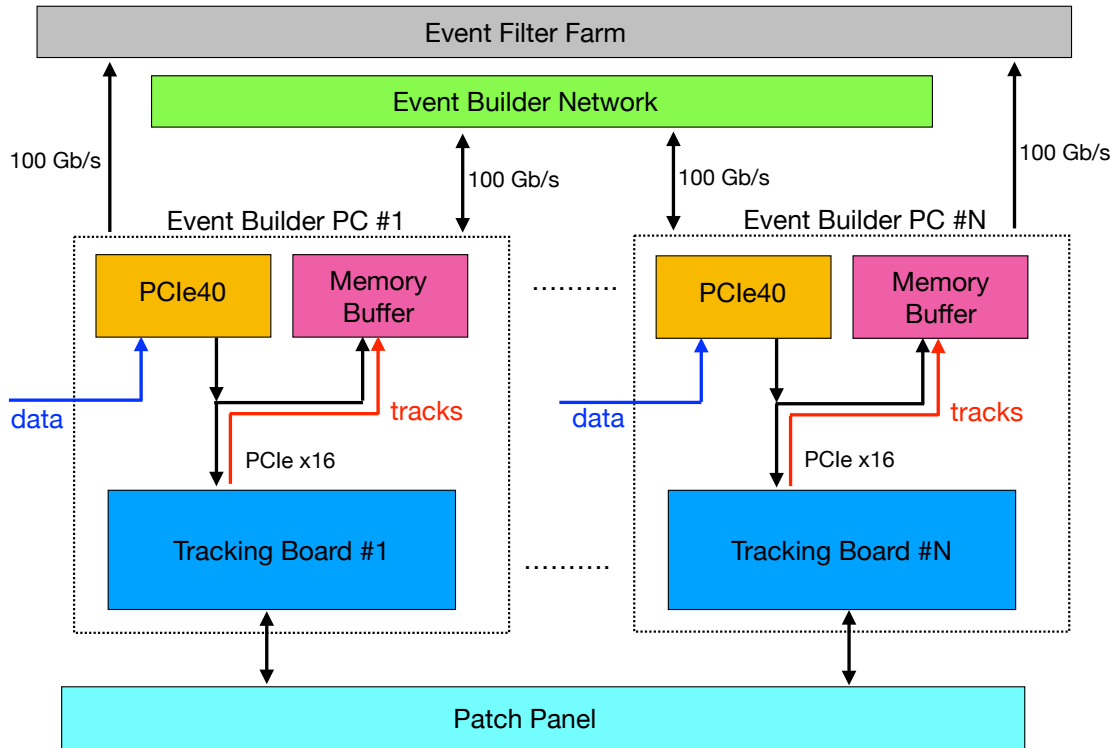

Figure 3.5: Integration scheme of the Downstream Tracker into the LHCb Upgrade Event Builder system.

3.4 Implementation details

The architecture described in previous sections is flexible and largely scalable. Without significant loss of generality, we will in the following make reference to straight

tracks intersecting a few parallel detector layers. The tracks parameters that we use are the coordinate of intersection of the track with the first and the last layer of the detector, we call them respectively U and V.

3.4.1 Mapping algorithm

For configuring the "Artificial Retina", the phase space of track parameters is divided into cells, which mimic the neurons connected to the receptive fields of the retina. The center of each cell corresponds to a specific track in the detector that intersects the layers in spatial points called receptors. A C++ piece of software code (Detector-Mapping) calculates the receptors for each cell, as shown in Figure 3.6. Not all hits are significant for each cell. A second step of the Detector-Mapping, also shown in Figure 3.6, groups contiguous cells. For a group of contiguous cells, where variations of track parameters are small, the corresponding receptors in the detector layers would belong to a limited area. The Detector-Mapping calculates which groups of cells are influenced by the hits recorded in a detector area. A hit influences a cell if its distance from the receptor is lower than the distance search. The distance search is a parameter of the "Artificial Retina", a typical value of the distance search is the pitch of cells grid.

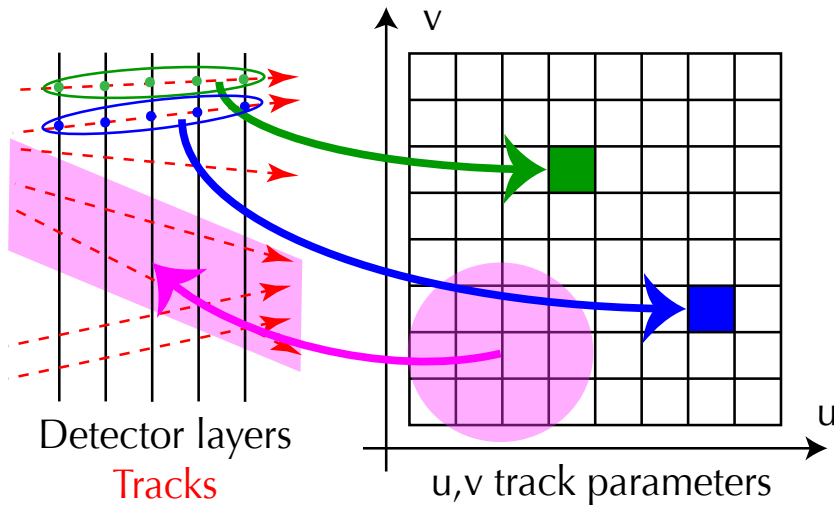Figure 3.6: "Artificial Retina" mappings for tracks on a plane without magnetic field, where tracks can be described by two parameters U and V. Magenta cloud shows a group of cell influenced by a specific detector area.

3.4.2 The switching network

To realize the "Artificial Retina" in practice, a crucial ingredient is a system for distributing in real-time the hit informations coming from the detector layers to the
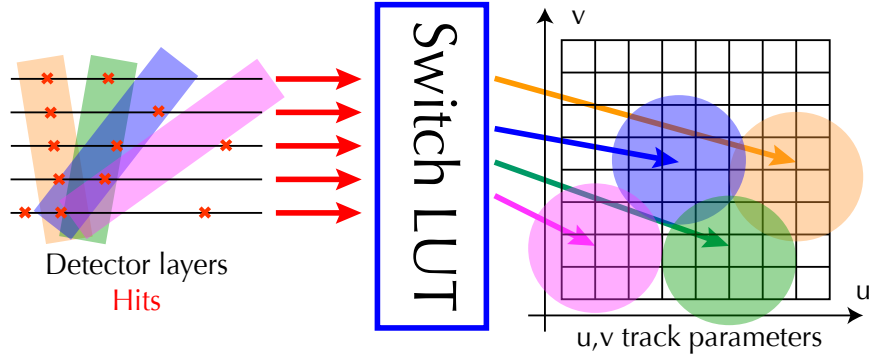
Figure 3.7: The switching network send hits to the influenced cell groups. Clouds shows cell group influenced by different detector areas.

array of cell. Given the high bandwidth of several Tbits/s, this is a nontrivial task. The switching network is a intelligent delivery system, with embedded information allowing each hit to be delivered in parallel to all cell. The switching network use the information calculated in the mapping step to deliver each hit only to the influenced cell groups. The switching network can send the same hit to more cell groups, as shown in Figure 3.7. As shows in Figure 3.2, the network increase the global bandwidth making multiple copies of hits ($10 - 12$ copies), but it never sends a hit to all the engines, reducing the input bandwidth for them.

3.4.3 The processing engine

The engine is the hits processor of a cell. Figure 3.8 shows the engine functions. For each hit x_l on layer l the engine calculates the Euclidean distance $d_l(x_l, t_l)$ from the cell receptor t_l of that layer. Then calculates the weight w of each hit. The weight is defines as:

$$h(x_i) = \begin{cases} 0 & \text{if } |(x_l - t_l)| > d_s \\ \exp\left(\frac{-(x_l - t_l)^2}{2\sigma^2}\right) & \text{if } |(x_l - t_l)| < d_s \end{cases}$$

where d_s, the distance search, is a cutoff of the weight function, and σ controls the width of the weight function. d_s and σ are parameters of the "Artificial Retina" architecture, that can be adjusted to optimize the sharpness of the response of the receptors, and to reduce the input bandwidth for the cells. Typical value of d_s is the pitch of cells grid, and typical value of tσ is half pitch of cells grid. The engines can process a hit for each clock cycle, and all the engines work in a fully parallel way. The engine excitation level is the summation of the weight of each hit. When all the hits of a same event are processed, the engines begin to identify the tracks.
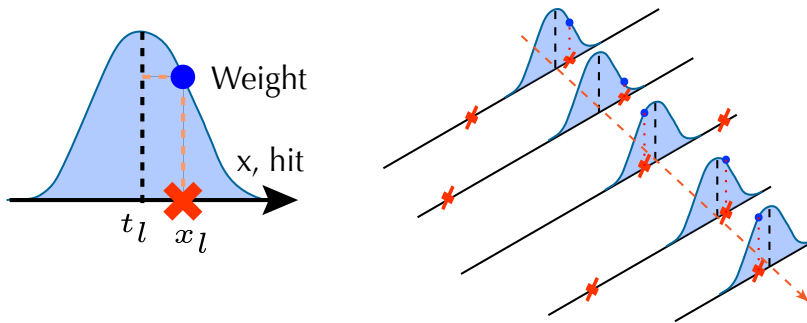
Figure 3.8: Engine calculates the weighted distance of the hits from its receptors.

3.4.4 Clustering

Tracks can be identified by looking for local maxima of the excitation level over the cells grid, shown in Figure 3.9. The engines read the excitation level of the neighbor engines inside a square 3×3. If the excitation level of the neighbor engines is lower than the engine excitation level, the engine is flagged as local maximum. We can set a threshold level for avoid false positive maxima. For a track resolution similar to offline reconstruction the grid does not require a high granularity, because significantly better precision can be obtained by computing the centroid of the 3×3 excitation level cluster. Given the excitation level R_{kl} of the engines, the track parameters $\overline{u}$ and $\overline{v}$ can be calculated as:

$$\overline{u} = u_0 + \delta u \frac{\sum_{kl} k R_{kl}}{\sum_{kl} R_{kl}}$$

$$\overline{v} = v_0 + \delta v \frac{\sum_{kl} l R_{kl}}{\sum_{kl} R_{kl}}$$

with $k = i-1, i, i+1$ and $l = j-1, j, j+1$, where u_0 and v_0 are the track parameters of the cells grid origin , δu and δv are the pitch of the cells grid, i and j are the index of the local maximum engine.

3.5 Hardware prototype and budget constraints

Given that the novelty of the artificial retina algorithm, the LHCb-Pisa group designed and implemented small hardware prototypes [6,61] of the system in order to demonstrate that very high throughputs, at luminosity of 2×10^{33} cm^{-2}s^{-1} (LHC Run 3 and Run 4 conditions), can be achieved in a FPGA based system. A first prototype using faster devices has been built using a board by DiniGroup, the DNS5GX_F2[1], equipped with two large Altera Stratix V FPGAs (almost 1M logic

---

[1]`https://www.dinigroup.com/web/DNS5GX_F2.php`
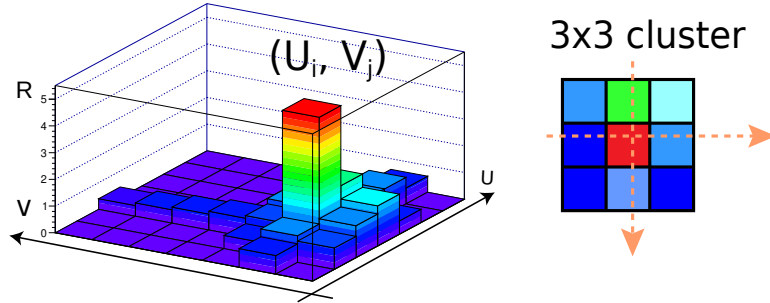
Figure 3.9: Cells excitation levels with a single maximum, and the 3×3 cluster around the maximum.

elements each), and with a large number of LVDS and optical interconnections. The algorithm was configured to reconstruct tracks in a tracker made by 6 single-coordinate layers and no magnetic field. The phase space of two-dimensional tracks was parameterized using the coordinates on the first and last layer, and it was divided in cells [2]. Each of them has been implemented as a distinct processing unit (engine), that accumulates weights proportional to the hit distance from the pattern track. Tracks are reconstructed looking for cells that are local maxima in the parameters phase space. Events with different occupancy, corresponding to few percent occupancy measured as number of tracks per cells, are used. An event rate of approximately 40 MHz down to 10 MHz, as shown in Fig. 3.10, and a latency smaller than 500 ns, were measured, perfectly in agreement with the requirements of DAQ systems planned for HL-LHC.

After demonstrating that high-speed performances can be achieved, the system has been specialized to the LHCb Upgrade experiment in order to evaluate realistic performances and cost feasibility. The configuration described above has been adapted to the SciFi tracking stations after the magnet. Due to the number of cells fitting in a single FPGA and the maximum number of slots available for PCIe boards in the EB ($\approx$ 78 EB nodes for the $x-z$ view, see tab. 3.1), the track parameters space for each quadrant[3] has been covered with approximately 20k cells (for a total of 80k cells for the whole axial view of the SciFi sub-detector). Using this configuration the system processed events with 200 tracks simulated with a simplified geometry (toy), and minimum-bias events fully simulated using the official LHCb simulation [62] with the current geometry for LHCb Upgrade. It turned out that 95% of the generated tracks are corresponding to local maxima, while 48% of found maxima are false

---

[2] Each cell corresponds to a pattern

[3] Quadrant can be considered independent for track reconstruction purpose.
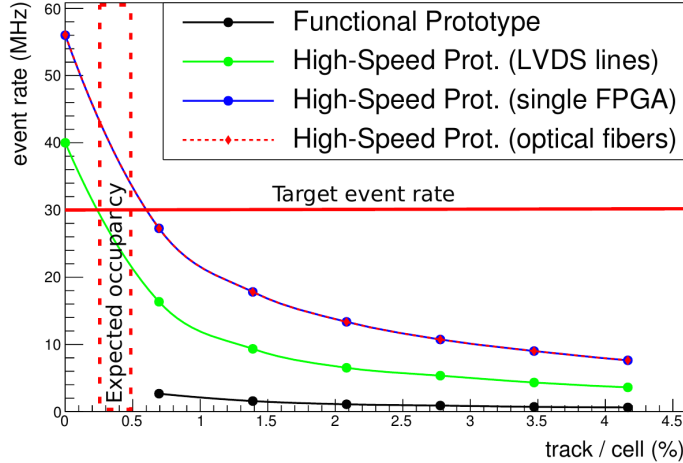
Figure 3.10: Event rate vs occupancy for different configurations. The figure is extracted from Ref. [61], where all curves are explained in detail, along with the different system configurations. As far as this thesis, the red dashed line, referred as "High-Speed Prot. (optical fibers)", is the most optimized prototype where FPGAs chips on the board communicate trough optical fibres at full speed. The "Expected occupancy" vertical band refers to the SciFi occupancy ($x - z$ axial view corresponding to 6 single-coordinate layers), where a throughput above the value of 30 MHZ is achieved.

positives (called ghosts). With this configuration it has been possible to estimate for the first time the amount of logic needed to implement a realistic system, completed of main components (Switching Network, Processing Engines, and Clustering). The Stratix V GX chip (model 5SGXAB)[4] was full at 93% level, and it was able to host about 960 engines. This translates into the budget constraint of approximately 1000 LEs per engine (or elementary pattern cell), since the maximum number of chips (at the moment we assume to have one chip per tracking board) is fixed by the PC EB nodes receiving raw hits from the SciFi sub-detector. Since, already nowdays, FPGA chips with larger number of Logic Elements (up to 2M LEs) are available, it is reasonable to assume that the a realistic system retina-like, to be installed during the LS3 (2024-2027) will have a size of about 10^5 elementary pattern cells (or engines) to be implemented in a reasonable number of approximately 100 high-end FPGAs.

3.6 This thesis

The LHCb-Pisa group demonstrated that the artificial retina algorithm is a feasible approach for a tracking device at low-level in a typical HL-LHC environment, developing hardware prototypes of the system, implemented on modern FPGAs in a fully pipelined way. An event rate of about tenths of MHz, very close to the 30

---

[4]The Altera/Intel Stratix V GX chip (model 5SGXAB) has 952 kLEs, 352 Variable-precision DSP blocks, and 48 transceivers at 14.1 Gbps each, and 210 LVDS channels at 1.4 Gbps (receive/transmit).

MHz requirement, and latency less than 1 μs, much shorter than the time available before the event is built, were achieved. Then, the LHCb-Pisa group started the development of a processor for reconstructing tracks originating outside the vertex detector at the LHCb Upgrade, in order to determine tracking performances of the envisioned device, and compare them with the offline software reconstruction when processing events fully simulated at the LHCb Upgrade conditions. Very preliminary studies demonstrated that high reconstruction efficiencies, close to 90% level, can be achieved in the reconstruction of 2D tracks, with about 80k pattern cells, where each of them needs about 1000 LEs to be implemented on modern FPGA chips. The price to pay is a very high ghost rate of tracks of about 48%[5], when tracks in the SciFi sub-detector are reconstructed using only the 6-axial layers. This was the state-of-art at the beginning of the work of this thesis.

The aim of this thesis project is to assess the tracking performance, that such an approach could achieve to the Future Upgrades of the LHCb experiment, for the realization of the Downstream Tracker project, within known budget constraints described in the previous section: an affordable size of such an envisioned device has to be of about 10^5 pattern cells, where each of them corresponds to about 1000 Logic Elements (LEs). A high-level simulation of the envisioned device, written in C++ programming language, has been therefore developed in order to determine the achievable tracking performances, given both the above constraints on the size of the system and on the compliance with the future LHCb data acquisition system. The main task of thesis is the precise determination of the tracking parameters in reconstructing LHCb-Upgrade downstream tracks, such as the reconstruction efficiency and the probability of reconstructing fake tracks ('ghosts') as a function of track parameters, along the resolution in measuring three-dimensional momentum and space trajectory. An exhaustive comparison between simulated tracks, reconstructed by the envisioned device, and tracks reconstructed with LHCb-Upgrade offline tracking program, running in the high level trigger sequence, has been carried out in order to assess tracking performance in absolute terms.

In particular, the thesis project has faced for the first time the challenge of reconstructing the T-tracks, using both axial and stereo layers of the SciFi sub-detector aiming at a full three-dimensional reconstruction. Finding T-tracks is the first, and the most CPU-time consuming, stage of the reconstruction of downstream tracks. From a theoretical point of view the artificial retina algorithm is well suited to solve tracking problem with any dimensionality. However, its application to the real life is not so straightforward because of the limited amount of local connectivity amongst engines into the current (and future) available electronic devices. The retina algorithm would require connections between cells in a dimensional space having the dimensionality of the space of track parameters[6]. However, the current available

---

[5]Reconstruction efficiency is defined as the ratio of the number of truth-matched reconstructed tracks to the number of reconstructible tracks in the SciFi acceptance. The ghost rate, instead, is defined as the ratio of the difference between the number of reconstructed tracks and the number of truth-matched reconstructed track to the number of the reconstructed tracks.

[6]In our case, straight lines on the 3D space are identified by 4 free parameters, if no magnetic

integrated circuits allow only connections on a two-dimensional plane and it entails a large amount of logic elements just to correctly connect the whole cells. In order to overcome this problem, I propose a different approach, factorizing the problem into two two-dimensional ones. The result of the first tracking stage will work as starting seed for solving the second stage that would lead us to the final solution. The addition of sequentiality into the algorithm obviously introduces a larger latency to the system, that must be accurately determined with a full hardware implementation of the 3D algorithm (which is clearly out of the scope of this thesis). However, the second stage, as described in Chapter 6, is logically similar to the first one, therefore the increase of the latency should have a negligible impact, being the latency of the Event Builder (about 13 μs) much larger than the measured latency of the first stage, namely the reconstruction of axial tracks, which turned out to be less than 500 ns.

A short summary of the contents of next chapters of the thesis follows. Chapter 4 describes the official LHCb detector simulation and the simulated samples used to develop the high level simulation of the Downstream Tracker, along with the definition of the track model used to solve pattern recognition and finding track parameters in the SciFi sub-detector. Chapter 5 describes the first step of the tracking sequence, where axial tracks are found, while the extension to the stereo layers of the SciFi is explained in detail in chapter 6. Lastly, an exhaustive comparison between performances of the Downstream Tracker with those obtained with the LHCb-Upgrade offline tracking program, running in the high level trigger sequence, is shown in chapter 7. Final conclusions are shown in chapter 7.

---

field is assumed in the SciFi subdetector. If the small fringe field, present in the SciFi sub-detector (see section 4.6) is considered, tracks are identified by 5 free parameter.

Chapter 4

The Official LHCb Upgrade detector simulation and track model

This chapter describes the Official LHCb Upgrade detector simulation, with a particular attention to the simulation of the Scintillating Fibre Tracker of the LHCb Upgrade, which is the subdetector used in this thesis to develop the Downstream Tracker. The track model used is also explained in detail.

4.1   The LHCb Simulation

In LHCb the task of modeling the behavior of the spectrometer for the different type of events occurring in the experiment is carried out by two separate applications called GAUSS and BOOLE [63]. GAUSS generates the initial particles and simulates their transport through the LHCb detector, whilst BOOLE reproduces the different subdetectors responses and their digitization converting the data in the same format provided by the experiment electronics and the DAQ system. After digitization real data and Monte Carlo data follow the same path through trigger, reconstruction and analysis procedures. GAUSS is customized by choosing and configuring the appropriate set of algorithms to execute in a given sequence and other suitable components for the various tasks. Some of these components, as the generator and the GEANT4 toolkit [64, 65]. In LHCb the production of particles coming out of the primary pp collision of the LHC beams is handled by default with PYTHIA [66], a general purpose event generator, whilst the decay and time evolution of the produced particles is delegated to EVTGEN [67]. This package, originally designed for the BaBar collaboration, is specialized to accurately describe B decays with a special customization for LHCb needed to handle incoherent B^0 and B_s^0 production in contrast to the coherent production at the B-factories. Lastly, in GAUSS the simulation of the physics processes undergone by the particles travelling through the detector, is delegated to the GEANT4 toolkit.

The Official LHCb Upgrade detector simulation is the most important tool to study tracking performance of the envisioned Downstream Tracker. Since the thesis subject is the reconstruction of T-tracks, a detailed description of simulation of the SciFi subdetector follows. Anyway, a general and more detailed description of the whole framework can be found in Ref. [62].

4.2   Simulated data samples

In order to develop the retina algorithm for the Downstream Tracker and measure tracking performances three different simulated samples are considered. They differs one from another by the event topology. All of them are produced at the LHCb Upgrade-I conditions (LHC Run 3 and Run 4), as follows:

- $\sqrt{s} = 14\,\text{TeV}$;

- LHC bunch spacing = 25 ns;

- $\mathcal{L} = 2 \times 10^{33}\,\text{cm}^{-2}\,\text{s}^{-1}$;

- $\nu = 7.6^1$.

The first one (*Sample 1*) is a sample of generic inelastic events, the so-called Minimum Bias sample, while the others two are filtered samples containing an hard collisions in each event, which has produced a $D^{*+} \to D^0 \pi^+ \to [K_S^0 \pi^+ \pi^-] \pi^+$ decay (*Sample 2*) and a $B_s^0 \to \phi\phi \to [K^+ K^-][K^+ K^-]$ decay (*Sample 3*). A summary of the three samples is reported in tab. 4.1.

Sample	Nb. Events	Decay Mode
Sample 1	1,000	Minimum-Bias
Sample 2	1,000	$D^{*+} \to D^0 \pi^+ \to [K_S^0 \pi^+ \pi^-] \pi^+$
Sample 3	1,000	$B_s^0 \to \phi\phi \to [K^+ K^-][K^+ K^-]$

Table 4.1: Simulated data samples.

4.3   The Scintillating Fibre Tracker simulation

The simulation through the LHCb Scintillating Fibre Tracker of the generated samples consists of three different steps:

---

[1] ν is the mean number of primary vertices per bunch crossing.

1. All interactions with the SciFi subdetector of all generated particles in the event from are simulated. Each simulated particle, therefore, generates a list of energy deposits in the various sub-detectors according to the detector acceptance.

2. The read-out electronic chain is simulated, producing the clusters out of the energy deposits in the detector. A cluster contains the information in a binary format of the position of the read-out channel corresponding to a "converted" energy deposit. Clusters can also be produced by spill-over and noise. Additional inefficiencies are simulated, taking into account the missing coupling of the read-out with the fibers and including the light attenuation due to ageing after 50 fb^{-1} of data taking.

3. The binary format is decoded into hits, which become available for tracks reconstruction.

The process of transforming the hits generated by the GEANT4 simulation into a digital signals is called digitization and it is implemented using the BOOLE software. as already mentioned. It accounts for the attenuation of the fibres after irradiation, the geometry of the fibres with respect to the SiPM channels, the gain of the SiPMs, the thermal noise, the noise from afterpulses and spillover, and the clustering. The final output is given in the same data format as the one that is expected from the final detector. All the details of how the samples are digitized can be found in Ref. [68].

4.4   Detector occupancy and hit efficiency

The main aspects of the detector simulation, and so of the detector itself, that have an impact on the tracking algorithm design and its performance are:

- the **detector occupancy** $(\frac{n_{\text{hits}}}{n_{\text{channels}}})^2$, mainly dependent on the event track multiplicity, on the number of primary vertices and on the contribution from spillover and detector noise to the formation of the clusters;

- the **hit conversion probability**, *i.e.* the probability that an energy deposit in the active material is converted into a hit for pattern recognition;

- the **acceptance of the detector**, depending on the detector geometry.

The SciFi detector occupancy for the generated samples is on average 4.5 clusters per *SiPM* per event in the hottest detector region. This means that one would expect to find on average in the hottest part of the detector one cluster every 7 mm, assuming the clusters to be uncorrelated (*i.e.* not generated from the same hit). The average

---

[2] n_{channels} is the number of channels available for the read-out.

number of hits per layer in the SciFi for a typical event is around 300 - 400 at the upgrade conditions (Fig. 4.1).[3]
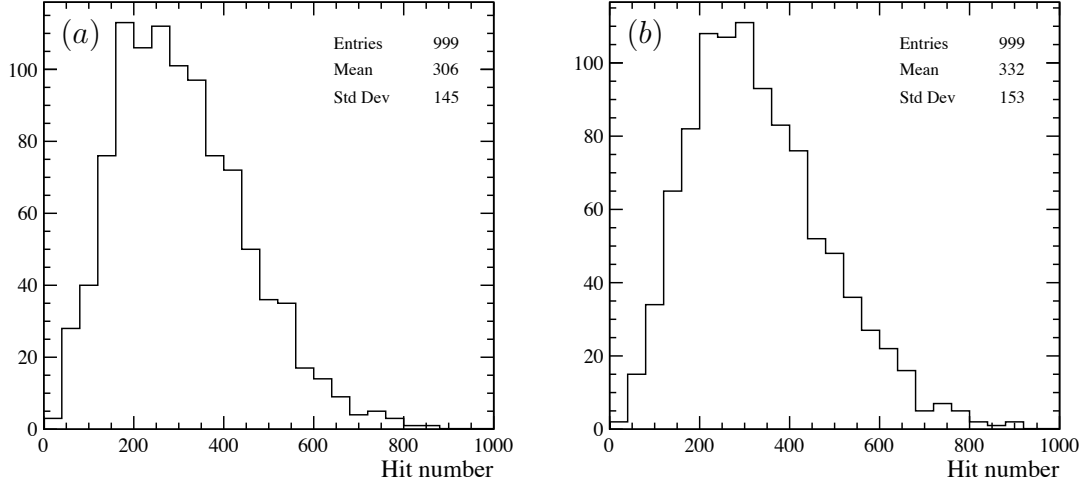
Figure 4.1: Distribution of the number of hits for the first axial layer (n. $0x$) and the last stereo layer (n. $10v$) of the SciFi subdetector.

Defining the effective hit efficiency as ε_{hit}, arising from the convolution of acceptance and digitization, it is possible to calculate the theoretical upper limit on *tracking efficiencies* when a minimal requirement on the number of hits on track is applied, by using the following binomial probability:

$$Prob(n_{track}^{layers}|12) = \binom{12}{n_{track}^{layers}} \cdot (1 - \varepsilon_{\text{hit}})^{12-n_{track}^{layers}} \cdot (\varepsilon_{\text{hit}})^{n_{track}^{layers}}$$

where n_{track}^{layers} is the number of fired layers that don't miss the hit. The value of ε_{hit}, determined by the simulation, at the LHCb Upgrade conditions, is $\varepsilon_{\text{hit}} = 97.5\%$. It is therefore possible to determine the above probability, in order to calculate the upper limit on the reconstruction efficiency using only axial (or stereo) layers

$$Prob(n_{track}^{layers}|6) = \binom{6}{n_{track}^{layers}} \cdot (1 - \varepsilon_{\text{hit}})^{6-n_{track}^{layers}} \cdot (\varepsilon_{\text{hit}})^{n_{track}^{layers}}$$

that with $n_{track}^{layers} = 6$ gives

$$Prob(n_{track}^{layers} = 6|6) = 85.9\%.$$

---

[3]Both the occupancy (and track multiplicity) in the detector and the amount of hits in the whole SciFi are directly correlated to the amount of primary vertices per event, the noise of the read-out and the spill-over.

The loss of reconstruction efficiency is certainly larger than the 14% level, when a requirement of having 6 reconstructed axial hits (one for each layer) is asked. It is therefore useful to calculate the same probability, by requiring 5 reconstructed hits out of 6, namely $n_{track}^{layers} \geq 5$, that gives:

$$Prob(n_{track}^{layers} \geq 5|6) = 99.1\%.$$

The loss of efficiency is now affordable, being less than 1% level. This is very important parameter for the designing of the Downstream Tracker, where it is not possible to add in the tracking algorithm any sequential step of recovering tracks with different number of reconstructed hits.

Lastly, the radiation damages corresponding to $50\,\mathrm{fb}^{-1}$ are simulated for all the samples. The impact of the radiation damages are stronger in the central region leading to higher *hit conversion probability* inefficiencies. Therefore, due to the radiation damages and the light attenuation in the fibers, it will be more likely to have tracks with a lower number of hits in the central region of the detector rather than in the external one.

4.5   Event topology

In order to design and optimize a real-time tracking algorithm, as the artificial retina applied to the Downstream Tracker, is important to analyze the topology and the features of the LHCb Upgrade event. In the following, the *Sample 1*, i.e. the sample containing the Minimum Bias events, is examined. No relevant differences between the three available samples are observed for these qualitative studies. Fig. 4.2 shows the number of primary vertices and the number of track contained in each event. The distribution of primary vertices has a mean value of 7 and a standard deviation of 2.3, while the mean value of the number of reconstructible tracks in each event is about 140 track/event. A non negligible tail of the distribution of the number of tracks per event is also clearly visible, reaching values up to 400 tracks per event. This feature is of high interest in the development of the real-time tracker, under study in this thesis, since tracking performances strongly depend on the level of occupancy of the detector. Instead, fig. 4.3 and fig. 4.4 show the distributions of the three-dimensional momentum of the tracks (p) and of the momentum transverse (i.e. perpendicular) to the beam line of the (p_T). The p_T momentum component is calculated at the entrance of the SciFi subdetector. In both distributions is clearly visible a peak at very low momentum values. These are tracks, that can be reconstructed in the SciFi subdetector[4], but cannot be reconstructed as Long or Downstream tracks, as shown in fig. 4.5. They are likely particles generating from the interactions between the halo beam and the beam pipe, or from other processes not directly related to the *pp* interactions.

---

[4]These tracks are also called *reconstructible* tracks in the SciFi, and the precise definition will be given in the chapter 5.
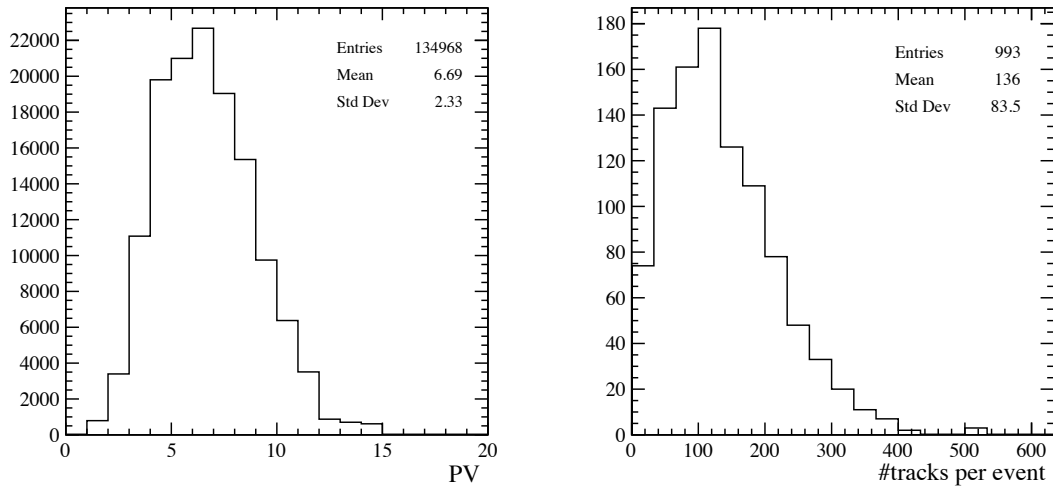
Figure 4.2: Distribution of the number of primary vertices (left). Distribution of the number of tracks per event (right).
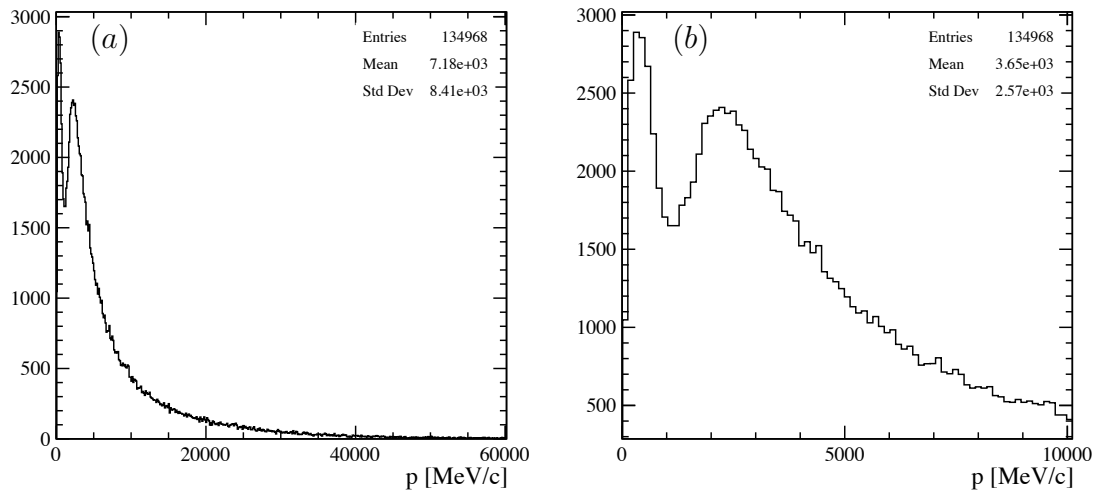
Figure 4.3: Distribution of the three-dimensional momentum of the tracks (a). Zoom at lower momentum values is shown (b).

64
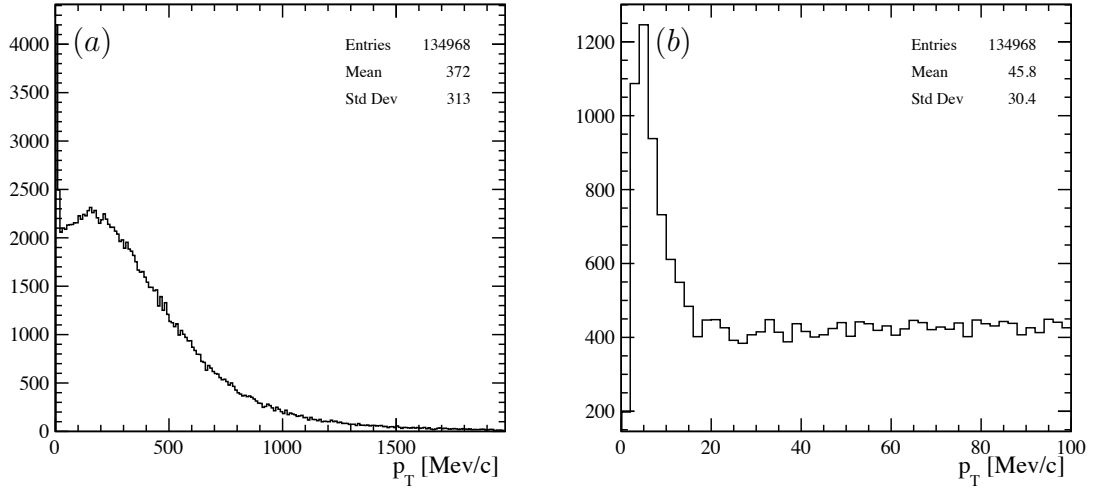
Figure 4.4: Distribution of the transverse momentum p_T of the tracks (a). Zoom at lower transverse momentum values is shown (b).
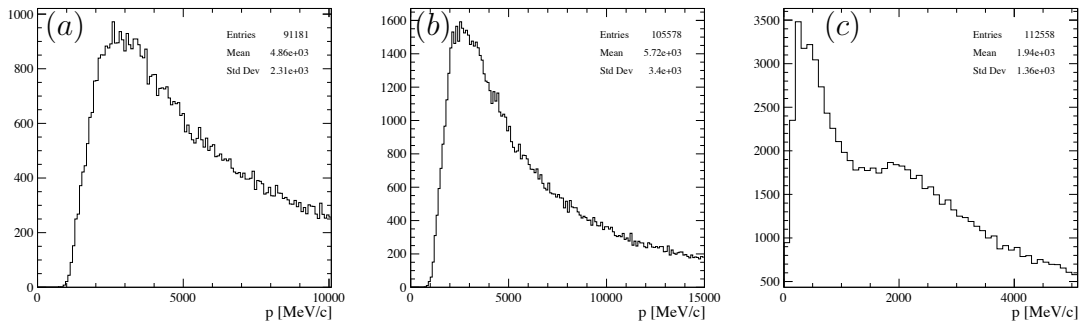
Figure 4.5: Distribution of the track three-dimensional momentum p for Long tracks (a), Downstream tracks (b), and for reconstructible tracks in the SciFi that are neither Downstream nor Long tracks. Similar distributions are obtained for the transverse momentum p_T.
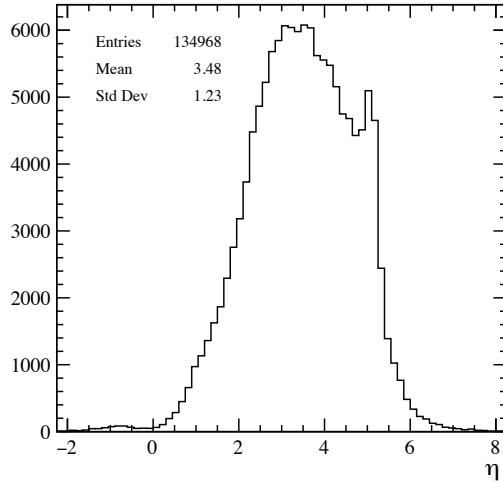
Figure 4.6: Distribution of the track pseudorapidity η.
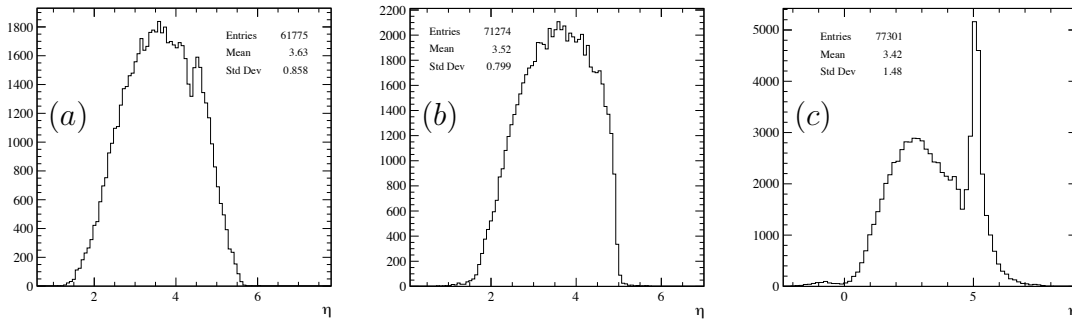
Figure 4.7: Distribution of the track pseudorapidity η for Long tracks (a), Downstream tracks (b), and for reconstructible tracks in the SciFi that are neither Downstream nor Long tracks. Similar distributions of the p are obtained.

Fig. 4.6 shows the distribution of the pseudorapidity η, defined as:

$$\eta = -\ln\left[\tan\left(\frac{\theta}{2}\right)\right],$$

where θ is the angle between the direction of the particle and the beam axis. Particles with very high values of pseudorapidity are generally lost, escaping through the beam pipe. Particles with values of pseudorapidity close to zero have a dominant p_T component. Negative values, instead correspond to particles going backwards to the LHCb direction. A peak at higher values of pseudorapidity, around $\eta \approx 5$, is clearly visible. As for the momentum distributions, this is due to the presence of very low momentum reconstructible tracks within the SciFi subdetector, that are neither long nor downstream tracks, as shown in fig. 4.7

66

As it can be expected from the η distribution, reconstructible tracks are concentrated in a limited region of the detector. Fig. 4.8 shows the track intersection with the first and last layer of the SciFi subdetector. The density of reconstructible track is clearly higher in the region close to beam pipe, while it decreases in the regions far away to that. The occupancy of the SciFi depends on the track intersection point and this fact impacts the designing of the Downstream Tracker, as it will be shown in chapter 5.
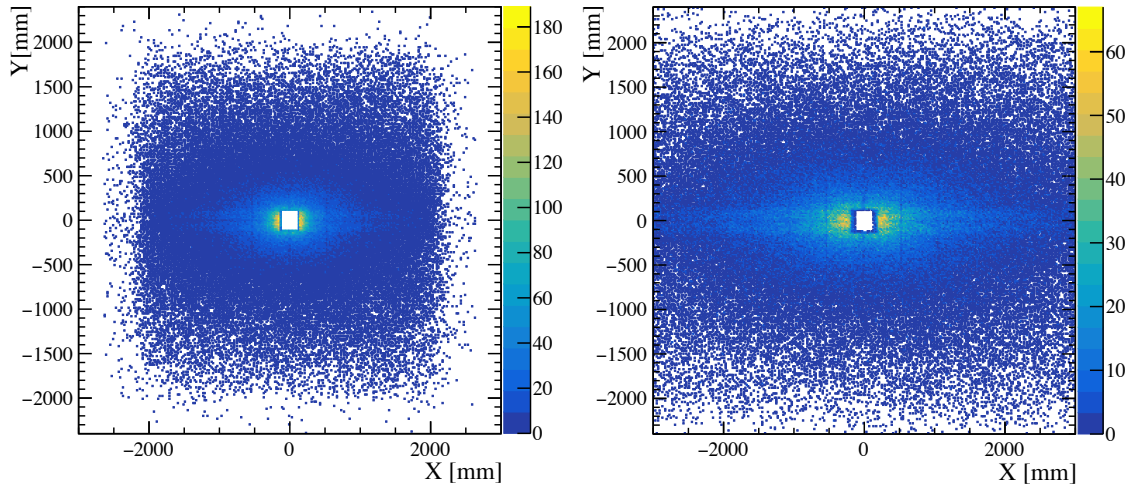
Figure 4.8: Distribution of the track intersection with the first layer (on the left side) and the last layer (on the right side) of the SciFi subdetector. The highest tracks density occurs near the beam pipe. The different scales between the two figures are due to the tracks enlargement.

Fig. 4.9 and fig. 4.10, instead, show the distribution of hits on different axial and stereo layers. Another interesting information about the SciFi occupancy, which is also an important ingredient for the designing and the development of the tracking algorithm for the Downstream Tracker, is the average number of hits per event, on each SciFi layers. Each layer has an average number of hit of about 300 per event, as shown in fig. 4.1.
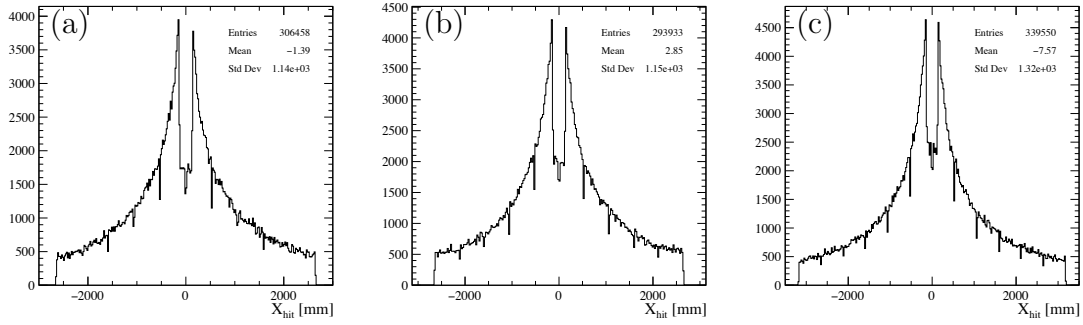
Figure 4.9: Distribution of the hit x coordinate for different axial layers. Layer number $0x$ (a), layer number $4x$ (b), and layer $11x$ (c).
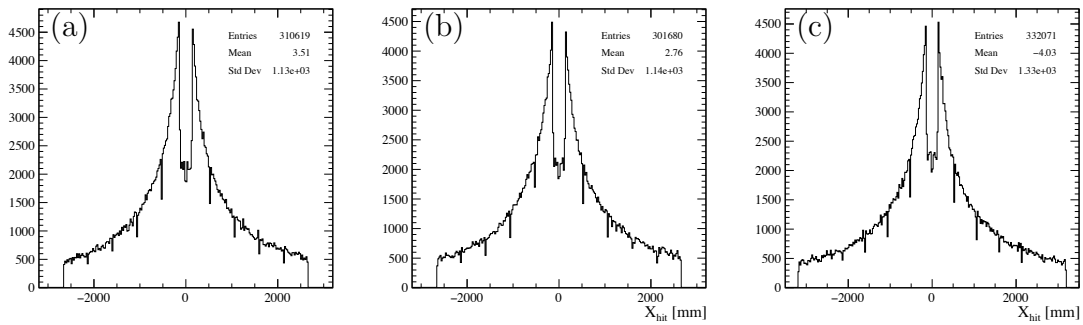
Figure 4.10: Distribution of the hit x coordinate for different stereo layers. Layer number $1u$ (a), layer number $5u$ (b), and layer $10v$ (c).

4.6   Track model in the SciFi tracker region

The analytical parameterization of a track is a crucial ingredient for any pattern recognition algorithm, since it has a direct impact on its performance. The model described in this section is the one adopted to study the three dimensional retina based track reconstruction algorithm using only information from the SciFi. The model takes into account the detector configuration. The track model has a significant impact on the track fit procedure as well as in track parameter estimation.

The equation of motion of a charged particle of momentum $\vec{p}$, charge q and velocity $\vec{v}$ in a magnetic $\vec{B} = (B_x, B_y, B_z)$ field is:

$$\frac{\mathrm{d}\vec{p}}{\mathrm{d}t} = q\vec{v} \times \vec{B}$$

leading to the following equations for the different momentum components p_x, p_y, p_z (where $p = \sqrt{p_x^2 + p_y^2 + p_z^2}$):

$$\frac{\mathrm{d}p_x}{\mathrm{d}z} = q(t_y B_z - B_y) \quad ; \quad \frac{\mathrm{d}p_y}{\mathrm{d}z} = q(B_x - t_x B_z) \quad ; \quad \frac{\mathrm{d}p_z}{\mathrm{d}z} = q(t_x B_y - t_y B_x), \quad (4.1)$$

where $t_x = p_x/p_z = \mathrm{d}x/\mathrm{d}z$ and $t_y = p_y/p_z = \mathrm{d}y/\mathrm{d}z$ are the track slopes. The differential equations for the track slope in the x-z plane is:

$$\frac{\mathrm{d}t_x}{\mathrm{d}z} = \frac{q}{p}\sqrt{1 + t_x^2 + t_y^2}\left(t_x t_y B_x - (1 + t_x^2)B_y + t_y B_z\right), \quad (4.2)$$

and for the y-z plane:

$$\frac{\mathrm{d}t_y}{\mathrm{d}z} = \frac{q}{p}\sqrt{1 + t_x^2 + t_y^2}\left((1 + t_y^2)B_x - t_x t_y B_y - t_x B_z\right). \quad (4.3)$$

Within the volume covered by the three SciFi stations T1, T2, T3, it is possible to define a track model accounting for the local magnetic field $\vec{B}$, in the approximation of small $|t_x|$ and $|t_y|$, as the particle are highly boosted along the z axis. In addition, most of the tracks are in the central region, where the dominant component of the field is B_y ($B_x/B_y \ll 1$ and $B_z/B_y \ll 1$). So, keeping only the first order terms, the equations of the trajectory eq.4.2 and eq.4.3 can be simplified as:

$$\frac{\mathrm{d}^2 x}{\mathrm{d}z^2} = \frac{\mathrm{d}t_x}{\mathrm{d}z} \simeq -\frac{q}{p}B_y \quad ; \quad \frac{\mathrm{d}^2 y}{\mathrm{d}z^2} = \frac{\mathrm{d}t_y}{\mathrm{d}z} \simeq \frac{q}{p}B_x \simeq 0 \quad (4.4)$$

The second equation results in a simple linear model for the y-z track projection:

$$y(z) = y_0 + t_y(z - z_0) \quad (4.5)$$

where y_0 and t_y are the coordinate and the slope at the reference position z_0. For the first equation, concerning the x-z track projection, neglecting the dependence of B_y on z so that, and solving the equation 4.4 one gets

$$x(z) = x_0 + t_x(z - z_0) + \frac{q}{p}\frac{B_y}{2}(z - z_0)^2, \quad (4.6)$$

where x_0 is the coordinate at the reference position z_0. In summary, when fitting a trajectory, the model depends linearly on five adjustable parameters: two (y_0 and t_y) related to the y-z projection, and three (x_0, t_x and $B_y q/p$) concerning the x-z projection. Defining $a_x = x_0$, $a_y = y_0$, $b_x = t_x$ and $c_x = \frac{q}{2p} B_y$, the track model can be written as:

$$
\begin{aligned}
x_{track}(z) &= a_x + b_x \cdot z + c_x \cdot z^2 \\
y_{track}(z) &= a_y + b_y \cdot z
\end{aligned}
$$
(4.7)

where the z_0 value will be fixed to the origin of the LHCb coordinates system ($z_0 = 0.0$ mm).

4.6.1 Track parameters

Once the track model is given, it is possible to study parameters of the track from the simulated data samples. The available information of simulated events are

- **All-hits**: all digitized hits[5], without any association to the truth.

- **PR-hits**: all digitized hits associated to the "true" tracks. This is a subsample of the ALL-hits.

True track parameters at generation level (as for instance p, p_T) are also available. The All-hits sample is the sample to be used to determine tracking performances (as for instance those of the Downstream Tracker), while the PR-hits sample can be used to study track parameters and (effective) hit resolution.

In order to quantify the effect of the small fringe field, present in the SciFi Tracker region, axial PR-hits of the track are fitted both to a straight line model ($x_{track}(z) = a_x + b_x \cdot z$) and to a parabola model ($x_{track}(z) = a_x + b_x \cdot z + c_x \cdot z^2$). The returned distribution for the χ^2 variable, for both models, is shown in fig. 4.11. The quality of the parabola fit is much better than the quality of the fit to a straight line, therefore the small fringe field in the SciFi Tracker region cannot be neglected in the track model. As it will be shown in the next chapter this ingredient is crucial in reducing the high level of reconstructed fake tracks that a two-dimensional approach of the retina algorithm returns (see tab 5.2). Fig. 5.14, instead, shows the distribution of the track parameters (a_x, b_x, c_x) returned from the fit of all tracks to the parabola model. The distribution of the c_x parameter is sensitive to the presence of the small fringe magnetic field component in the SciFi region. The size of the parameter is small, however it provides some useful information about the component of the track momentum on the bending plane (see next section).

From the axial fit described above it is possible to determine the "effective" spatial hit resolution for axial layers of the SciFi subdetector, by looking at the distribution of the hit residuals, defined as

$$
R = x^{\mathrm{fit}}(z) - x^{\mathrm{hit}},
$$

---

[5]Digitized hits includes all reconstruction stages and realistic effects: energy deposit, photon production, photon propagation in the fibres, photons conversion in the SiPMs, clusterization of the electrical signals, etc
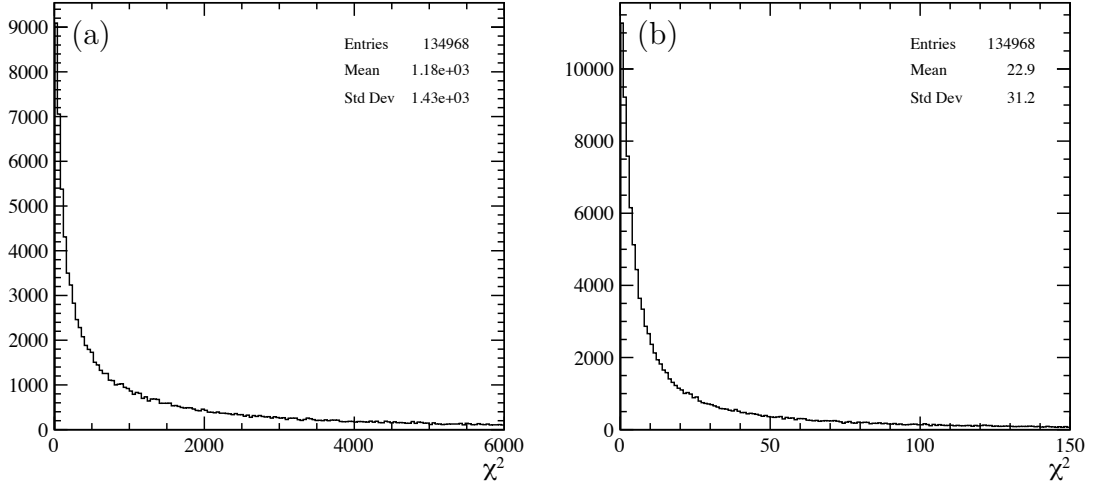
Figure 4.11: Distribution of the returned χ^2 of the axial fit of all reconstructible track. Straight line model (a) and parabola model (b). An hit resolution of $\sigma_{\text{hit}} = 0.1$ mm is assumed in the χ^2 determination.

where $x^{\text{fit}}(z)$ is the predicted x-coordinate of the hit from the axial fit, x^{hit} is the x-coordinate of the hit from PRhit sample. The distribution of the hit residuals is shown in Figure 4.13, both for the straight line and parabola models. Also in this case, the straight line model results to be inaccurate, with a standard deviation of the distribution of 2.57 mm. For the parabola model, instead, a standard deviation of 373 μm is obtained. This is much closer to the nominal spatial resolution of 75μm [7], even if it is larger than a factor of 5. This is expected since the value of 75μm comes from the diameter of the single fibre of 250 μm^6, while the distribution of residuals account for all the reconstruction stages and for all realistic effects, that are fully simulated. It is also worth noting that long tails are present in the distribution, likely due to the approximations assumed to derive the track model.

---

[6]This estimate assumes a uniform distribution: $250/\sqrt{12} = 72.2\mu$ m).

71
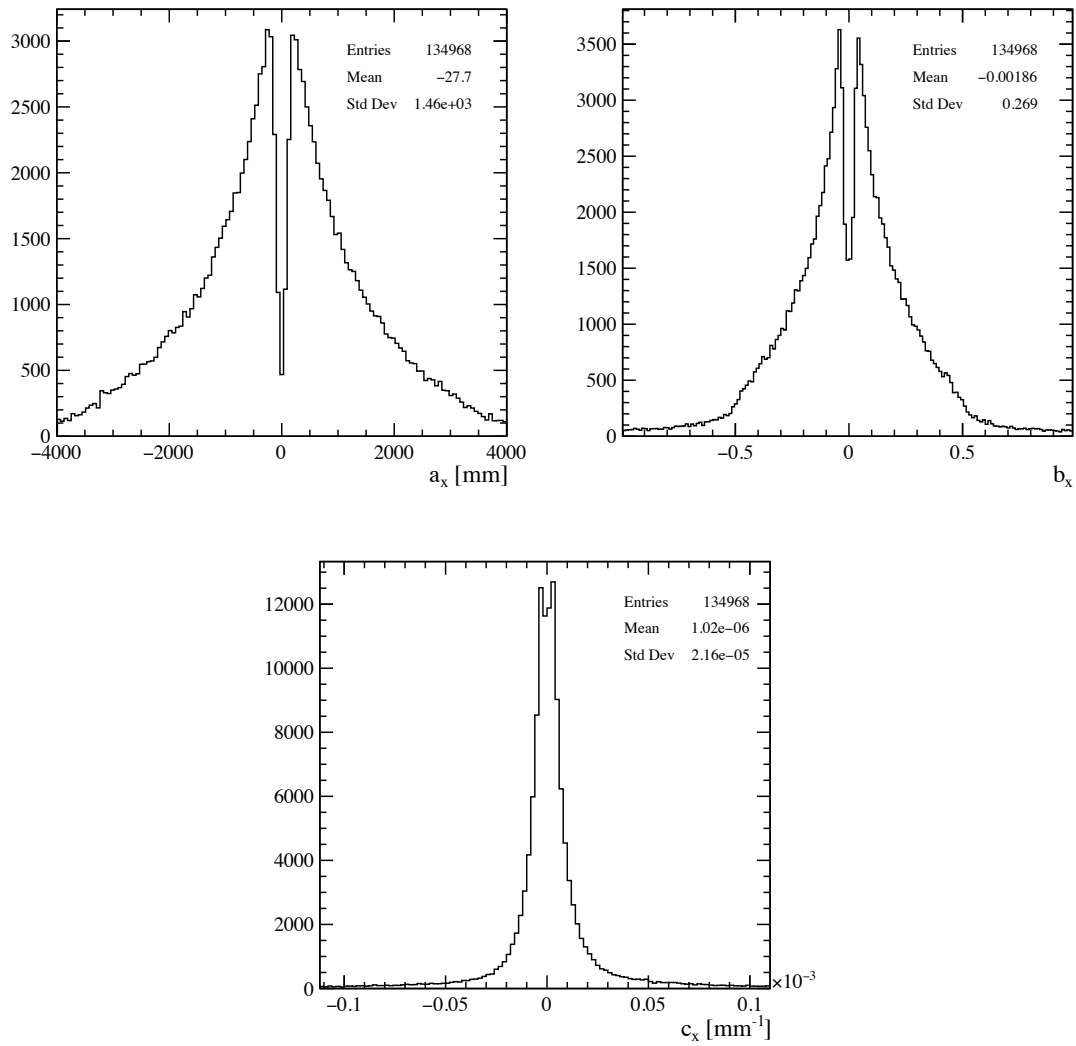
Figure 4.12: Distributions of the track parameters (a_x, b_x, c_X) returned from the fit of all tracks to the parabola model.
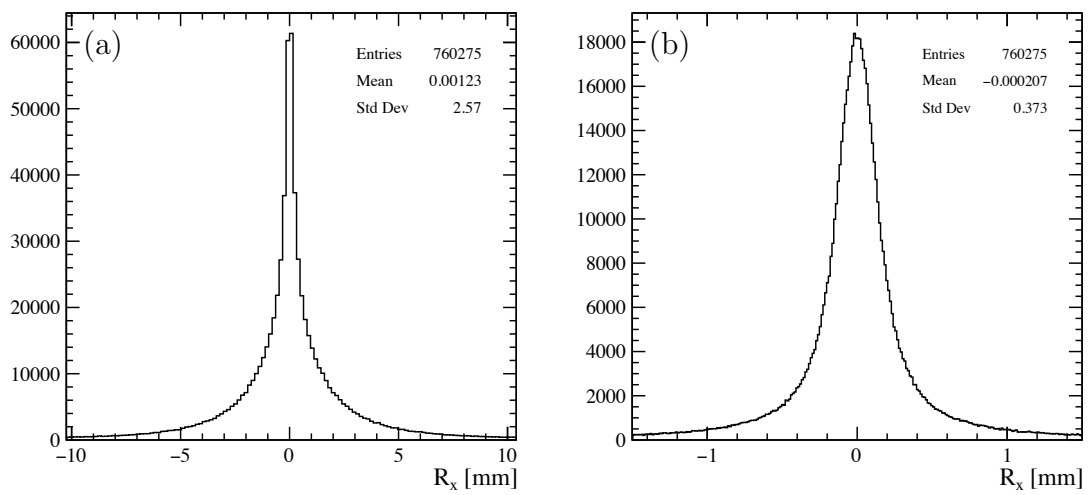
Figure 4.13: The distribution of the hit residuals for the straight line (a) and parabola (b) models.

The same procedure is repeated using both axial and stereo PRhits, with the implementation of a three-dimensional fit. The full track model is used, with a parabola model $(x_{track}(z) = a_x + b_x \cdot z + c_x \cdot z^2)$ for the axial component and a straight line $(y_{track}(z) = a_y + b_y \cdot z)$ for the stereo one. Fig. 4.14 shows the distributions of obtained stereo track parameters, the distribution of the the returned χ^2, and the distribution of residuals for the stereo hits, as previously done for the axial ones.
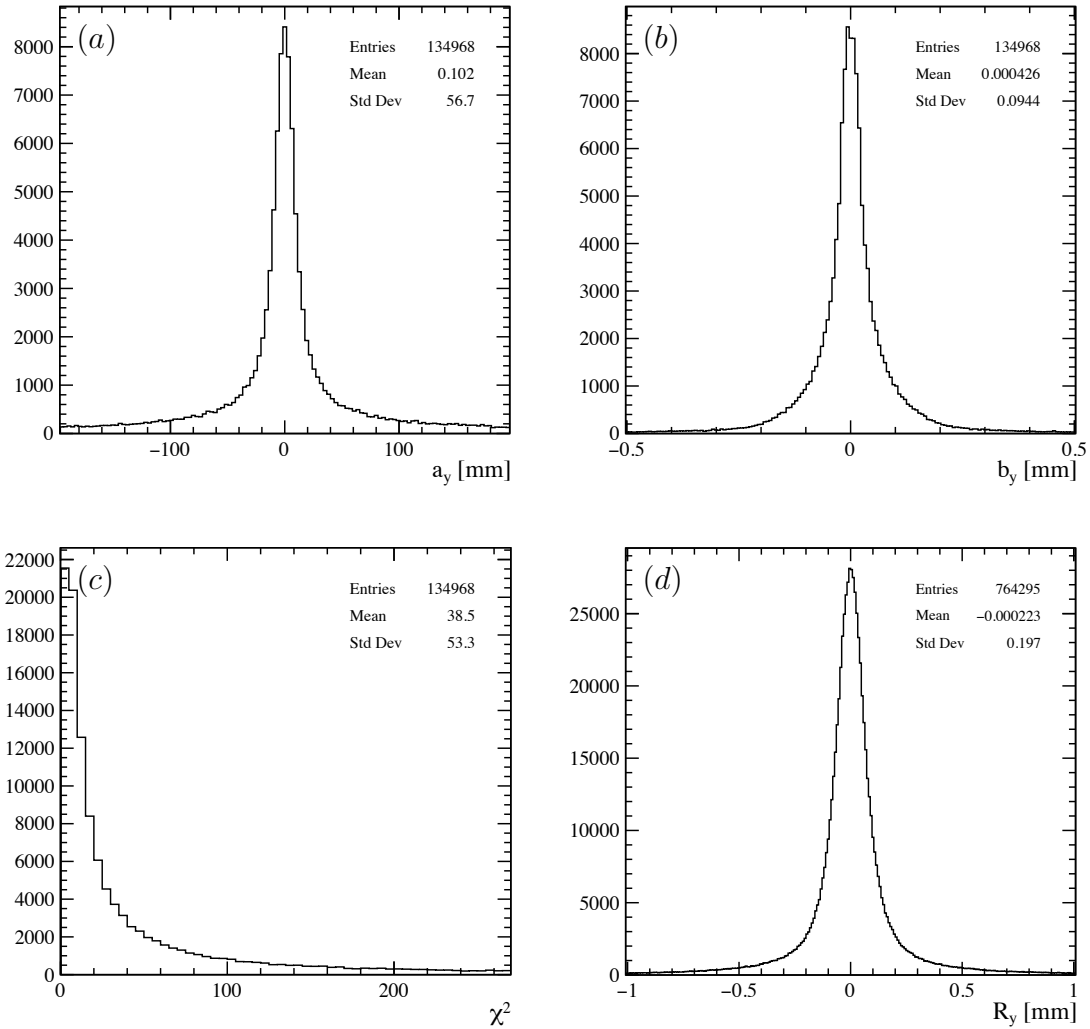
Figure 4.14: Distributions of stereo track parameter a_y (a) and b_y(b) returned from the three-dimensional fit. Distribution of the the returned χ^2, and the distribution of residuals for the stereo hits.
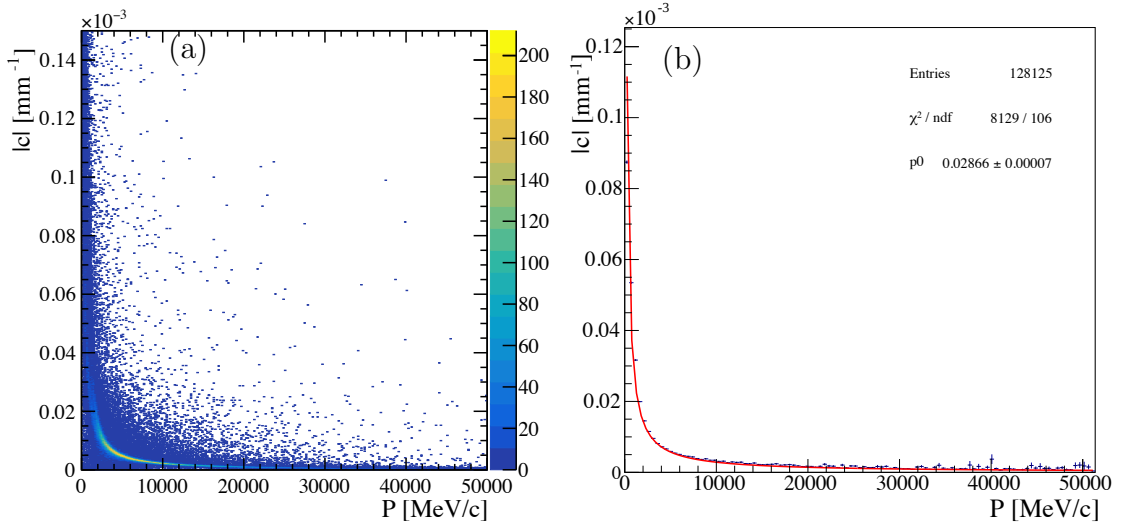
Figure 4.15: Two-dimensional distribution of (c_x, p) (a). Profile histogram of the two-dimensional distribution (c_x, p) (b). The fit result (red line) is superimposed.

4.7 Measurement of the track momentum

The presence of a small, but non negligible, fringe magnetic field allows a measurement of the track momentum. In particular from the track parameter c_x is possible to infer information on the size of the component of the track momentum on the bending plane, i.e. $p_{bending} = \sqrt{p_x^2 + p_z^2}$. The p_z component is usually much larger than the other two components p_x and p_y, for both long and downstream tracks, therefore, for these two track categories, one can safely assume $p_{bending} \approx p$. In fact, from Eq.4.6, where the same approximations hold, it is possible to see that the c_x parameter is directly linked to the momentum p of the track. Fig. 4.15 shows the scatter plot between the true momentum of the track and the measured c_x parameter, returned from the fit of axial PRhits. By profiling the scatter plot, all the resolution effects are removed, and a fit to a function proportional to $1/p$ provides a result which accurately describes the observed behaviour. This result is very important because from the measurement of the small c_x curvature is possible to extract a measurement of the momentum of the track without any assumptions of the type of the track.

Chapter 5

Real-time axial reconstruction of T-tracks

This chapter describes the reconstruction of T-tracks in the Scintillating Fibre Tracker subdetector using the artificial retina algorithm. This is the first stage of the tracking sequence of the envisioned Downstream Tracker device. Particular attention is dedicated to the procedure developed in this thesis in order to reduce as much as possible the number of reconstructed fake tracks ('ghosts') keeping high tracking efficiencies, comparable to the those obtained with the official offline LHCb software. In order to quantify the goodness of the proposed tracking approach the performance indicators will be also defined.

5.1 The Downstream Tracker tracking sequence

Although the chapter focusses only on the axial part of the algorithm, it is useful here to briefly outline also the subsequent stages. The basic stages of the algorithm, based on the artificial retina, conceived to reconstruct three dimensional tracks using solely the information provided by the Scintillating Fibre Tracker can be summarized as follows

1. receptors production;

2. find $x - z$ track projection;

3. removal of $x - z$ false positive tracks (linearized calculation of χ^2_A);

4. add $y - z$ track projection;

5. stereo only two-dimensional fit (or global three-dimensional fit).

The artificial retina algorithm can be efficiently implemented on FPGAs only if a two-dimensional tracking problem has to be solved. Therefore, although the fringe magnetic field in the SciFi Tracker region is not completely negligible, tracks must be approximated as straight lines in the first stage of the their reconstruction
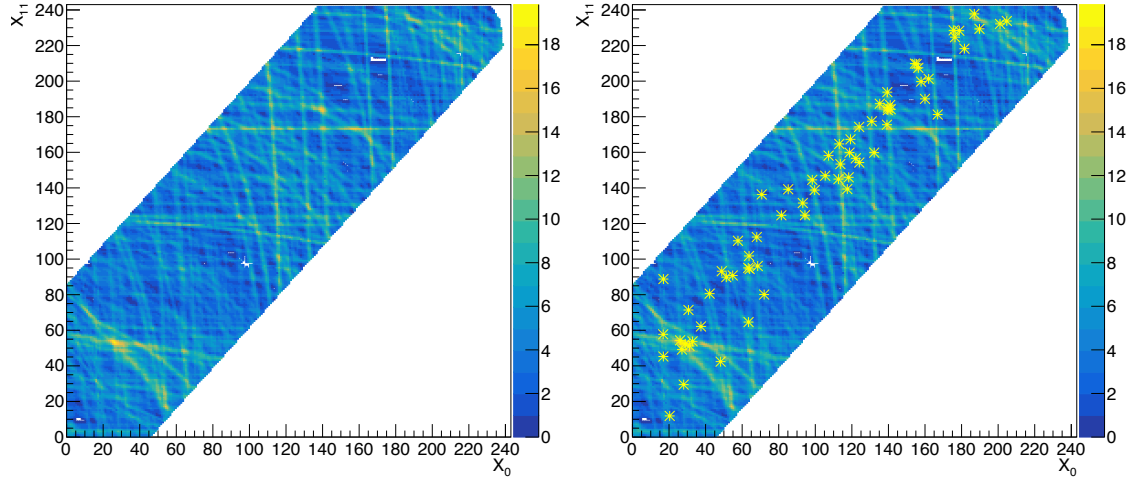
Figure 5.1: Appearance of an axial retina for a single event. The retina filled with the axial hits from the SciFi subdetector is shown on the right, while the same retina is shown on the left but *yellow stars*, indicating positions of true reconstructible tracks, are superimposed.

(pattern recognition) on the axial $x - z$ view[1]. The axial projection of the tracks is therefore parameterized in the two-dimensional space (x_0, x_{11}), where x_0 and x_{11} are the x-coordinates of the intersections of the track with two *virtual planes* located just before the first layer $(0x)$ of the SciFi and just after the last one $(11x)$, respectively. This is the axial retina space, and it is divided into about 10^5 pattern cells (as explained in chapter 3), corresponding precisely to 25800 cells per quadrant[2]. For each pattern cell the associated pattern of hits, namely the intersections of the associated track with the detector layers, is then generated (receptors production)

At this point, simulated hits of the SciFi subdetector (from the All-hits sample), are sent to the axial retina in the (x_0, x_{11}) space[3], in order to solve the pattern recognition in the $x - z$ view. Only for the hits that are distant from the cell receptors less than a fixed distance, i.e the *distance search* d_s, a gaussian weight is calculated and stored into the cell. Hits are therefore accumulated into the axial retina, and immediately after the end of each event (End Event bit), a search for local maxima is performed. Only maxima exceeding a certain excitation level threshold W_T^A are considered (find $x - z$ track projection). Not all the collected maxima are expected to have a truth-matched reconstructed track, so an additional requirement on the χ_A^2 value, provided by a linearized fit calculation using hits accumulated in the local maximum is necessary (removal of $x - z$ false positive tracks). As an example, fig. 5.1 shows the axial retina for a a single event, filled with all hits from the SciFi

---

[1]This will result to be a very good approximation.

[2]Quadrant can be considered independent for track reconstruction purpose, and all the tracking studies, done in this thesis, are performed in a single quadrant.

[3]Actually, a transformation of the coordinates (x_0, x_{11}) is necessary to uniform track distribution in the parameter space. See sec 5.3.

subdetector.

Subsequently, for each axial maximum found passing the χ_A^2 cut, a new search of local maxima is performed by looking at a stereo retina, one for each reconstructed axial track, where only the hit coming from the tilted layers ($u-$ and $v-$layers) are considered. The stereo retinas have a granularity of about $350 - 400$ pattern cells, much lesser than the axial retina, entirely covering all the stereo track space $(y_0, y_{11})^4$ where y_0 and y_{11} are the y-coordinates intersections of the track with the same virtual planes mentioned above. Given an axial track, only stereo hits, compatible with the $x - z$ projection of the associated track are sent to the stereo retina. As for the axial retina, a search for local maxima is performed requiring that the found maxima have to exceed a given threshold W_T^S (add $y - z$ track projection). Lastly, a linearized stereo fit (or a linearized global 3D fit) is performed to extract the track parameters and to associate the correct stereo local maximum to the axial track. This is done by selecting the track with the minimum χ_S^2. As an example, fig. 5.2 shows a stereo retina associated to a reconstructed truth-matched axial track, filled with stereo hits from the SciFi subdetector, compatible with the $x - z$ projection.
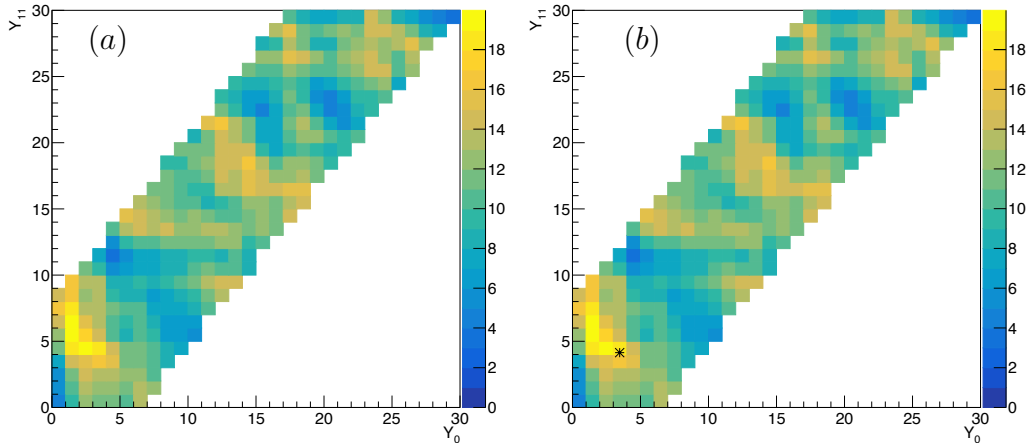
Figure 5.2: Appearance of a stereo retina for a single event, associated to a reconstructed truth-matched axial track. The retina filled with the stereo hits from the SciFi subdetector is shown on the right, while the same retina is shown on the left but a *black star*, indicating the positions of associated true reconstructible stereo tracks, is superimposed.

Before going through each stage, in detail, some definitions are needed in order to define performance indicators for providing a quantitative measurements of the quality of the proposed tracking approach.

---

[4]No coordinates transformation is necessary here because the number of hits entering the stereo retina is much smaller than that of the axial retina.

5.2   Performance indicators

The performance of a tracking algorithm can be determined from simulation studies, comparing the number of tracks the algorithm is able to find (reconstructed tracks) with the maximum number of tracks that it could possibly find (reconstructible tracks). It is also useful to define the tracking performances depending on the track type (Long, Downstream, Upstream, Velo, T-Track). Therefore, also sub-detector reconstructibility criteria are defined in LHCb. Concerning the SciFi, a Monte Carlo simulated particle is said to be reconstructible in the SciFi if it has at least one x-layer and one stereo hit in each station. Therefore the minimum number of hits for a track to be reconstructible in the SciFi is 6. The various sub-detectors reconstructibility criteria are:

1. a Monte Carlo simulated particle is reconstructible in the VELOPix if it fires at least three modules, i.e. if there are clusters (produced out of the pixels) associated to the particle in three or more modules;

2. a particle is reconstructible in the SciFi if there are at least one x-layer and one stereo hit in each of the three tracking stations;

3. a particle is reconstructible in the UT if there is one x-layer and one stereo hit associated to the particle out of the four detection layers.

Therefore, the definition of reconstructibility criteria depending on the track type are the following:

1. A particle is reconstructible as a Velo tracks if it satisfies the VELOPix reconstructibility criteria.

2. A particle is reconstructible as a Upstream track if it satisfies the VELOPix and UT reconstructibility criteria.

3. A particle is reconstructible as a Long track if it satisfies the VELOPix and SciFi reconstructibility criteria.

4. A particle is reconstructible as a Downstream track if it satisfies the SciFi and UT reconstructibility criteria.

In order to state if a track is correctly reconstructed, the Downstream Tracker (DWT) and the official offline reconstruction software have different definitions:

- **DWT.** A reconstructed track is said to be matched to a simulated particle if both the axial and stereo maxima are contained in a 3×3 square centered at the true track parameters position.

- **Offline** A reconstructed track is said to be matched to a simulated particle if they share at least 70% of the hits.

Based on these definitions, one can evaluate the following performances indicators

- the tracking efficiency ($\varepsilon_{\text{Tracking}}$) is defined as the ratio between the amount of reconstructed and matched tracks with respect to the total amount of reconstructible tracks:

$$\varepsilon_{\text{Tracking}} = \frac{\text{reconstructed \& matched}}{\text{reconstructible}};$$

- the ghost rate is the amount of reconstructed tracks not associated to a Monte Carlo particle with respect to the total amount of tracks found by the pattern recognition algorithm:

$$ghost\ rate = \frac{\text{reconstructed not matched}}{\text{reconstructed}}.$$

These tracks arise when hits, mostly coming from different particles or from noise, are randomly combined, producing candidates which pass the quality cuts of the pattern recognition algorithm. Higher track multiplicity events tend to produce more fake tracks than lower ones, so it is also useful to estimate the event-averaged ghost rate.

Tab. 5.1 reports a summary of different flags used to determine efficiencies for different types of tracks.

Name	Property
hasT	reconstructible in SciFi
down (or downstream)	reconstructible in SciFi and UT
long	reconstructible in VELO and SciFi
noVelo	not reconstructible in the VELO
strange	daughter of a strange particle (K^0 , Λ, ..)
from B	belongs to the decay chain of a b hadron
from D	belongs to the decay chain of a c hadron

Table 5.1: Selections used by the performances indicators.

In the next sections each step of the axial tracking sequence of the Downstream Tracker is described in detail, reporting the measured tracking efficiencies and the ghost rate. For these studies, only one quadrant of the SciFi sub-detector is accounted for. Indeed, from the distribution of the intersection of the track with the first and last layers, as shown in fig. 5.3 and fig. 5.4, it is possible to estimate that the fraction of tracks moving from the upper quadrants to the lower quadrants (or vice versa) is only 1.4%, while tracks moving from the right quadrant to the left one (or vice versa) are 4.3% of the total. For these reasons the quadrants can be considered independent for track reconstruction purpose,
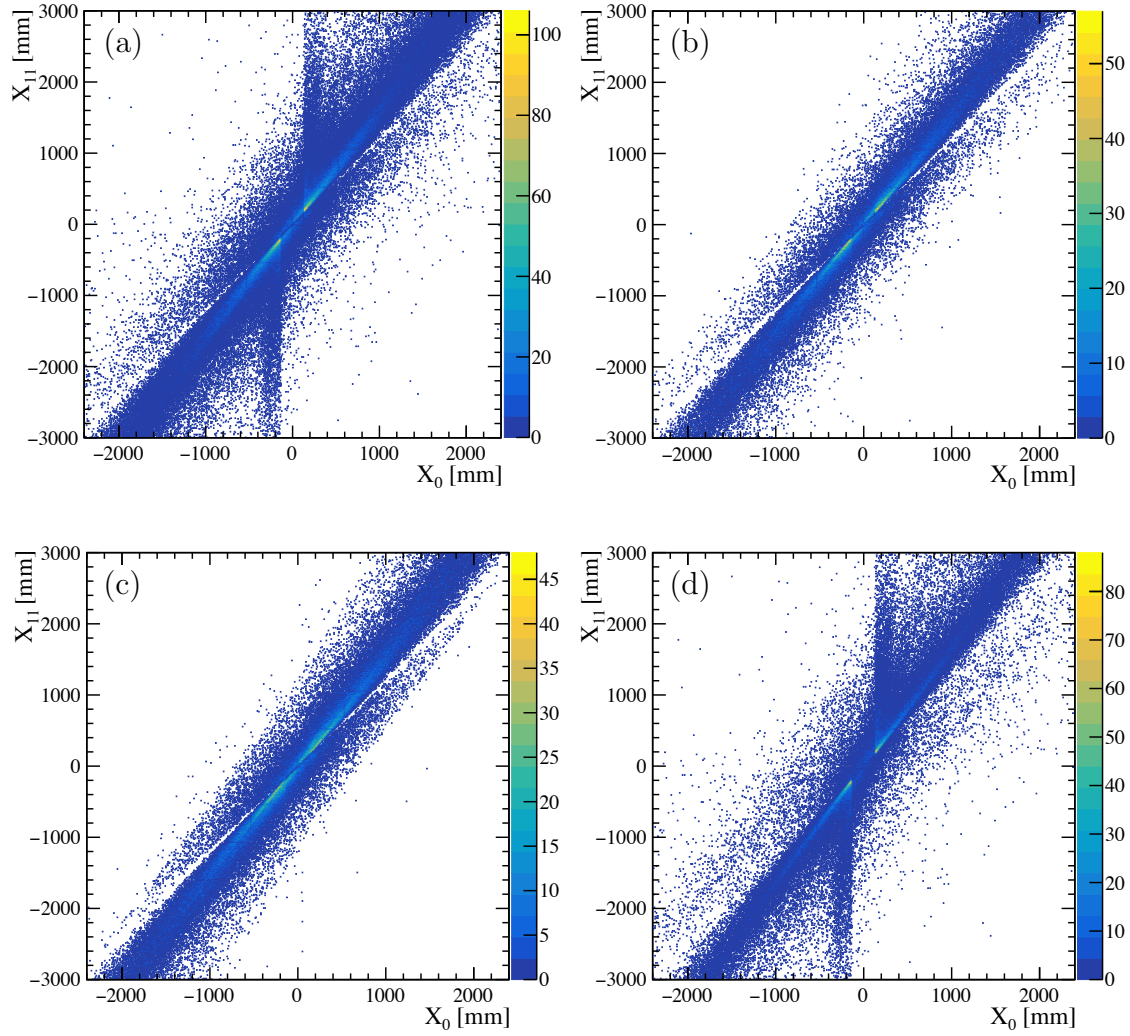
Figure 5.3: Distribution of the track x-coordinate intersections with the first and last layers. All reconstructible tracks (a) all the track are shown, long tracks (b), downstream tracks (c), and tracks reconstructible in the SciFi subdetector that are neither long nor downstream tracks (d).
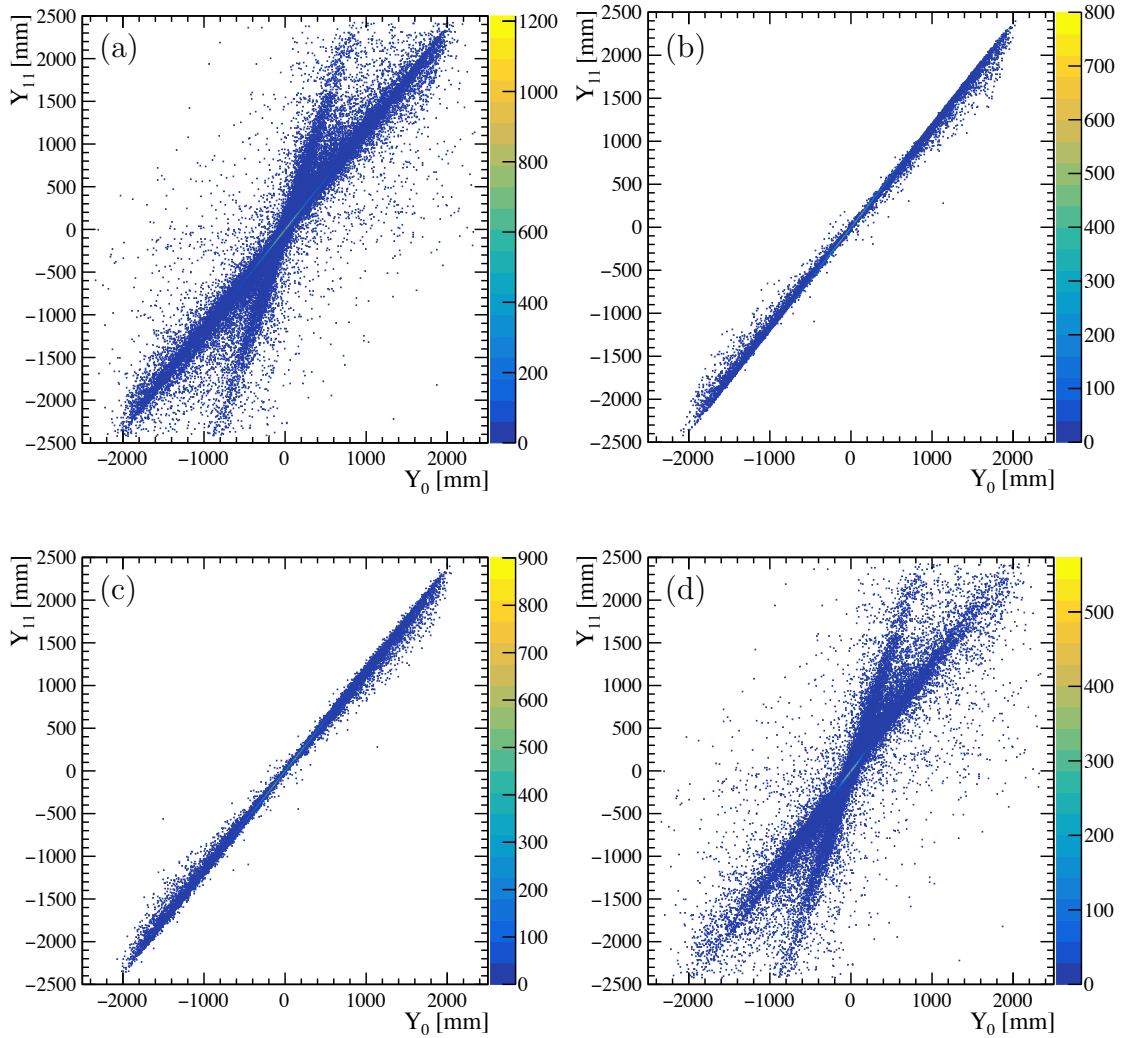
Figure 5.4: Distribution of the track y-coordinate intersections with the first and last layers. All reconstructible tracks (a) all the track are shown, long tracks (b), downstream tracks, and tracks reconstructible in the SciFi subdetector that are neither long nor downstream tracks (d).

5.3 Receptors production on the x-z plane

The official LHCb simulation is used to produce the patterns of hits associated to each pattern cell. This is a preparatory step and it has to be done once, or better to say every time geometry and alignments of the SciFi detector change during the data taking. The output of this procedure is just a list of pre-calculated constants, determined with the LHCb Upgrade realistic simulation, to be loaded on FPGAs.
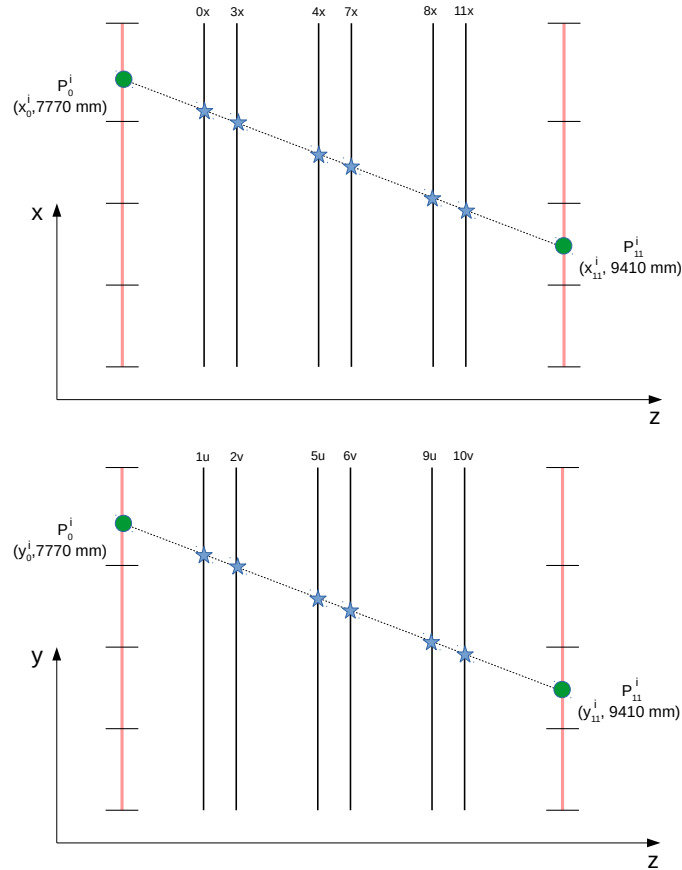
Figure 5.5: Sketch of the procedure used to produce retina receptors, for a given (x_0^i, x_{11}^i) axial pattern cell (a) and for a given (y_0^i, y_{11}^i) stereo pattern cell. The intersections of the particle trajectory with the SciFi layers (*blue stars*) are the so-called *receptor* coordinates, while the green dots indicate the point P_0^i and P_{11}^i to identify the starting point and the momentum direction of the generated muons.

The two parameters chosen to parameterize the phase-space of axial projection of tracks, as already mentioned above, are the intersection x_0 and x_{11} coordinates of the track with two "*virtual*" planes located just before ($z = 7700$mm) the first layer, positioned at $z = 7826$mm, and just after ($z = 9400$mm) the last layer, positioned at $z = 9410$mm. This is motivated by the fact that the simulation is not able to generate particles within the active detector material, as the scintillating fibres. For each ith

retina cell, centered at (x_0^i, x_{11}^i), a single event containing 100 muons with momentum $p = 1$ TeV is generated. Muons are created in the spatial point $P_0^i = (x_0^i, 7700\text{mm})$, just before the first SciFi layer. Assuming a straight line trajectory[5] for all muons, the momentum direction is chosen such that the particle arrival point is the spatial point $P_{11}^i = (x_{11}^i, 9410\text{mm})$, just after the last SciFi layer. Receptors in each SciFi layers are therefore computed as the mean value of the about 100 released hits on each layer. Detector inefficiencies and multiple scattering (that has small effects considering the chosen momentum) are therefore removed from the procedure by the average of several reconstructed hits generated by the same geometrical track.

Reconstructible tracks populates only specific regions of the retina, and furthermore with very different occupancies. In particular the most of tracks are distributed within a diagonal band of the space parameter, as shown in fig. 5.6. This means that not all the phase space needs to be mapped with receptors, but only the diagonal region[6]. Furthermore the tracks are not uniformly distributed, due to the forward detector geometry and the topology of the physics events. As previously mentioned, it is known that the system performance depends on the occupancy, so it is necessary to uniform tracks in the parameter space. To do that, the hits distributions on first and last layers are considered (fig. 5.6). The distributions are fitted with the following function

$$f(x) = \begin{cases} p_0 \cdot x & x < x_{\min} \\ \frac{1}{p_1 + p_2 \cdot x} & x > x_{\min}. \end{cases} \tag{5.1}$$

The $f(x)$ is a discontinuous function, in order to reproduce the observed features. The SciFi sub-detector layers have an hole around the beam pipe that produces the discontinuity clearly visible around the value $x_{\min} = 13$ cm. From the function $f(x)$ it is possible to extract a new function $h(x)$, which is a function of x-coordinate of the hit, in order to change variable, moving from x to $\tilde{x}$, with $\tilde{x}$ uniformly distributed. Such a function is the following

$$\tilde{x} = h(x) = \begin{cases} \frac{p_0 \cdot x}{N \cdot x_{\min}} & x < x_{\min} \\ \frac{p0}{N} + \frac{1}{N} \ln\left(\frac{p_1 + p_2 \cdot x}{p_1 + p_2 \cdot x_{\min}}\right) & x > x_{\min}, \end{cases} \tag{5.2}$$

where N is a normalization constant defined as

$$N = \ln\left(\frac{p_1 + p_2 \cdot x_{\max}}{p_1 + p_2 \cdot x_{\min}}\right).$$

Since the hit distribution is not too different among the various layers, as shown in sec. 4.5, a single set of parameters, obtained by fitting the sum of the hits distributions for all the SciFi layers, is used for the transformation. x-coordinates of all hits of each layer are transformed and the result is shown in fig. 5.7. It can be seen how the tracks are distributed in the transformed phase-space and how the hits are almost uniformly distributed on the first and last SciFi layers.

---

[5]The detector placed afterwards the magnet, so with the selected very high momentum, the
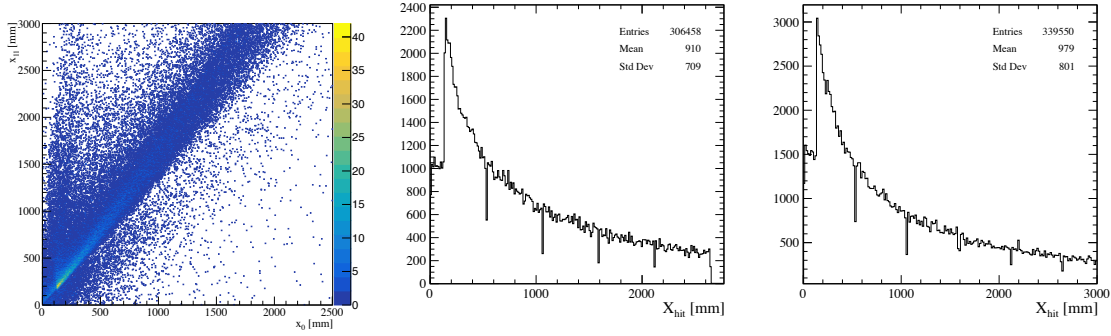
Figure 5.6: Distribution of the $x - z$ track projection in the parameter phase space (left) and hits distribution on the first layer (middle) and last layer (right), i.e. $0x$ and $11x$.
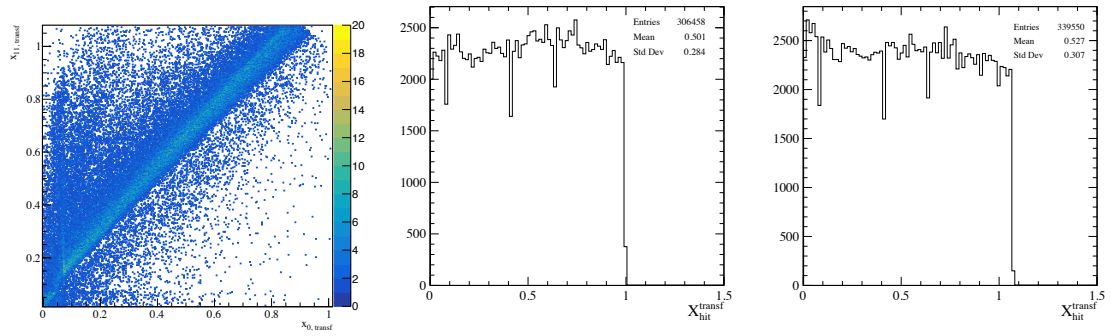
Figure 5.7: Distribution of the $x - z$ track projection in the *transformed* parameter phase space (left) and hits distribution on the first layer (middle) and last layer (right), i.e. $0x$ and $11x$.

The grid of the axial retina is made into the transformed phase space, where tracks are uniformly distributed. In order to find transformed coordinates of receptors on each SciFi layer, the transformed $\tilde{x}_0$ and $\tilde{x}_{11}$ coordinates of each cell are transformed back to the real coordinates x_0 and x_{11}, the receptors production procedure explained above is implemented to find real coordinates of receptors on each SciFi layer, and finally real receptors coordinates are transformed in the new uniform space.

In the following sections and chapters, axial retinas are shown always in the transformed phase space, even if the same x_0 and x_{11} coordinates notation is used.

---

curvature of muons is completely negligible.

[6]That is why retinas displayed in fig. 5.1 and in fig. 5.2 cover only a diagonal region. The same holds for the stereo retinas.

5.4 Find x-z projection

Hits coming from the axial layers of the SciFi detector are sent to the axial retina. The gaussian weights are evaluated and their values is accumulated into the associated cells. In order to obtain the best performance it is important to set some parameters as the sharpness of the receptor response σ and the distance search d_s, i.e. the maximum distance from the receptor such that the gaussian weight is calculated, accumulated, and stored. The first one has a great impact on the largeness of the maxima, while the second one on the amount of weights that have to be calculated. It is clear that they are extremely linked. In fact after some optimization, their values are fixed to be

$$d_s = 2 \cdot \sigma.$$

It is also clear that the value of σ depends on the cell dimension Δx. An empirical relationship that links these two parameters is found to be

$$d_s = \Delta x = 2 \cdot \sigma.$$

Then, a search for local maxima is carried out. In order to evaluate if a maximum is comparable with a true track parameters, it is required that the maximum is contained in a 3×3 square centered at the true track parameters. At this stage a first requirement is applied. The excitation level of local maxima must be higher than a determined threshold W_T^A extracted by comparing the distribution of the excitation levels of all local maxima and the ones that have a positive truth-matching with true tracks. For the study described in this thesis the value $W_T^A = 4$ is chosen, in order to keep reconstruction efficiency as higher as possible, as shown in fig. 5.8.

As it can be deducted from the procedure for generating pattern cells, the system is not able to reconstruct tracks with a very low momentum. Track trajectory is far from being a straight line, and consequently the hit lines do not meet at the expected position and thus the maximum has a lower excitation level, as shown in fig. 5.9. This is an intrinsic limitation due to the space dimensionality of the axial retina, and it strongly depends on the granularity of the retina. Increasing the retina granularity, making the cells much smaller, gets worse the situation with a further decrease of efficiency. However, as shown in tab. 5.10, the loss of efficiency is negligible. Moreover it is worth noting that interesting physics tracks, coming from b- and c-hadrons, or from a long lived particle as K_S^0 or Λ, have an average higher momentum with respect to tracks from a generic inelastic pp collisions. The price to pay, however, having a low retina granularity, is the high level of reconstructed fake tracks, how it is shown in the following.

5.4.1 Axial retina results

Fig. 5.10 shows few examples of excited retinas, where the positions of the true tracks (yellow stars), of the reconstructed tracks (red dots), and of the truth-matched tracks (black dots) are superimposed. The tracking efficiencies, shown
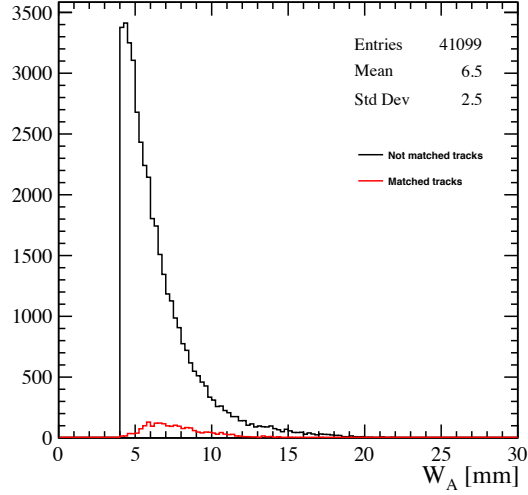
Figure 5.8: Distribution of the excitation level. The requirement $W_{\mathrm{T}}^{\mathrm{A}} \geq 4$ is applied. The distribution of truth matched maxima is in red, while the distribution of non-truth matched maxima is in black.
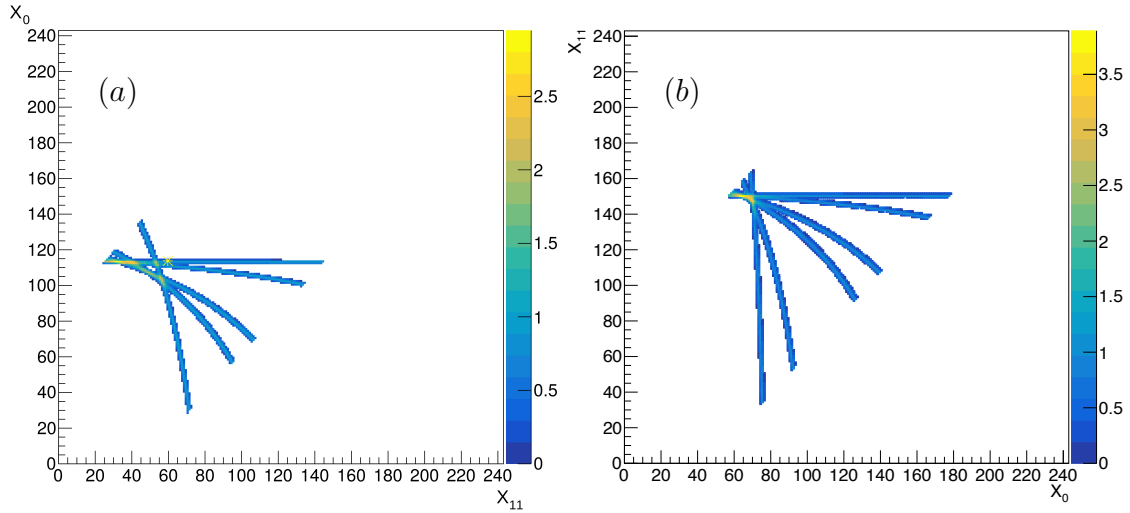
Figure 5.9: Example of low momentum track reconstruction. $p = 408.67$ MeV$/c$ (a) and $p = 1344.9$ MeV$/c$.

in tab. 5.2, are well above the 90% level for all the track categories listed in the table. Results of the *Sample 2* are particularly relevant for the Downstream Tracker. Such a filtered sample contains, in each event, a long lived K_{S}^{0} particle from the $D^{*+} \rightarrow D^{0}\pi^{+} \rightarrow [K_{\mathrm{S}}^{0}\pi^{+}\pi^{-}]\pi^{+}$ decay chain, and the category "down strange" listed in the table, refers to pions from the $K_{\mathrm{S}}^{0} \rightarrow \pi^{+}\pi^{-}$ decay, the most important tracks to be reconstructed by the Downstream Tracker. Reconstruction efficiency for those

Track type	Sample 1 ε_A (%)	Sample 2 ε_A (%)	Sample 3 ε_A (%)
hasT	92.4	92.4	92.9
hasT, $p > 1\mathrm{GeV}/c$	94.3	93.7	94.5
hasT, $p > 3\mathrm{GeV}/c$	95.8	95.0	95.3
hasT, $p > 5\mathrm{GeV}/c$	96.6	95.0	95.7
Long	95.6	95.6	96.1
Long, $p > 1\mathrm{GeV}/c$	95.6	95.6	96.1
Long, $p > 3\mathrm{GeV}/c$	95.9	95.6	95.8
Long, $p > 5\mathrm{GeV}/c$	96.6	95.0	95.8
Down	95.2	95.7	96.3
Down, $p > 1\mathrm{GeV}/c$	95.2	95.7	96.3
Down, $p > 3\mathrm{GeV}/c$	95.6	95.5	96.1
Down, $p > 5\mathrm{GeV}/c$	96.4	95.1	96.5
Down strange	-	98.4	-
Down strange, $p > 1\mathrm{GeV}/c$	-	98.4	-
Down strange, $p > 3\mathrm{GeV}/c$	-	98.7	-
Down strange, $p > 5\mathrm{GeV}/c$	-	97.7	-
ghost avg.	85.9	92.2	91.7

Table 5.2: Tracking axial efficiency ε_A for different simulated samples and different track categories. An excitation level over the threshold $W_T^A > 4$ is required. Results for down strange tracks, that are mainly pions from $K_S^0 \rightarrow \pi^+\pi^-$ decay, are reported only for the *Sample 2*.

tracks is of about 98.0%[7].

As expected the ghost rate is high, reaching the level of 86%-92%. For instance, for an average number of reconstructed track per quadrant of about 35, one expects an average number of reconstructed fake tracks for each quadrant of about $350 - 35 = 315$ tracks per event (assuming a 90% level of ghost rate). In principle, the value of the threshold W_T^A may be increased to values higher than 4. This would certainly help in drastically reducing the ghost rate, but with a non negligible loss of track efficiency. Reducing the ghost rate keeping high tracking efficiencies is therefore of primarily importance, since the higher number of reconstructed track candidates would make useless the usage of the Downstream Tracker both as a track pre-processor for the Event Filter Farm and as a level-0 track trigger. The amount of data to move to the Event Filter Farm would be too big in terms of available internal and external bandwidth of the envisioned device, and any possible requirement on measured track parameters would be completely inefficient in order to reduce the input rate to the Event Filter Farm.

---

[7]Results for down strange tracks are not reported for *Sample 1* and *Sample 3* because of the low statistics.
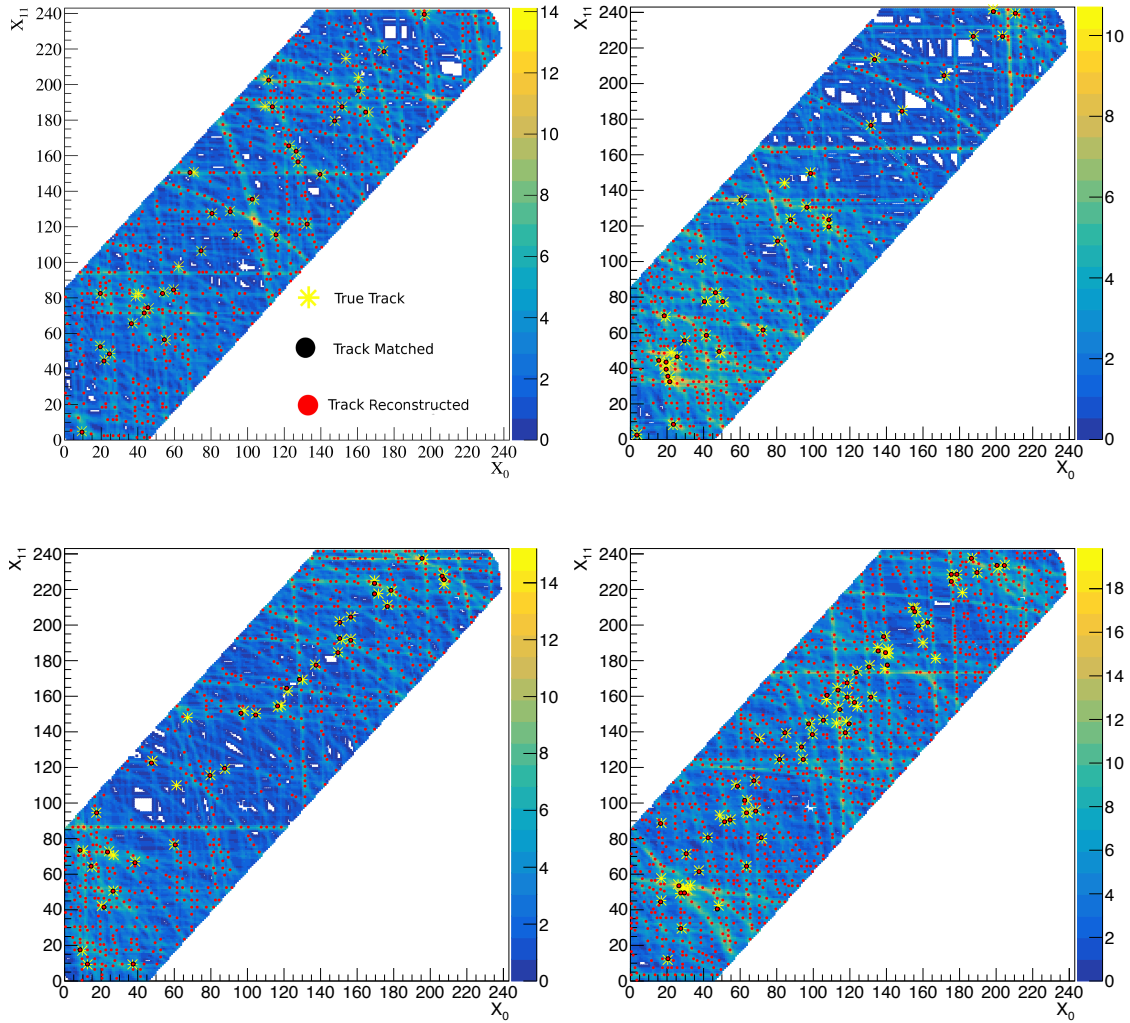
Figure 5.10: Excitation level of few axial retinas filled with SciFi subdetector hits from fully simulated LHCb Upgrade events. True tracks (yellow stars), reconstructed track candidates (red dots), and truth-matched reconstructed track candidates (black dots). Reconstructed tracks candidates are local maxima over threshold ($W_{\mathrm{T}}^{\mathrm{A}} = 4$).

5.5   Remove $x - z$ false positive

In order to reduce the number of false positive reconstructed tracks, additional quality requirements are necessary to be a local maximum

- a minimum number of 4 hits coming from 4 different SciFi layers is required to be present into the cells. This is strictly related to the theoretical upper limit on the reconstruction efficiency, as described in Chap. 4, where the probability to reconstructs tracks with a given number of axial hits larger than or equal to 4 is $\mathrm{Prob}(n_{\mathrm{hit}} \geq 4) \simeq 100\%$ (assuming $\varepsilon_{\mathrm{hit}} = 97.5\%$). This reduces the ghost rate by a factor of about 2.

- a χ^2 value, returned from a fit to the axial hits stored into the local maximum, is required to be less than a determined threshold χ_A^2. The fit is performed considering the combinations of two hits, the two closest hits to the cell receptor for each layer. This is made through a well known linearized fit strategy, suitable to be easily implemented on high-speed FPGA-based system.

5.5.1   Linearized fit strategy

The χ^2 fit aims at recognizing real tracks from accidental combinations of hits [69, 70]. Given that every candidate track is associated to an array on n hits coordinates, the candidate track can be thought as a point within a set $\mathcal{C} \subset \mathbb{R}^n$. Not every point in $\mathcal{C}$ is equally likely to represent a track: only the vector $\overline{x}$ representing hits aligned along a track path have chances to represent real tracks. The set of all $\overline{x}$ aligned along a track path is the subset $\mathcal{T} \subset \mathcal{C}$. Suppose each track can be parameterized by a number $m < n$ of real parameters $\overline{p}$ (e.g. U, V), in the ideal case of perfect resolution, the set $\mathcal{T}$ reduce to a m-dimensional surface contained in $\mathcal{C}$, described by n parametric equations:

$$\overline{x} = \overline{x}(\overline{p})$$

that can also be cast in implicit form, yielding $n - m$ constraint equations:

$$f_i(\overline{x}) = 0 \quad i = 1, \dots n - m$$

These constraint function can be determined from the knowledge of the geometry of the detector. For each candidate track one evaluates the $f_i(\overline{x})$, and accepts the track if all $f_i(\overline{x})$'s are zero. The effect of finite resolution is to make $f_i(\overline{x})$'s slightly different from zero. The measure of this effect is given by the covariance matrix F_{ij} of the $f_i(\overline{x})$, which can be calculated at the first order from the covariance matrix of the coordinates $\overline{x}$. A χ^2 can be formed as:

$$\chi^2 = \sum_{ij} f_i \cdot F_{ij}^{-1} f_j$$

A cut on this quantity can be used to select good tracks with any chosen efficiency. Its value is the same one would obtain for the minimum of the usual χ^2 from a

standard fitting procedure of the parameters $\overline{p}$. F_{ij}^{-1} is symmetrical, then it can be diagonalized, and the constraints redefined accordingly:

$$F_{kl}^{-1} = M_{ki}\frac{\delta_{ij}}{\sigma_i^2}M_{jl}$$

$$\widetilde{f}_i = \frac{M_{ij}f_i}{\sigma_i}$$

χ^2 expression can be simplified and rewrites as:

$$\chi^2 = \sum_i \widetilde{f}_i^2$$

We need to compute the values of the constraint functions $\widetilde{f}_i(\overline{x})$ for each candidate track. Generally speaking, they can be quite complicated functions, however, experience has shown that in vast majority of tracking problems they can be approximate with quite good precision by linear expansions about some convenient point $\overline{x}_0$:

$$\widetilde{f}_i \simeq \frac{\partial \widetilde{f}_i}{\partial \overline{x}} \cdot (\overline{x} - \overline{x}_0) = \overline{v}_i \cdot \overline{x} + c_i$$

Geometrically, this amounts to approximating $\mathcal{T}$ with its tangent hyperplane in $\overline{x}_0$, and $\overline{v}_i$'s are the vector orthogonal to the hypersurface in $\overline{x}_0$. The approximation works well when $\mathcal{T}$ is nearly flat. In general, in order to obtain a sufficient precision, it is necessary to segment $\mathcal{T}$ in several smaller region, and perform the expansion around the central point $\overline{x}_0$ of each of them.

All constant can be calculated numerically starting from a sample of vector $\overline{x}$ belonging to $\mathcal{T}$. The variance of any linear function $y(\overline{x}) = \overline{v} \cdot \overline{x} + c$ evaluated in this sample is given, to the first order, by:

$$\sigma_y^2 \simeq \overline{v} \cdot M \cdot \overline{v}$$

where M is the covariance matrix of $\overline{x}$, estimated from the sample as:

$$M \simeq \frac{N}{N-1}\langle(x_i - \langle x_i\rangle)(x_j - \langle x_j\rangle)\rangle$$

If it append that $y = 0$ for all $\overline{x}$ in our sample, then $\overline{v} \cdot M \cdot \overline{v} = 0$, and since M, being a covariance matrix, has no negative eigenvalues, it follows that $\overline{v}$ is an eigenvector of M with eigenvalue 0. We can find out the $\overline{v}_i$ taking any base of the Kernel of M. The corresponding constant c_i are determined by imposing $\langle \widetilde{f}_i\rangle = 0$, that gives $c_i = -(\sum \overline{v}_i \cdot \overline{x})/N$.

Parameter extraction

The set of tracks can be labeled by using m parameters:

$$\mathbf{x} = \mathbf{x}(p_1, \ldots, p_m)$$

This relations can be inverted (at least locally) to obtain the parameters as functions of the hits coordinates:

$$p_i = p_i(\mathbf{x})$$

For fast calculation, it is desirable to approximate those functions with m linear functions, as did for the constraints:

$$p_i \sim \omega_\mathbf{i} \cdot (\mathbf{x} - \mathbf{x_0}) + p_i(\mathbf{x_0}) = \omega_\mathbf{i} \cdot \mathbf{x} + q_i$$

The constants $\omega_\mathbf{i}$ and q_i can be found by maximizing the resolution, that is, by minimizing the average quadratic deviation from the true values $\tilde{p}_i$:

$$\frac{\partial \left\langle (\tilde{p}_i - p_i(\mathbf{x}))^2 \right\rangle}{\partial \omega_\mathbf{i}} = 0$$

This is easy found by writing formally:

$$\tilde{p}_i - p_i(\mathbf{x}) = \vec{W}_i \cdot \vec{X} + q_i$$

where $\vec{W}_i$ and $\vec{X}$ are $n + 1$ components vectors:

$$\vec{X} = (\mathbf{x}, \tilde{p}_i) \vec{W}_i = (\omega_\mathbf{i}, -\mathbf{1})$$

The covariance matrix C of the newly defined vector $\vec{X}$ is:

$$C = \begin{bmatrix} \mathbf{M} & \gamma \\ t\gamma & \sigma_{\tilde{p}_i}^2 \end{bmatrix}$$

where $\gamma = \langle \tilde{p}_i \mathbf{x} \rangle - \langle \tilde{p}_i \rangle \langle \mathbf{x} \rangle$. The variance of $\tilde{p}_i - p_i(\mathbf{x})$ can now e written in terms of C:

$$\sigma^2(p_i - \tilde{p}_i) = \vec{W}_i \cdot C \cdot \vec{W}_i = \omega_\mathbf{i} \cdot \mathbf{M} \omega_\mathbf{i} - 2\omega_\mathbf{i} \cdot \gamma + \sigma_{\tilde{p}_i}^2$$

and by taking the minimum of this expression:

$$\omega_\mathbf{i} = \mathbf{M}^{-1} \cdot \gamma = \mathbf{M}^{-1} \cdot \frac{\sum \tilde{p}_i \mathbf{x} - \sum \tilde{p}_i \sum \mathbf{x}/N}{N - 1}$$

from which it is also possible to calculate q_i:

$$q_i = \langle \tilde{p}_i \rangle - \langle \omega_\mathbf{i} \cdot \mathbf{x} \rangle$$

These constants are obtained from a sample of tracks with *known parameters*. That is an important difference with respect to the case of the constraints previously

discussed, where it is possible to obtain the constants from a sample of real tracks. In this case only fully simulated events can be used.

The linearized χ^2 fit was used in the CDF Silicon Vertex Tracker (SVT) [69, 70] to perform track finding and fitting at very high speed, in a specific application with integrated circuits (ASIC). This approach is suitable for an implementation of modern FPGAs because they have a high number of digital signal processor (DSP) to perform sums and multiplications (scalar products) at very high speed. In addition, due to the use of a fine subdivision of the parameter space, the artificial retina approach already has a grid of expansion points conveniently available. As far as this thesis, I implemented the linearized fit, described above, within the C++ simulation software I wrote to designed and develop the application of the retina algorithm to the Downstream Tracker.

The chosen retina granularity ensures the presence of true track hits, within the two nearest hits to the receptors, accumulated into the local maxima. This implies that the hardware implementation of the axial retina must have the capability of storing (at least temporarily) these two nearest hits, for each receptors. Such a functionality extension can be realized with a very small amount of additional logic. It is also worth noting that this approach is strongly dependent on the retina occupancy and it has been optimized with a toy simulation with occupancies similar and/or larger than those of the LHCb Upgrade. In fact, if the average number of tracks, and therefore the average number of hits, entering the axial retina, increases, it is no longer guaranteed that the true hits are within the two nearest hits to the receptors, at the given retina granularity. This automatically translates into a loss of efficiency.

In order to avoid about a 15% loss of efficiency, requiring the presence of 6 hits per track (one for each SciFi layer), 5 hits out of 6 are requested. Therefore the linearized χ^2 fit is implemented for 6 different configurations, that differs because the removal of one of the SciFi layers. According to the particular missing SciFi layer, six different M matrices are calculated

$$
M_0 = \begin{bmatrix}
0 & 0 \\
0.09800219972951 & 0.16232477782774 \\
-0.06373258898363 & -0.74724872701151 \\
-0.35625328960415 & 0.61821604572780 \\
0.79643679369939 & 0.11087795995266 \\
-0.47445310963010 & -0.14417005682271
\end{bmatrix}
$$

$$
M_1 = \begin{bmatrix}
0.06143276561316 & 0.10511651829371 \\
0 & 0 \\
-0.03470258028321 & -0.71667504625680 \\
-0.34145230108233 & 0.65343263662339 \\
0.80114171620601 & 0.13313511111435 \\
-0.48641959548406 & -0.17500922043879
\end{bmatrix}
$$

$$M_2 = \begin{bmatrix} -0.01658707213323 & -0.51876800368870 \\ -0.05924112177238 & 0.77109195422635 \\ 0 & 0 \\ 0.39773090227666 & -0.31208538653852 \\ -0.78793413540375 & -0.10634327536801 \\ 0.46603142186867 & 0.16610471326647 \end{bmatrix}$$

$$M_3 = \begin{bmatrix} -0.07398953825441 & -0.48867227341425 \\ -0.04764444761441 & 0.79392003652622 \\ 0.38315738712089 & -0.33049028843780 \\ 0 & 0 \\ -0.76764816268917 & -0.09069369556475 \\ 0.50612475720425 & 0.11593622225805 \end{bmatrix}$$

$$M_4 = \begin{bmatrix} -0.02650375912099 & -0.51586434148910 \\ -0.10606953923398 & 0.80552221889281 \\ 0.72528681671587 & -0.13626092088479 \\ -0.67474226331745 & -0.24205503834880 \\ 0 & 0 \\ 0.08202874612325 & 0.08865808423158 \end{bmatrix}$$

$$M_5 = \begin{bmatrix} 0.09273734187084 & -0.48682901804626 \\ -0.02410402075265 & 0.80425214388542 \\ -0.65430516850218 & -0.28692941510418 \\ 0.73510155143586 & -0.14444161758136 \\ -0.14942970639803 & 0.11394790960025 \\ 0 & 0 \end{bmatrix}$$

while the elements of costant vectors c_1^j and c_2^j (j runs over the missing layer) are

$$\mathbf{c}_1 = \begin{bmatrix} -0.05449990875609 \\ -0.05140945661738 \\ 0.04724054526380 \\ 0.08572186224779 \\ 0.07560492984302 \\ -0.05884708928395 \end{bmatrix} \quad \mathbf{c}_2 = \begin{bmatrix} -0.08470651102742 \\ -0.08226670217913 \\ 0.00350812275665 \\ -0.03178271158187 \\ -0.01709566865692 \\ -0.03951597400886 \end{bmatrix}.$$

This approach, therefore, requires to calculate the linearized χ^2 for all combinations of two hits per receptor, and for 5 SciFi layers out of 6. The maximum number of possible combinations can be easily calculated and it is equal to $6 \cdot 2^5 = 192$. Fig. 5.11 shows the distribution of the number of combinations performed per each reconstructed track (local maximum) for the fully realistic LHCb *Sample 1* (Minimum Bias). Combinations are done starting from the closest hits to the receptors, which have a high probability to be the correct ones. Therefore the maximum number of combinations is never reached. In particular the closest hit is the correct one for the most of the times, resulting in a very small number of "effective" combinations to be calculated.
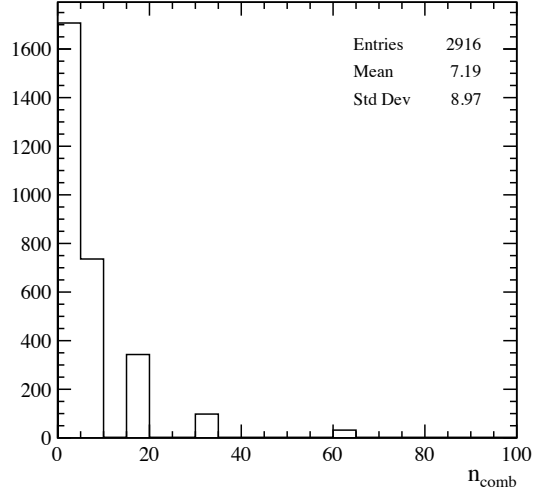
Figure 5.11: Number of χ^2 combination evaluated. The distribution is peaked around 7 combination.

Step	N_{product}	N_{sum}
$\tilde{f}_i = \bar{x} \cdot \bar{v}_i + c_i$	$n \cdot (n-m)$	$n \cdot (n-m)$
$\tilde{f}^2$	$(n-m)$	0
$\chi^2 = \sum \tilde{f}^2$	0	$n - m - 1$
$\vec{p}$ estimation	$n \cdot m$	$n \cdot (m)$
Total	$n_{\text{comb}} \cdot (n+1) \cdot (n-m) + n \cdot m$	$n_{\text{comb}} \cdot [(n+1) \cdot (n-m) - 1] + n \cdot m$

Table 5.3: Estimation of the number of operation that have to be performed in order to evaluate the χ^2 of a candidate track. n_{comb} is the number of combination to compute.

DSP number estimation

A digital signal processor (DSP) is a specialized microprocessor, optimized for the operational needs of digital signal processing. An estimation of the needed number of DSPs on a single FPGA chip to implement the above described method is now carried out. Given a vector of n hits, that has to be fitted with a function with m parameters, it is possible to compute the matrix $M(n, n-m)$. The eigenvalues of the M matrix can be computed and stored. The number of necessary operations to compute the $\tilde{f}_i$ and the χ^2_A are reported in Tab.5.3. In our case ($n = 5$ and $m = 3$), a total number of products $N_{\text{products}} = 12$ and a total number of sums $N_{\text{sum}} = 11$ are required to calculate the χ^2 of a candidate track. These numbers have to be multiplied by the number of combinations, since the two closest hits to the receptors per each layer, are assumed to be stored in the pattern cell. The maximum number of combinations can

be easily calculated and it is $N_{\text{comb,max}} = 192$. Once the track candidate is found, parameters are computed. So, the maximum number of operations required to evaluate the linearized χ^2 and the parameters is $N^{\text{MAX}}_{\text{products,total}} = (2304 + 15) = 2319$ and $N^{\text{MAX}}_{\text{sum,total}} = (2112 + 15) = 2127$. Assuming to put an upper bound of 50 combinations, one obtains $N^{50}_{\text{products,total}} = (600 + 15) = 615$ and $N^{50}_{\text{sum,total}} = (550 + 15) = 565$. With these assumptions, the total number of combinations to be computed for each track are equal to 1180. Since the average number of tracks per event is about 136 track/event, and assuming a ghost rate of 43% (after requiring a minimum number of 4 hits on different layers), the total candidate tracks to be fitted are approximately 238 tracks. Since the maximum number of tracking boards, namely of FPGA chips, for the axial $x - z$ reconstruction is 78, one for each Event Builder PC nodes, each FPGA has to process an average number of 3 candidate tracks. Since the current available Standard-Precision Fixed Point DSPs are able to compute two products (or two sums) in a cycle of clock, an FPGA chip with 2520 DSPs (for example the Altera/Intel Stratix 10 GX) is able to make 5040 operations per clock cycle. In principle few clock cycles are needed to calculate the χ^2 of the 3 candidate tracks. This is just a simple calculation and a precise number of clock cycles needed to calculate the the axial χ^2_{A} needs a full hardware implementation of the algorithm described in this thesis. Anyway adding a bunch of clock cycles to 500 ns measured latency of the system should not be an issue, being the the envisioned maximum latency of the the Downstream Tracker should not exceed the value of 3μs (while the design latency of the Event Builder is about 13 μs).
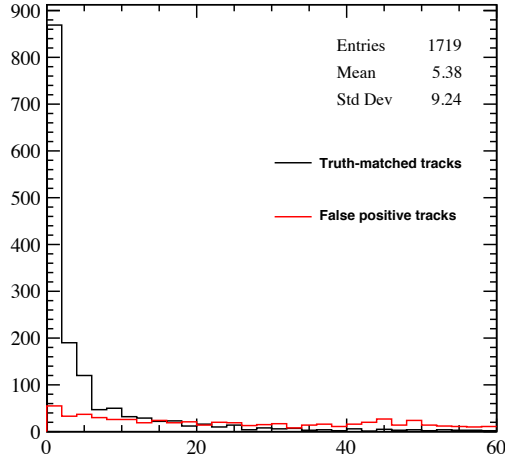
Figure 5.12: Distribution of the axial linearized χ^2_A for truth-matched track candidates (black line) and for fake track candidates (red line).

5.5.2   Results

The linearized χ^2 fit is therefore calculated for each local maximum over the pre-determined threshold of $W^A_T = 4$, having at least 4 axial hits coming from 4 different SciFi layers. The χ^2 is calculated for all the six SciFi layers configurations, only using the two closest hits to the receptors. The local maximum is accepted as a track candidate if the linearized axial χ^2_A value is lesser than a threshold, $\chi^2_A < 20$, as shown in fig. 5.12

Fig. 5.13 shows few examples of excited retinas, where the position of the true tracks (yellow stars), of the reconstructed tracks (red dots) passing also the requirement on the linearized χ^2_A, and of the truth-matched tracks (black dots) are superimposed. It is clearly visible that the fraction of fake tracks (or ghosts) is drastically reduced. The resulting tracking efficiencies, shown in tab. 5.4, are close to the 90% level for the track categories where a minimal requirement on the track momentum is applied[8]. It is worth noting that downstream tracks are reconstructed with an efficiency of about 90% in the three samples considered. The measured tracking efficiencies of the *Sample 2* are particularly relevant for the Downstream Tracker. As already mentioned, the *Sample 2* contains in each event a long lived K^0_S particle from the $D^{*+} \to D^0\pi^+ \to [K^0_S\pi^+\pi^-]\pi^+$ decay chain. Down strange tracks[9] (with $p > 3GeV/c$) are reconstructed with an efficiency of about 90%. The ghost rate is drastically reduced less than the 20% level. Both tracking efficiencies and

---

[8]$p > 1, 3, 5$ GeV/c are very minimal requirements that almost the majority of LHCb analyses uses for physics signal tracks. They are also very close to intrinsic limit of the LHCb Upgrade tracking system, including Velo and Upstream Tracker.

[9] *strange* downstream tracks are mainly pions from $K^0_S \to \pi^+\pi^-$ decay.

ghost rate are at the same level of those obtained with the offline reconstruction software program (see chapter 7). This is clearly a remarkable result of this thesis. The pattern recognition in the axial $x - z$ view can be fully solved in real-time with a number of about 10^5 elementary pattern cells to be implemented in a system of about 78 tracking boards equipped with modern currently available FPGA chips, to be integrated in the LHCb Event Builder system during the LHC LS3.
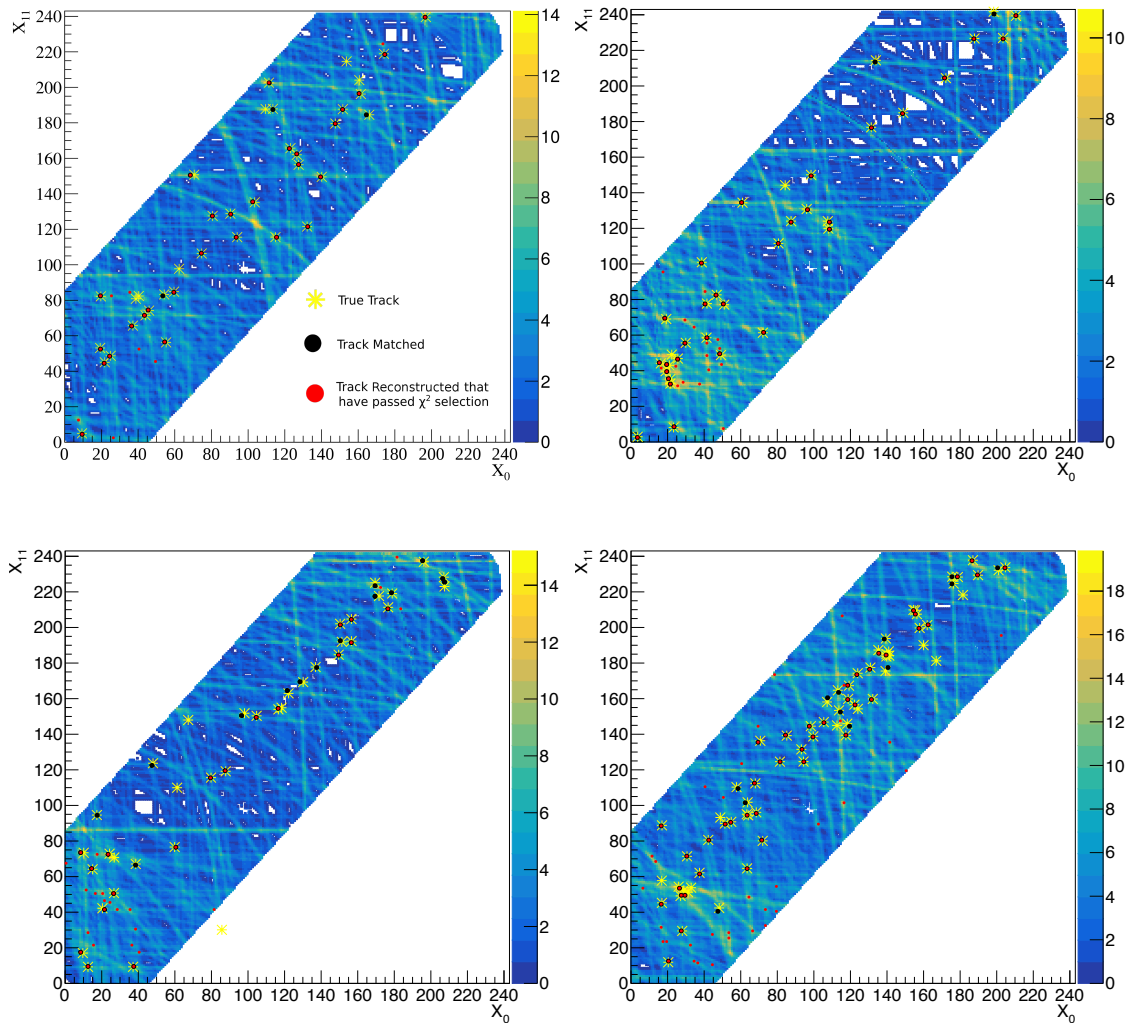
Figure 5.13: Excitation level of few axial retinas filled with SciFi subdetector hits from fully simulated LHCb Upgrade events. True tracks (yellow stars), reconstructed track candidates (red dots), and truth-matched reconstructed track candidates (black dots). Reconstructed track candidates are local maxima over threshold ($W_{\mathrm{T}}^{\mathrm{A}} = 4$), have at least 4 axial hits coming from 4 different SciFi layers, and passes the $\chi_{\mathrm{A}}^2 < 20$ requirement.

Track type	Sample 1 ε_A (%)	Sample 2 ε_A (%)	Sample 3 ε_A (%)
hasT	75.0	74.4	73.9
hasT, $p > 1\mathrm{GeV/c}$	77.6	77.7	76.4
hasT, $p > 3\mathrm{GeV/c}$	87.0	85.9	85.1
hasT, $p > 5\mathrm{GeV/c}$	90.3	88.2	86.6
Long	81.7	84.1	84.2
Long, $p > 1\mathrm{GeV/c}$	81.7	84.1	84.2
Long, $p > 3\mathrm{GeV/c}$	87.3	87.1	87.3
Long, $p > 5\mathrm{GeV/c}$	90.6	88.1	88.1
Down	80.1	83.0	82.6
Down, $p > 1\mathrm{GeV/c}$	80.1	83.0	82.6
Down, $p > 3\mathrm{GeV/c}$	87.0	87.1	86.5
Down, $p > 5\mathrm{GeV/c}$	90.5	88.8	87.9
Down strange	-	84.7	-
Down strange, $p > 1\mathrm{GeV/c}$	-	84.7	-
Down strange, $p > 3\mathrm{GeV/c}$	-	89.4	-
Down strange, $p > 5\mathrm{GeV/c}$	-	93.0	-
ghost avg	12.1	16.3	18.4

Table 5.4: Tracking axial efficiency ε_{A} for different simulated samples and different track categories. Reconstructed track candidates are local maxima over threshold with $W_{\mathrm{T}}^{\mathrm{A}} > 4$), have at least 4 axial hits coming from 4 different SciFi layers, and passes the $\chi_{\mathrm{A}}^2 < 20$ requirement. Results for down strange tracks, that are mainly pions from $K_{\mathrm{S}}^0 \to \pi^+\pi^-$ decay, are reported only for the *Sample 2*.
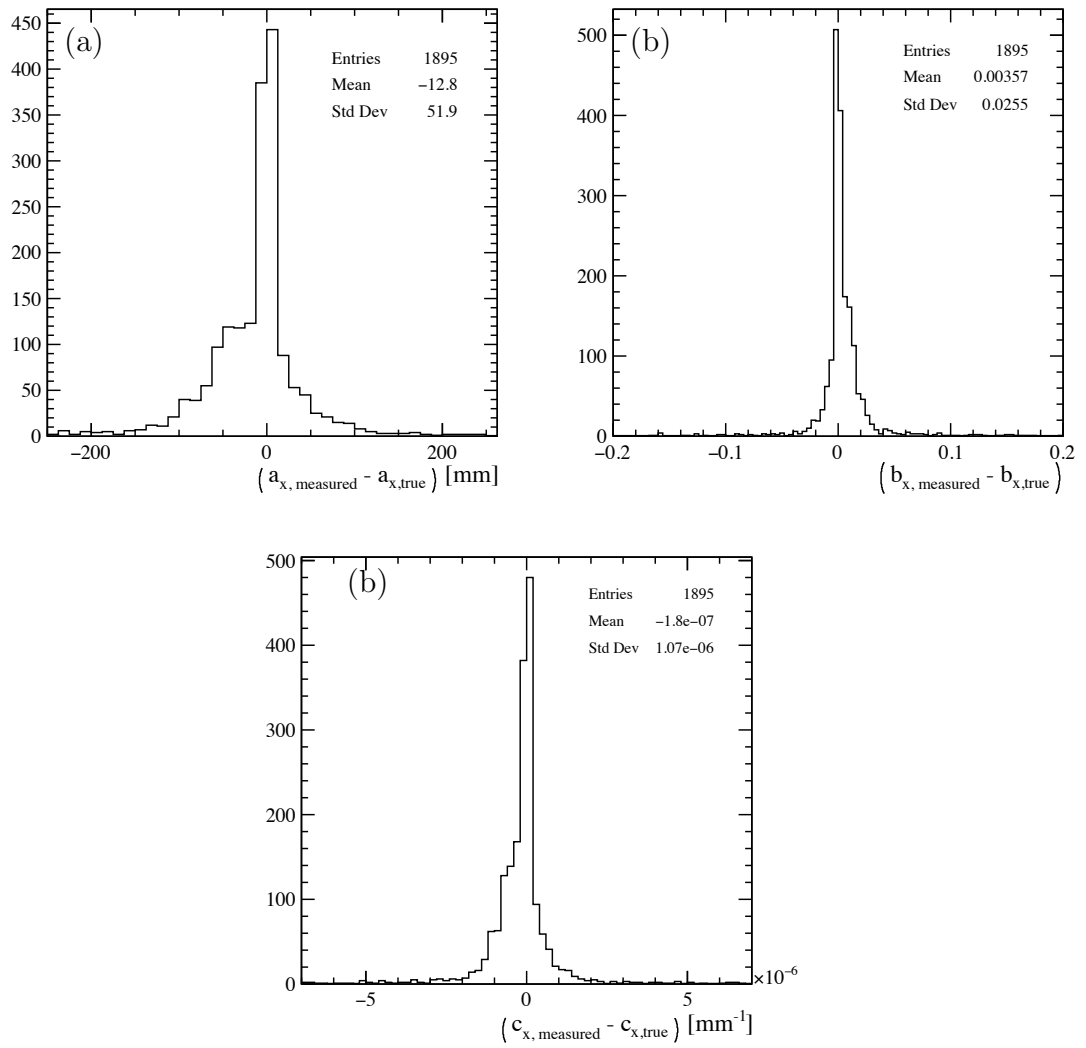
Figure 5.14: Difference between the true track parameters and the parameters provided by the linearized χ^2 fit.

Chapter 6

Real-time three-dimensional reconstruction of T-tracks

This chapter describes the first implementation of a full three-dimensional realtime reconstruction of T-tacks in the Scintillating Fibre Tracker of the LHCb Upgrade. The information from the stereo tilted u/v-layers is used in conjunction with the axial information. Different configurations of the algorithm are studied in order to assess stability of the tracking performance. This is the first attempt to reconstruct three-dimensional tracks in a realistic environment, as the Downstream Tracker, using the artificial retina algorithm.

6.1   Receptor production on the y-z plane

As for the axial part, the parameters describing the $y - z$ view of the track projection are chosen to be y_0 and y_{11}, the y-coordinates of intersections on the virtual planes of the track associated to the relative pattern cell. Since the fringe magnetic field on the $y - z$ view is very small, the same approximations used for the axial part hold, and are much more accurate. Tracks are straight lines with a high level of accuracy. Therefore, in order to calculate retina receptors for track pattern cells in the (y_0, y_{11}) parameter space, the same procedure used to determine receptors for the axial retina is adopted (see sec. 5.3). As explained in the next section, only a small fraction of stereo hits needs to be loaded on the $y - z$ retina, the only ones compatible with trajectory of the relative found axial track. For this reason, differently from what is done for the axial retina, a transformation of the track parameters (y_0, y_{11}) is not necessary here.

6.2   Add y-z projection

The selected x-z projection track candidates contain only hits from x-layers and have an estimation of the x-z plane parameters (a_x, b_x, c_x). The y-z plane track motion is extracted from the u/v-layers since their local frame is obtained from a

rotation of the x-y plane around the z direction by $+5°$ and $5°$. Therefore, it is possible to add the information of the track motion in the y-z plane looking at the u/v-layer hits which are compatible with the x-z plane track projection. The x-z projection candidates are used as "seed". For each x-z projection, the predicted $x_{\text{pred},u/v}$ position at the z position of u/v-layers is evaluated:

$$x_{\text{pred},u/v} = a_x + b_x \cdot z_{u/v} + c_x \cdot z_{u/v}^2.$$

The distance between the u/v-layers hits and $x_{\text{pred},u/v}$ allows to identify for each u/v-hits a y measurement:

$$y_{u/v} = \frac{x_{\text{measured},u/v} - x_{\text{pred},u/v}}{\tan \alpha_{u/v}}.$$

Therefore, only u/v hits compatible with the $x - z$ projection of the candidate track are loaded in the stereo retina associated to the relative axial track. A sketch showing the SciFi detector geometry (of one T-Station) is shown in Fig. 6.1.
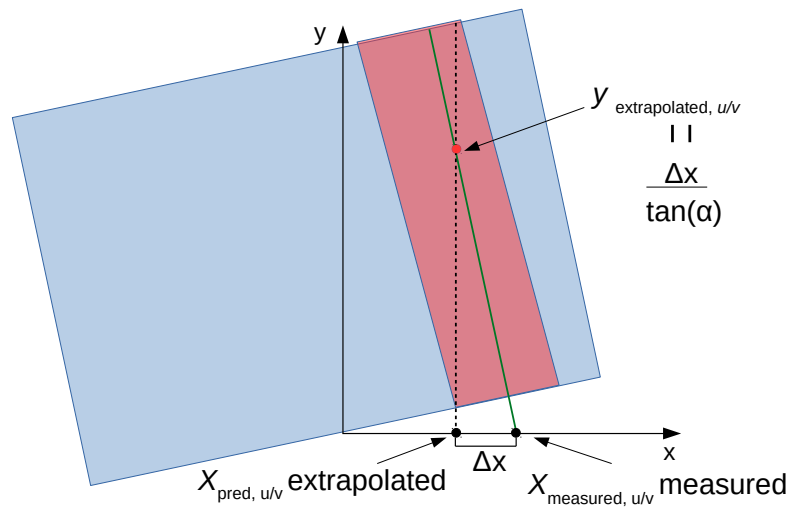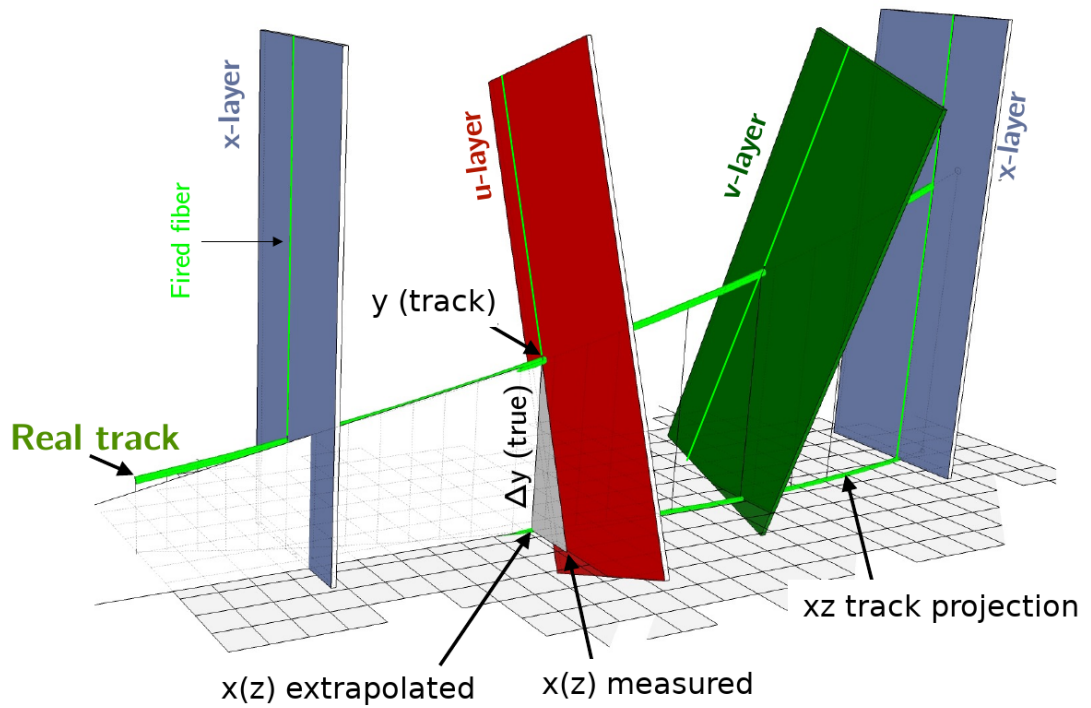
Figure 6.1: Graphical representation of the extraction of the $y_{u/v}$-coordinate track intersection, given the $x_{\mathrm{measured},u/v}$ coordinate of the u/v-hit of a stereo SciFi layer and the predicted $x_{\mathrm{pred},u/v}$-coordinate of the reconstructed axial track candidate. The $y_{u/v}$-coordinate (red dot) comes from the intersection of the u/v-hit (green line in the bottom figure) with a straight line parallel to the y axis and passing through the $x_{\mathrm{pred},u/v}$-coordinate (vertical black dashed line in the bottom figure). Only u/v-hits compatible with the axial track projection (transparent red band in the bottom figure) are sent to the stereo retina.

6.2.1 Granularity on stereo retina

The topology of local maxima in the stereo retina is sensitive to the accuracy at which the axial track parameters are determined in the axial retina. Fig. 6.2 shows a single track event where axial $x - z$ projection is clearly identified by a very precise local maximum (retina on the left). The stereo retina (retina on the right) is filled with $y_{u/v}$-coordinates where the values of $x_{\mathrm{pred},u/v}$, as a function of z-coordinate, is a straight line, and the reconstructed axial track parameters are determined from the center (x_0, x_{11}) of the found local maximum. With these approximations the contributions of the six u/v-hits are splitted and do not meet to form a clear local maximum in the stereo retina. This issue is solved by measuring more precisely

Figure 6.2: Axial (left) and stereo (right) retina of single track event. The stereo retina is filled with $y_{u/v}$-coordinates where the values of $x_{\mathrm{pred},u/v}$, as a function of z-coordinate, is a straight line, and the reconstructed axial track parameters are determined from the center (x_0, x_{11}) of the found local maximum. In this illustrative example, granularity of stereo retina is the same of that one of the axial retina. See text for details.

the axial track parameters using the parabola model through the linearized χ^2 fit procedure described in the previous chapter, as shown in Fig. 6.3. In addition, since the amount of hits filling the individual stereo retinas is a small fraction of the total, the number of pattern cells can be small, in order to allow to absorb in a single cell any residual splitting of the $y_{u/v}$-hits of the track. As mentioned in the previous chapter, the parameter extraction procedure does not require a large amount of logic, but only the usage of the DSP blocks present in the modern FPGAs.

6.3 Stereo fit

Even if not all the u/v-hits are loaded into the stereo retina, for each reconstructed axial candidates, the search of local maxima produces a number of maxima over
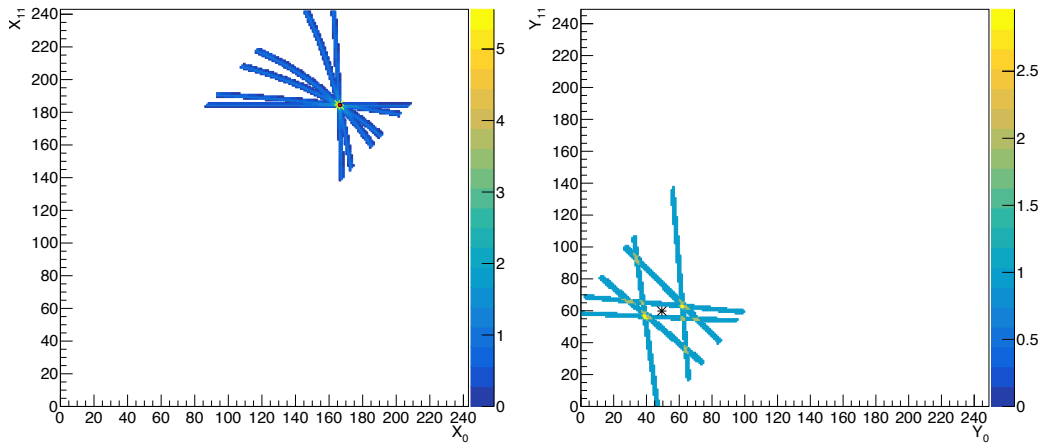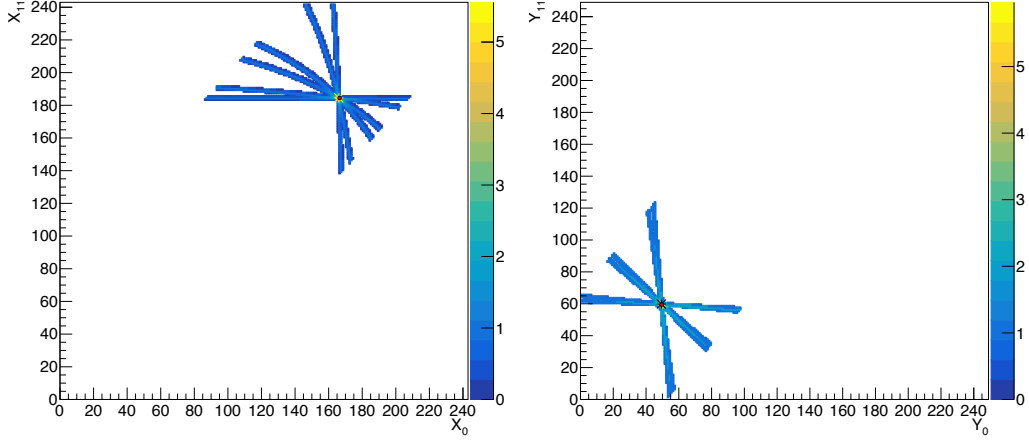
Figure 6.3: Axial (left) and stereo (right) retina of single track event. The stereo retina is filled with $y_{u/v}$-coordinates where the values of $x_{\mathrm{pred},u/v}$, as a function of z-coordinate, is a parabola, and the reconstructed axial track parameters are determined from the linearized χ^2 calculation for the local maximum. In this illustrative example, granularity of stereo retina is the same of that one of the axial retina. See text for details.

threshold which is larger than one. The chosen granularity of the stereo retinas, covering the same quadrant studied in the axial case, is equal to 30×30 pattern cells, where the number of cells mapping the effective diagonal band is equal to 355, which is much lower than 25800[1], i.e. the number of pattern cells used to map the diagonal band of axial retina. Reconstructed track candidates in the stereo view, associated to a given axial track candidate, are found with the same procedure developed for the axial retina (see chapter 5). A number of u/v-hits, in a different stereo SciFi layers has to be larger than 4 ($n_{\mathrm{hit}}^{\mathrm{S}} \geq 4$) and the excitation level of the stereo retinas has to be larger than 3 ($W_{\mathrm{T}}^{\mathrm{S}} \geq 3$). Then, the linearized χ^2 value is calculated using only u/v-hits stored in the pattern cell, as for the axial case, and the local maximum having the minimum χ_{S}^2 value is chosen as the stereo counterpart of the relative axial track. Other stereo local maxima are discarded. No absolute requirement on the χ_{S}^2 value is required, since it is used only to make association between the two view.

Fig. 6.4 shows two examples of the excitation level of two stereo retinas filled with SciFi subdetector u/v-hits from fully simulated LHCb Upgrade events. They are associated to two different axial tracks.

6.3.1 Results

Tab. 6.1 report the final measured axial (ε_{A}) and the three-dimensional ($\varepsilon_{\mathrm{AS}}$) tracking efficiencies using 100 events of the three available fully simulated samples at the

---

[1]Granularity of axial retina is 250×250 pattern cells for each quadrant, but only 25800 pattern cells are used to map the diagonal band of the phase space track parameters.
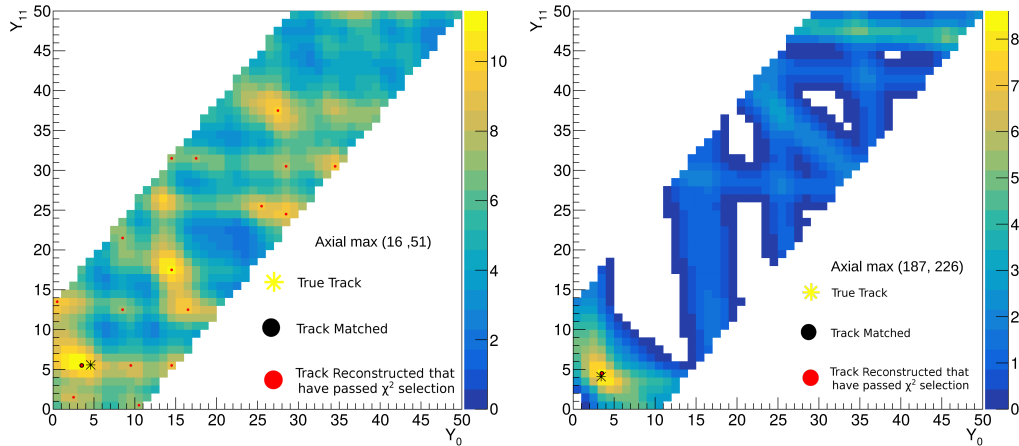
Figure 6.4: Excitation level of two stereo retinas filled with SciFi subdetector hits from fully simulated LHCb Upgrade events. True tracks (yellow stars), reconstructed track candidates (red dots), and truth-matched reconstructed track candidates (black dots) are superimposed.

conditions of the LHCb Upgrade-I (LHC Run 3 and Run 4).

Efficiencies equal or above the 80% level are measured for long and down tracks categories, for all the three simulated samples. If some minimal requirements on track momentum is applied[2] efficiencies values around 80%-87% are obtained. The measured tracking efficiencies of the *Sample 2* are particularly relevant for the Downstream Tracker. The *Sample 2* contains in each event a long lived K_S^0 particle from the $D^{*+} \rightarrow D^0 \pi^+ \rightarrow [K_S^0 \pi^+ \pi^-] \pi^+$ decay chain. It is worth noting that generic downstream tracks (with $p > 5\,\text{GeV}$) are reconstructed with a full three-dimensional reconstruction efficiency of about 83.6%, while down strange tracks[3] (with $p > 3\,\text{GeV}$) are reconstructed with a full three-dimensional reconstruction efficiency of about 86.7%. Axial reconstruction efficiencies for the same tracks are about 90%. These are very important results in view of the realization and installation of the Downstream Tracker device during the LHC LS3.

Since no quality requirement is applied to the stereo χ_S^2, the amount of fake tracks, namely the ghost rate, can only increase when the association with a stereo reconstructed track is required, because of a wrong association. A full three-dimensional reconstructed track is required to satisfy 3D truth-matched criteria only if both axial and stereo parameters are compatible within a 3×3 square, both in the axial and stereo retina. This issue has to be optimized in the future, because the probability of misassociating the stereo track counterpart has to be almost null, once the

---

[2]$p > 1, 3, 5$ GeV are very minimal requirements that almost the majority of LHCb analyses uses for physics signal tracks. They are also very close to intrinsic limit of the LHCb Upgrade tracking system, including Velo and Upstream Tracker.

[3] *strange* downstream tracks are mainly pions from $K_S^0 \rightarrow \pi^+ \pi^-$ decay.

most difficult task of the pattern recognition (the axial one) is successfully carried out. Anyway the loss of efficiency, moving from a pure axial reconstruction to a full three-dimensional reconstruction, is already small, below the 10% level. The final ghost rate is under control, about 20%, and it is comparable with the ghost rate obtained with the LHCb offline reconstruction software program. Anyway, as mentioned above, the effective rate of reconstructing fake tracks is the axial one, because the increase of the ghost rate is only due to the misassociation of the stereo track counterparts.

Tab. 6.2 and tab. 6.3 report the measured tracking efficiencies in two different tracking configurations in order to assess the quality of the performance when a full linearized three-dimensional fit, using both axial and stereo hits is performed once the stereo local maximum is found (tab. 6.2), and when the axial χ^2 threshold is moved from 20 to 40 (tab. 6.3). No large differences in performance are found, so the central configuration of tab. 6.1 is satisfactory.

Track type	Sample 1		Sample 2		Sample 3	
	ε_A	ε_{AS}	ε_A	ε_{AS}	ε_A	ε_{AS}
hasT	75.0	71.4	74.4	70.0	73.9	67.4
hasT, $p > 1\text{GeV}/c$	77.6	73.9	77.7	73.1	76.4	69.7
hasT, $p > 3\text{GeV}/c$	87.0	83.0	85.9	80.8	85.1	77.2
hasT, $p > 5\text{GeV}/c$	90.3	85.7	88.2	82.7	86.6	77.4
Long	81.7	78.8	84.1	79.5	84.2	77.2
Long, $p > 1\text{GeV}/c$	81.7	78.8	84.1	79.5	84.2	77.2
Long, $p > 3\text{GeV}/c$	87.3	84.2	87.1	82.3	87.3	79.8
Long, $p > 5\text{GeV}/c$	90.6	86.9	88.1	83.1	88.1	79.9
Down	80.1	77.7	83.0	78.6	82.6	76.2
Down, $p > 1\text{GeV}/c$	80.1	77.7	83.0	78.6	82.6	76.2
Down, $p > 3\text{GeV}/c$	87.0	84.4	87.1	82.5	86.5	79.3
Down, $p > 5\text{GeV}/c$	90.5	87.5	88.8	83.6	87.9	80.2
Down strange	-	-	84.7	82.8	-	-
Down strange, $p > 1\text{GeV}/c$	-	-	84.7	82.8	-	-
Down strange, $p > 3\text{GeV}/c$	-	-	89.4	86.7	-	-
Down strange, $p > 5\text{GeV}/c$	-	-	93.0	87.2	-	-
ghost rate	12.1	15.7	16.3	20.2	18.4	24.7

Table 6.1: Axial only (ε_A) and three-dimensional (ε_{AS}) reconstruction efficiencies for different simulated samples and different track categories. Results are obtained with the axial retina mapped along the diagonal (25800 engines per quadrant) and stereo retinas mapped along the diagonal (355 engines). Reconstructed axial track candidates are local maxima over threshold with $W_T^A > 4$, have at least 4 axial hits coming from 4 different SciFi layers, and passes the $\chi_A^2 < 20$ requirement. For the three-dimensional reconstruction tracks also are a local stereo maxima over threshold with $W_T^S = 3$, have at least 4 stereo hits coming from 4 different SciFi titled layers. The stereo fit is performed on the 5 (out of 6) hit combinations from the u/v-layers only. Results for down strange tracks, that are mainly pions from $K_S^0 \to \pi^+\pi^-$ decay, are reported only for the *Sample 2*.

Track type	Sample 1 ε_A	Sample 1 ε_{AS}	Sample 2 ε_A	Sample 2 ε_{AS}	Sample 3 ε_A	Sample 3 ε_{AS}
hasT	75.0	71.5	74.4	70.1	73.9	68.3
hasT, $p > 1\mathrm{GeV/c}$	77.6	74.0	77.7	73.2	76.4	70.6
hasT, $p > 3\mathrm{GeV/c}$	87.0	83.1	85.9	80.8	85.1	78.3
hasT, $p > 5\mathrm{GeV/c}$	90.3	85.7	88.2	82.8	86.6	78.9
Long	81.7	79.1	84.1	79.5	84.2	78.3
Long, $p > 1\mathrm{GeV/c}$	81.7	79.1	84.1	79.5	84.2	78.3
Long, $p > 3\mathrm{GeV/c}$	87.3	84.4	87.1	82.5	87.3	80.9
Long, $p > 5\mathrm{GeV/c}$	90.6	87.1	88.1	83.2	88.1	81.2
Down	80.1	77.9	83.0	78.7	82.6	77.2
Down, $p > 1\mathrm{GeV/c}$	80.1	77.9	83.0	78.7	82.6	77.2
Down, $p > 3\mathrm{GeV/c}$	87.0	84.6	87.1	82.6	86.5	80.4
Down, $p > 5\mathrm{GeV/c}$	90.5	87.7	88.8	83.8	87.9	81.3
Down strange	-	-	84.7	82.8	-	-
Down strange, $p > 1\mathrm{GeV/c}$	-	-	84.7	82.8	-	-
Down strange, $p > 3\mathrm{GeV/c}$	-	-	89.4	86.7	-	-
Down strange, $p > 5\mathrm{GeV/c}$	-	-	93.0	87.2	-	-
ghost rate	12.1	15.6	16.3	20.1	18.4	23.6

Table 6.2: Axial only (ε_A) and three-dimensional (ε_{AS}) reconstruction efficiencies for different simulated samples and different track categories. Results are obtained with the axial retina mapped along the diagonal (25800 engines per quadrant) and stereo retinas mapped along the diagonal (355 engines). Reconstructed axial track candidates are local maxima over threshold with $W_T^A > 4$, have at least 4 axial hits coming from 4 different SciFi layers, and passes the $\chi_A^2 < 20$ requirement. For the three-dimensional reconstruction tracks also are a local stereo maxima over threshold with $W_T^S = 3$, have at least 4 stereo hits coming from 4 different SciFi titled layers. A global three-dimensional fit is performed on 5 pre-determined axial hits plus 5 hits (out of 6) combinations of the u/v-layers. Results for down strange tracks, that are mainly pions from $K_S^0 \rightarrow \pi^+\pi^-$ decay, are reported only for the *Sample 2*.

Track type	Sample 1		Sample 2		Sample 3	
	ε_A	ε_{AS}	ε_A	ε_{AS}	ε_A	ε_{AS}
hasT	78.4	74.6	78.8	74.1	78.0	72.2
hasT, $p > 1\mathrm{GeV/c}$	81.1	77.3	82.2	77.3	80.6	74.7
hasT, $p > 3\mathrm{GeV/c}$	88.7	84.4	88.0	82.5	86.8	80.1
hasT, $p > 5\mathrm{GeV/c}$	91.2	86.6	89.8	83.8	87.8	80.1
Long	84.9	81.6	86.8	81.9	87.1	81.1
Long, $p > 1\mathrm{GeV/c}$	84.9	81.6	86.8	81.9	87.1	81.1
Long, $p > 3\mathrm{GeV/c}$	88.9	85.3	88.7	83.6	89.1	82.8
Long, $p > 5\mathrm{GeV/c}$	91.6	87.7	89.2	83.9	89.2	82.3
Down	83.6	80.7	86.4	81.8	86.1	80.6
Down, $p > 1\mathrm{GeV/c}$	83.6	80.7	86.4	81.8	86.1	80.6
Down, $p > 3\mathrm{GeV/c}$	88.6	85.4	88.7	83.9	88.4	82.4
Down, $p > 5\mathrm{GeV/c}$	91.4	88.0	89.9	84.6	89.0	82.4
Down strange	-	-	85.9	83.3	-	-
Down strange, $p > 1\mathrm{GeV/c}$	-	-	85.9	83.3	-	-
Down strange, $p > 3\mathrm{GeV/c}$	-	-	90.2	86.7	-	-
Down strange, $p > 5\mathrm{GeV/c}$	-	-	93.0	87.2	-	-
ghost rate	15.4	18.3	21.4	24.9	24.18	28.6

Table 6.3: Axial only (ε_A) and three-dimensional (ε_AS) reconstruction efficiencies for different simulated samples and different track categories. Results are obtained with the axial retina mapped along the diagonal (25800 engines per quadrant) and stereo retinas mapped along the diagonal (355 engines). Reconstructed axial track candidates are local maxima over threshold with $W_\mathrm{T}^\mathrm{A} > 4$, have at least 4 axial hits coming from 4 different SciFi layers, and passes the $\chi_\mathrm{A}^2 < 40$ requirement. For the three-dimensional reconstruction tracks also are a local stereo maxima over threshold with $W_\mathrm{T}^\mathrm{S} = 3$, have at least 4 stereo hits coming from 4 different SciFi titled layers. The stereo fit is performed on the 5 (out of 6) hit combinations from the u/v-layers only. Results for down strange tracks, that are mainly pions from $K_\mathrm{S}^0 \to \pi^+\pi^-$ decay, are reported only for the *Sample 2*.
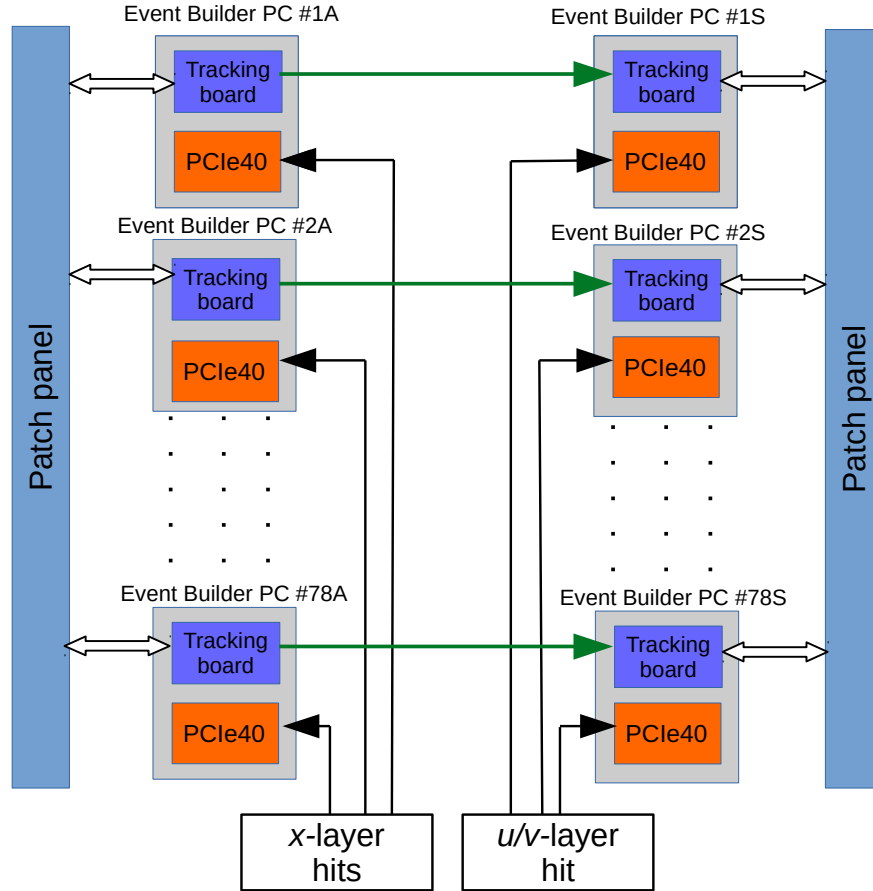
Figure 6.5: Schematic view of the architecture of the envisioned Downstream Tracker.

6.4 Envisioned hardware implementation

The envisioned architecture of the Downstream Tracker is described in Sec. 3.3. The full track reconstruction for the SciFi tracker can be implemented similarly, as shown in Fig. 6.5. The expected number of EB nodes dedicated to the SciFi tracker are expected to be 156. One half of these nodes (78 EB PC nodes) receives the raw hits from the x-layers of the detector, while the other half receives the raw hits from the u/v-layers. The idea is to instrument entirely all the 156 Event Builder nodes with the same number of tracking boards with two different Patch Panels and Switching Networks. The system will first find for axial tracks in 78 axial sub-retinas with approximately a latency less than 500 ns. When axial tracks will be ready, they will be sent to the relative stereo tracking boards, that will contain only u/v-hits compatible with axial tracks reconstructed in the associated axial tracking boards. The stereo tracking boards should host approximately three (or more than three, it depends on the capacity of the FPGAs chip) identical and independent stereo retinas for a total of (355×3) 1065 engines, in order to simultaneously process three axial

tracks at the time, in order to associate the stereo track counterparts. The average number of reconstructed axial track in a single tracking board is indeed 3. If a larger number of axial tracks will arrive on a stereo tracking board they must be serially processed increasing the latency of the system, expected to be approximately of the same order of that necessary for the axial reconstruction.

The size of the final system, in order to reconstruct three-dimensional T-tracks using information from the Scintillating Fibre Tracker detector, requires approximately 10^5 pattern cells (engines) for solving the pattern recognition using the axial layers, and approximately further 10^5 pattern cells (engines) for associating the stereo track counterparts. This size seems to be affordable with already available current FPGA chips, for a system to be installed during the LHC LS3 (2025-2026).

Chapter 7

Comparison with the official LHCb offline tracking software program and conclusions

This chapter reports the final Downstream Tracker performance along with a detailed comparison with the official LHCb offline tracking software reconstruction program, the so-called Hybrid Seeding. Final conclusions of the thesis are also reported.

7.1 Brief resume of the LHCb offline reconstruction software

The Hybrid Seeding [71] is a standalone track search in the T-stations. The algorithm is designed to reach a good compromise between tracking efficiencies, ghost rate and timing. The main idea behind the Hybrid Seeding is to progressively clean the tracking environment: first finding the tracks which are easier to reconstruct, and then looking for the harder ones using the left-over hits. The design of the algorithm is shown in Fig. 7.1. An overview of its implementation is illustrated here.

1. **Cases.** The algorithm is divided in different steps, called Cases, where tracks covering different momentum ranges are searched for. The algorithm supports and execute a total of three Cases by default and it can be configured to execute only one or two of them through the configurable option named `NCases`. The momentum ranges covered depending on the Case are shown in Tab.7.1. Each Case depend on the execution of the previous one, since it considers the left-over hits from the previous track search iteration. This behavior can be changed by the `FlagHits` and `RemoveFlagged` options, which are taking care of flagging the hits at the end of each Case and to not allow to re-use the flagged hits .

2. **Upper/lower division.** For each Case, the tracks are searched first in the $y > 0$ part of the detector and then in the $y < 0$ part. It is possible to use this

Case 1	Case 2	Case 3
$P > 5\text{GeV/c}$	$P > 2\text{GeV/c}$	$P > 1.5\text{GeV/c}$

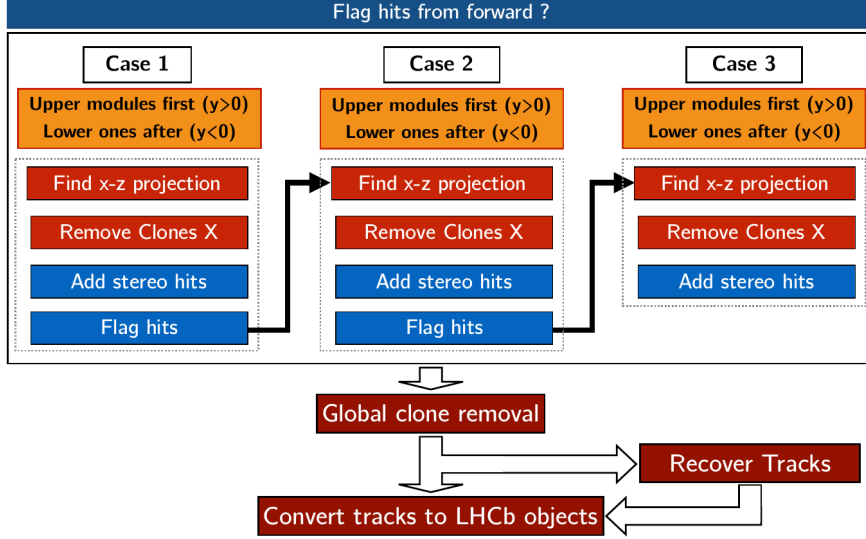Table 7.1: Momentum ranges covered by the algorithm depending on the Case.

Figure 7.1: Offline algorithm scheme

approach because the fraction of tracks migrating from the upper to the lower part of the detector is negligible.

3. **Find $x - z$ projections.** For each Case, all the $x - z$ track projections are searched for using solely the hits from x-layers. The track search in each Case is designed in a projective approach, i.e. the tracks are looked for starting from a two-hit combination from two different x-layers which are the farthest possible (one hit in T1 and a second one in T3). A third hit is searched in T2 for each two-hit combination and from the resulting parabola other hits in the three remaining x-layers are searched for.

4. **Remove clones X.** An intermediate clone removal step is applied to the $x - z$ track projections. This is achieved by counting the number of hits shared between the projections found in the same Case and selecting the best one based on the value of the track χ^2 and the number of fired x-layers.

5. **Add stereo hits.** All stereo hits compatible with a $x - z$ projection surviving the intermediate clone killing step are collected. A Hough-like transformation on the stereo hits is used to identify potential line candidates as $y - z$ projections associated to the $x - z$ projection of the track. Additional preliminary criteria

116

are applied to select the potential line candidates for a given $x - z$ projection. For each line candidate, the full track ($x - z$ projection plus line candidate) undergoes the simultaneous fit procedure, eventually removing outlier hits. The final χ^2 is checked to be within the tolerances and a track candidate is generated. The best track candidate among those sharing the same $x - z$ projection is selected on the basis of its χ^2 and the number of hits involving different layers.

6. **Flag hits.** The hits used by the track candidates found by the first two Cases are flagged (if `FlagHits` option is enabled) and they become unavailable for the track search in the following Case (if `RemoveFlagged` option is enabled).

7. **Global clone removal.** Once all the Cases have been processed, a global clone removal step is applied based on the fraction of shared hits between the tracks and their χ^2/ndof .

8. **Track recovering routine.** All the $x - z$ projections from all the Cases which are not promoted to full tracks when looking at matching u/v-hits are recovered requiring for them to be composed of hits which are not used by any of the already found full track candidates. For the recovered $x - z$ projections stereo layer hits are added using a set of dedicated parameters.

9. **Convert tracks to LHCb objects.** All the track candidates found by the algorithm are converted into standard LHCb objects, which can be used by other algorithms and handled by the Kalman filter.

Step 0	exit of Case 1 x-z projection search (after performing the removal of clones)
Step 1	exit of Case 1 stereo hit search for the x-z projections found in Case 1
Step 2	exit of Case 2 x-z projection search (after performing the removal of clones)
Step 3	exit of Case 2 stereo hit search for the x-z projections found in Case 2
Step 4	exit of Case 3 x-z projection search (after performing the removal of clones)
Step 5	exit of Case 3 stereo hit search for the x-z projections found in Case 3
Step 6	track recovery routine in which the recovered x-z projections are selected (just before adding the stereo hits with dedicated parameters)
Step 7	at the exit of the Hybrid Seeding, where all track candidates have been found

Table 7.2: Different steps defined in the algorithm used to break-up the performance evolution of the Hybrid Seeding.

7.2 Downstream Tracker and Hybrid Seeding

Tracking performances of the Downstream Tracker, measured on the three different simulated samples, are presented in detail in Chapter 6. The axial tracking efficiencies ε_A in reconstructing tracks of physics interest, as the long tracks or the downstream
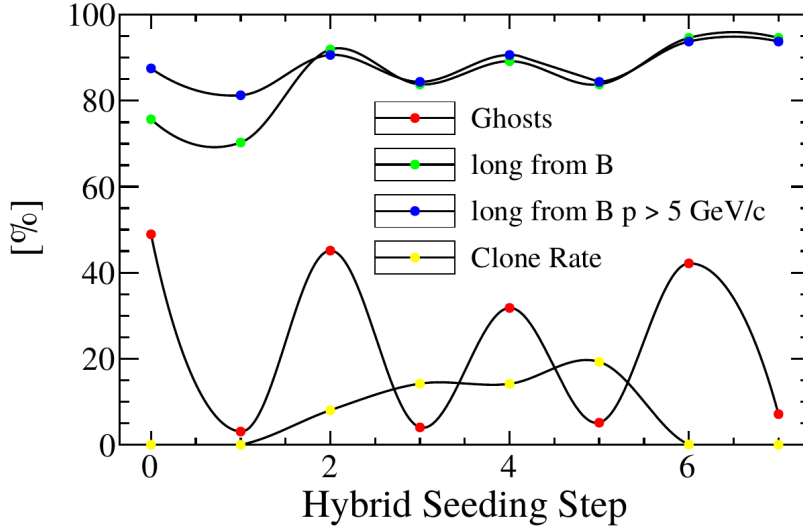
Figure 7.2: Evolution of tracking efficiency, ghost rate (red) and clone tracks rate (for hasT track categories in yellow) for the Hybrid Seeding algorithm. Tracking efficiency is shown for all Long track from b-hadrons in the event (green) and selecting only those having $p > 5\text{GeV/c}$ (blue). The various Hybrid Seeding step are defined in Tab. 7.2.

(down in the tables), are approximately equal to 90% with an event-averaged ghost rate of about 20%, i.e. one false positive track each four correctly reconstructed tracks. The three-dimensional reconstruction efficiencies ε_{AS} in reconstructing tracks of physics interest (as above), are about $80 - 85\%$.

The comparison with the offline reconstruction algorithm, i.e. the Hybrid Seeding, is shown in tab.7.3 and tab. 7.4 for *Sample 2* and *Sample 3*, the only available ones in Ref. [71]. Performances are quite similar, and ghost rate is comparable[1]. This is very satisfactory. High quality T-tracks seeds from Downstream Tracker can be sent to the Event Filter Farm for triggering even in the harsh conditions of rate and luminosity that LHCb will face in the Future Upgrades Runs with a full readout of the detector at 30MHz.

---

[1]Actually, for the *Sample 3*, the Hybrid Seeding provides a ghost rate much smaller than that obtained in the *Sample 2* and this is unexplained.

Track type	Hybrid Seeding	Downstream Tracker	
	ϵ	ϵ_A	ϵ_{AS}
hasT	66.6%	74.4%	70.0%
Long	92.1%	84.1%	79.5%
Long, $P > 5\,\text{GeV}/c$	95.4%	88.1%	83.1%
Down strange	91.8%	84.7%	82.8%
Down strange $P > 5\,\text{GeV}/c$	95.7%	93.0%	87.2%
Down strange, noVELO	91.3%	79.1%	74.0%
Down strange, noVELO, $P > 5\,\text{GeV}/c$	95.6%	90.0%	84.0%
ghost rate (evt.avg)	19.4%	16.3 %	20.2%

Table 7.3: Tracking performances comparison between the Downstream Tracker and the Hybrid Seeding algorithms for $D^{*+} \to D^{*+} \to D^0\pi^+ \to [K_\mathrm{S}^0\pi^+\pi^-]\pi^+$.

Track type	Hybrid Seeding	Downstream Tracker	
	ϵ	ϵ_A	ϵ_{AS}
hasT	67.2%	73.9%	67.4%
Long	90.6%	84.2%	77.2%
Long, $p > 5\,\text{GeV}/c$	94.8%	88.1%	79.9%
Long from B	93.4%	91.8%	88.6%
Long from B, $p > 5\,\text{GeV}/c$	95.4%	91.7%	88.8%
Down strange, noVELO	89.7%	82.0%	74.5%
Down strange, noVELO, $p > 5\,\text{GeV}/c$	95.2%	89.8%	84.7%
ghost rate (evt.avg)	4.5 %	18.4%	24.7%

Table 7.4: Tracking performances comparison between the the Downstream Tracker and the Hybrid Seeding algorithms for $B_s^0 \to \phi\phi \to [K^+K^-][K^+K^-]$.

7.3 Final conclusions

In this thesis, the first study of the performance of real-time reconstruction of tracks in the SciFi detector achievable with the artificial retina algorithm, using fully simulated events at the LHCb Upgrade (LHC Run 4) conditions, is presented. This is a crucial milestone on the path of the realization of the Downstream Tracker processor for the Future Upgrades of the LHCb experiment, that would allow to recover the reconstruction efficiency of the decay channels containing downstream tracks. This thesis has shown that tracking performance obtainable with this approach, in a cost effective way, is comparable with the offline software reconstruction performance.

The thesis presents the first results on the reconstruction of the three-dimensional T-tracks of a generic LHCb-Upgrade event. I demonstrated that a full three-dimensional reconstruction is achievable using a number of about 10^5 pattern cells to fully solve the pattern recognition and finding tracks in the axial $x - z$ view (6 axial SciFi detector layers), and about 10^5 pattern cells to associate the stereo track counterparts in the $y - z$ view (6 u/v SciFi detector layers), where each pattern cell (or engine) requires to be implemented on modern FPGAs about 1300 LEs. Both measured reconstruction efficiency and ghost rate are comparable to those obtained with the official offline tracking program; a generic T-track is reconstructed with an efficiency of about 70% with a ghost rate of about 20%. Requiring a minimal momentum threshold, as three-dimensional momentum larger than 5 GeV, and that the track has to be a downstream track or it has to come from the interaction point, axial efficiencies in the range of 90% and three-dimensional efficiencies of 84% are achieved.

I also designed for the first time a possible realistic architecture for the Downstream Tracker, and how it should be integrated into the future LHCb-Upgrade data acquisition system. Its size, from these preliminary studies, seems to be affordable and cost effective, and it may be implemented with the already available FPGA chips. The Downstream Tracker is planned to be installed during the LHC LS3 (2025-2026), to operate during the LHCb Upgrade-Ib (Run4, 2027-2029). At that time its cost will be a small fraction of the cost of the data acquisition system and of the Event Filter Farm.

Bibliography

[1] LHCb collaboration, *Expression of Interest for a Phase-II LHCb Upgrade: Opportunities in flavour physics, and beyond, in the HL-LHC era*, CERN-LHCC-2017-003.

[2] L. E. The LHCb Collaboration, *Physics case for an LHCb Upgrade II*, Tech. Rep. LHCb-PUB-2018-009. CERN-LHCb-PUB-2018-009, CERN, Geneva, May, 2018.

[3] L. Ristori, *An artificial retina for fast track finding*, Nucl. Instrum. Meth. **A453** (2000) 425.

[4] S. Stracka et al. *An artificial retina processor for track reconstruction at the lhc crossing rate*, Journal of Physics: Conference Series **898** (2017), no. 3 032038.

[5] F. Lazzari, *Development of a real-time tracking device for the LHCb Upgrade 1b*, Master's thesis, University of Pisa, etd-11202017-113320, 2017.

[6] R. Cenci et al. *Development of a High-Throughput Tracking Processor on FPGA Boards*, PoS **TWEPP-17** (2017) 136.

[7] LHCb collaboration, *LHCb Tracker Upgrade Technical Design Report*, CERN-LHCC-2014-001. LHCb-TDR-015.

[8] J. H. Christenson, J. W. Cronin *et al.*, *Evidence for the 2π decay of the K_2^0 meson*, Phys. Rev. Lett. **13** (1964), no. 4 138.

[9] A. D. Sakharov, *Violation of CP invariance, C asymmetry, and baryon asymmetry of the Universe*, Pisma Zh. Exp. Theor. Fiz. **5** (1967) 32, English translation in JETP Lett. 5, 24 (1967), reprinted in Sov. Phys. Usp. 34, 392 (1991).

[10] NA48 collaboration, *A new measurement of direct CP violation in two pion decays of the neutral kaon*, Phys. Rev. Lett. **B465** (1999), no. 335.

[11] KTeV collaboration, *Observation of direct CP violation in $K_{S,L} \to \pi\pi$ decays*, Phys. Rev. Lett. **83** (1999), no. 22.

[12] L. Wolfenstein, *Violation of CP invariance and the possibility of very weak interaction*, Phys. Rev. Lett. **13** (1964), no. 18 562.

[13] BABAR collaboration, *Observation of CP violation in the B^0 meson system*, Phys. Rev. Lett. **87** (2001), no. 9:091801.

[14] BELLE collaboration, *Observation of large CP violation in the neutral B meson system*, Phys. Rev. Lett. **87** (2001), no. 9:091802.

[15] N. Cabibbo, *Unitary symmetry and leptonic decays*, Phys. Rev. Lett. **10** (1963), no. 12 531.

[16] M. Kobayashi and T. Maskawa, *CP-Violation in the Renormalizable Theory of Weak Interaction*, Prog. Theor. Phys. **49** (1973), no. 2 652.

[17] C. Jarlskog, *Commutator of the Quark Mass Matrices in the Standard Electroweak Model and a Measure of Maximal CP Nonconservation*, Phys. Rev. Lett. **55** (1985), no. 10 1039.

[18] C. Jarlskog, *A basis independent formulation of the connection between quark mass matrices, CP violation and experiment*, Z. Phys. C **29** (1985) 491.

[19] I. Dunietz, O. W. Greenberg, and D.-D. Wu, *A priori definition of maximal CP nonconservation*, Phys. Rev. Lett. **55** (1985), no. 27 2935.

[20] CKMfitter Group, J. Charles *et al.*, *CP violation and the CKM matrix: assessing the impact of the asymmetric B factories. Updated results and plots available at: http://ckmfitter.in2p3.fr*, The European Physical Journal C - Particles and Fields **41** (2005) 1.

[21] L. Wolfenstein, *Parameterization of the Kobayashi-Maskawa Matrix*, Phys. Rev. Lett. **51** (1983), no. 21 1945.

[22] M. Battaglia, A. J. Buras *et al.*, *The CKM Matrix and the Unitarity Triangle*, arXiv **0304132** (2003).

[23] J. E. Augustin, A. M. Boyarski *et al.*, *Discovery of a Narrow Resonance in e^+e^- Annihilation*, Phys. Rev. Lett. **33** (1974), no. 23 1406.

[24] J. J. Aubert, U. Becker *et al.*, *Experimental Observation of a Heavy Particle J*, Phys. Rev. Lett. **33** (1974), no. 23 1404.

[25] S. W. Herb *et al.*, *Observation of a dimuon resonance at 9.5 GeV in 400-GeV proton-nucleus collisions*, Physical Review Letter **39** (1977), no. 5 252.

[26] N. Ellis and A. Kernan, *Heavy quark production at the CERN $p\bar{p}$ collider*, Phys. Rept. **195** (1990) 23.

[27] CDF collaboration, *Measurement of the $B^0\bar{B}^0$ flavor oscillations frequency and study of same side flavor tagging of B mesons in $p\bar{p}$ collisions*, Physical Review D **59:032001** (1999).

[28] CDF collaboration, *Measurement of sin2β from $B \to J/\psi K_S^0$ with the CDF detector*, Physical Review D **61:072005** (2000).

[29] Particle Data Group, C. Patrignani *et al.*, *Review of particle physics*, Chin. Phys. **C40** (2016) 100001, and 2017 update.

[30] BaBar collaboration, D. Boutigny *et al.*, *BaBar technical design report*, in *BaBar Technical Design Report EPAC Meeting Stanford, California, March 17-18, 1995*, 1995.

[31] A. Abashian *et al.*, *The Belle Detector*, Nucl. Instrum. Meth. **A479** (2002) 117.

[32] C.-h. Cheng, *Measurements of the CKM Angle beta/phi(1) at B factories*, eConf **C070512** (2007) 010, `arXiv:0707.1192`.

[33] Belle-II collaboration, T. Abe *et al.*, *Belle II Technical Design Report*, `arXiv:1011.0352`.

[34] A. Achilli *et al.*, *Total and inelastic cross sections at LHC at $\sqrt{s} = 7$ TeV and beyond*, Phys. Rev. D **84** (2011) 094009.

[35] LHCb collaboration, Yu. Guz, *Studies of open charm and charmonium production at LHCb*, Nucl. Phys. Proc. Suppl. **207-208** (2010) 355.

[36] CDF collaboration, *Measurement of the J/ϕ and b-Hadron Production Cross Sections in $p\bar{p}$ Collisions at $\sqrt{s} = 1960$ GeV*, Phys. Rev. D **71** (2005), no. 032001.

[37] LHCb collaboration, *Measurement of $\sigma(pp \to b\bar{b}X)$ at $\sqrt{s} = 7$ TeV in the forward region*, Phys. Lett. B **694** (2010) 209.

[38] LHCb collaboration, *LHCb Trigger and Online Technical Design Report*, CERN-LHCC-2014-016. LHCb-TDR-016.

[39] T. Abe *et al.*, *Belle II Technical Design Report*, ArXiv e-prints (2010) `arXiv:1011.0352`.

[40] E. Kou *et al.*, *The Belle II Physics Book*, `arXiv:1808.10567`.

[41] K. Akai, K. Furukawa, and H. Koiso, *SuperKEKB Collider*, `arXiv:1809.01958arXiv:1809.01958`.

[42] O. S. Brning *et al.*, *LHC Design Report*, CERN Yellow Reports: Monographs, CERN, Geneva, 2004.

[43] LHCb collaboration, A. A. Alves Jr. *et al.*, *The LHCb detector at the LHC*, JINST **3** (2008) S08005.

[44] LHCb collaboration, R. Aaij *et al.*, *LHCb detector performance*, Int. J. Mod. Phys. **A30** (2015) 1530022, `arXiv:1412.6352`.

[45] R. Aaij *et al.*, *Performance of the LHCb Vertex Locator*, JINST **9** (2014) P09007, `arXiv:1405.7808`.

[46] R. Arink *et al.*, *Performance of the LHCb Outer Tracker*, JINST **9** (2014) P01002, `arXiv:1311.3893`.

[47] M. Adinolfi *et al.*, *Performance of the LHCb RICH detector at the LHC*, Eur. Phys. J. **C73** (2013) 2431, `arXiv:1211.6759`.

[48] A. A. Alves Jr. *et al.*, *Performance of the LHCb muon system*, JINST **8** (2013) P02022, `arXiv:1211.1346`.

[49] R. Aaij *et al.*, *The LHCb trigger and its performance in 2011*, JINST **8** (2013) P04022, `arXiv:1211.3055`.

[50] M. Tobin, *Performance of the LHCb Tracking Detectors*, Tech. Rep. CERN-LHCb-PROC-2013-015, 2013.

[51] LHCb collaboration, *Framework TDR for the LHCb Upgrade: Technical Design Report*, CERN-LHCC-2012-007. LHCb-TDR-012.

[52] LHCb collaboration, *LHCb VELO Upgrade Technical Design Report*, CERN-LHCC-2013-021. LHCb-TDR-013.

[53] *Letter of Intent for the LHCb Upgrade*, Tech. Rep. CERN-LHCC-2011-001. LHCC-I-018, CERN, Geneva, Mar, 2011.

[54] A. K. Kuonen *et al.*, *LHCb Scintillating Fibre Tracker Engineering Design Review: Silicon Photomultipliers*, Tech. Rep. LHCb-INT-2016-019. CERN-LHCb-INT-2016-019, CERN, Geneva, Apr, 2016.

[55] Y. Amhis *et al.*, *The Seeding tracking algorithm for a scintillating detector at LHCb*, Tech. Rep. LHCb-PUB-2014-002. CERN-LHCb-PUB-2014-002, CERN, Geneva, Mar, 2014.

[56] M. Vesterinen, A. Davis, and G. Krocker, *Downstream tracking for the LHCb upgrade*, Tech. Rep. LHCb-PUB-2014-007. CERN-LHCb-PUB-2014-007, CERN, Geneva, Jan, 2014.

[57] LHCb collaboration, *Study of $B^0_{(s)} \to K^0_S h^+ h'^-$ decays with first observation of $B^0_s \to K^0_S K^\pm \pi^\mp$ and $B^0_s \to K^0_S \pi^+ \pi^-$*, JHEP **10** (2013) 143. 18 p, Comments: 18 pages, 4 figures, submitted to JHEP.

[58] A. Abba *et al.*, *A specialized track processor for the LHCb upgrade*, Tech. Rep. LHCb-PUB-2014-026. CERN-LHCb-PUB-2014-026, CERN, Geneva, Mar, 2014.

[59] P. Hough, *Machine analysis of Bubble Chamber Pictures*, Proc. Int. Conf. High Energy Accelerators and Instrumentation **C590914** (1959).

[60] P. Hough, *Method and mean for recognizing complex patterns*, US Patent **3069654** (1962).

[61] R. Cenci *et al.*, *Performance of a high-throughput tracking processor implemented on stratix-v fpga*, Nuclear Instruments and Methods in Physics Research Section A: Accelerators, Spectrometers, Detectors and Associated Equipment (2018) .

[62] M. Clemencic *et al.*, *The lhcb simulation application, gauss: Design, evolution and experience*, Journal of Physics: Conference Series **331** (2011), no. 3,"LHCb-PROC-2011-006. CERN-LHCb-PROC-2011-006" 032023.

[63] LHCb collaboration, *LHCb computing: Technical Design Report*, CERN-LHCC-2005-019. LHCb-TDR-011.

[64] S. Agostinelli *et al.*, *Geant4a simulation toolkit*, Nuclear Instruments and Methods in Physics Research Section A: Accelerators, Spectrometers, Detectors and Associated Equipment **506** (2003), no. 3 250.

[65] J. Allison *et al.*, *Geant4 developments and applications*, IEEE Transactions on Nuclear Science **53** (2006) 270.

[66] T. Sjöstrand, S. Mrenna, and P. Skands, *PYTHIA 6.4 physics and manual*, JHEP **05** (2006) 026, `arXiv:hep-ph/0603175`.

[67] D. J. Lange, *The EvtGen particle decay simulation package*, Nucl. Instrum. Meth. **A462** (2001) 152.

[68] E. Cogneras, M. Martinelli, J. van Tilburg, and J. de Vries, *The digitisation of the scintillating fibre detector*, Tech. Rep. LHCb-PUB-2014-003. CERN-LHCb-PUB-2014-003, CERN, Geneva, Apr, 2014.

[69] W. Ashmanskas *et al.*, *The CDF silicon vertex tracker*, Nuclear Instruments and Methods in Physics Research Section A: Accelerators, Spectrometers, Detectors and Associated Equipment **477** (2002), no. 1 451 , 5th Int. Conf. on Position-Sensitive Detectors.

[70] CDF, S. Belforte *et al.*, *SVT TDR (Silicon Vertex Tracker Technical Design Report)*, Tech. Rep. CDF-3108, 1995.

[71] R. Quagliani, Y. S. Amhis, P. Billoir, and F. Polci, *The Hybrid Seeding algorithm for a scintillating fibre tracker at LHCb upgrade: description and performance*, Tech. Rep. LHCb-PUB-2017-018. CERN-LHCb-PUB-2017-018, CERN, Geneva, May, 2017.